"HYPERSONIC BOUNDARY LAYERS IN STRONG PRESSURE GRADIENTS"

S. Mohammadian, Dipl. Ing.

April 1970

A thesis submitted for the Degree of
Doctor of Philosophy in the Faculty of
Engineering of the University of London.

ABSTRACT

The growth of a hypersonic boundary layer over both concave and convex surfaces is described. Several theoretical predictions are examined and compared with the experimental data. The theories used include the exact numerical solution of the laminar boundary layer equations using the programme of Sells, Luxton and Youngs approximate method and Cheng's viscous interaction theory in both its original and modified forms. The strong viscous interaction theory due to Cheng is extended to cover curved surfaces. The resulting equation is normalized and solved asymptotically for small and large arguments. Both the asymptotic solution (for large arguments) and the numerical integration demonstrate the oscillatory behaviour of the equation for the concave surfaces studied here. The solution does not oscillate if other pressure laws are used instead of the Newton-Busemann pressure law employed by Cheng. The solution obtained using

alternative pressure laws are more realistic for both convex and concave surfaces. Other methods are also discussed and compared with experimental data reported here and elsewhere. Experiments in air, conducted in the hypersonic gun tunnel under cold wall conditions at $M = 8.2$ and 12.25, included measurement of surface pressure, surface heat transfer distributions and schlieren studies for concave and convex models.

ACKNOWLEDGEMENTS

The author wishes to express his gratitude for the unfailing guidance and encouragement given by his supervisor, Mr. J.L. Stollery, throughout the course of this study. Thanks are also due to Dr. N.C. Freeman and Dr. J.K. Harvey for their helpful supervision during the temporary absence of Mr. Stollery.

The author would also like to thank the Aeronautics Department Workshop staff for their patient care in the construction of the models, and the library and office staff for their valuable services.

Finally, the author wishes to express his thanks to his wife Erika for her patience and understanding during the course of this study.

CONTENTS

LIST OF ILLUSTRATIONS

Page

Page

Page

Page

Page

Page

NOTATION

Symbols

a,b,c,d	constants
C	constant in viscosity-temperature relation (defined by $\frac{\mu}{\mu_\infty} = C \frac{T}{T_\infty}$)
C_p	specific heat
D,E	constants
F	order one variable
H	shape factor = $\frac{\delta_1}{\delta_2}$
k	thermal conductivity
ℓ	scaling factor in Cheng's equation $= \frac{A^2\bar{\chi}^2}{4\gamma a^4 M^4}$
M	Mach number
n	power in the body shape function
p	pressure
P	pressure ratio, p_e/p_∞
Pr	Prandtl number
$\dot{q}$	heat transfer rate
R	$\int P \, dX$

Re	Reynolds number
St.	Stanton number = $\dfrac{\dot{q}}{\rho_\infty u_\infty (H_\infty - H_w)}$
t	the thickness of the blunt leading edge or nose
T	temperature
x,y	rectangular coordinates in directions parallel and normal, respectively, to the free stream direction, with the origin at the nose
X	$(A\overline{\chi})^{-2}$
Y	scaled y coordinate
u	velocity in x-direction
v	velocity in y-direction
z	certain variable
α	scaled body slope
γ	the specific heat ratio C_p/C_v
δ	boundary layer thickness
δ^* or δ_1	displacement thickness
δ_2	momentum thickness

ε	$(\gamma-1)/(\gamma+1)$
μ	the viscosity of the gas
Λ	pressure gradient form factor
ρ	density
ξ	certain variable
η	order-one variable
Δ^*	scaled displacement thickness $= \dfrac{\delta^*}{a\ell}$
ω	power index of the viscosity-temperature relationship $\mu \sim T^{\omega}$
$\bar{\chi}$	viscous interaction parameter $= M^3 \sqrt{C/Re_x}$
$\bar{\chi}_\varepsilon$	$= .664\ (1+2.6\frac{T_w}{T_o})\bar{\chi}$

Subscripts

e	at the edge of the boundary layer
o	stagnation conditions
w	wall conditions
∞	free stream conditions
f.p.	flat plate

1	initial conditions in barrel
4	initial driver conditions

INTRODUCTION

The development of hypersonic laminar boundary layer theory was stimulated by the progress in aeronautical engineering and in recent times by the development of rockets and artificial satellites. At high Mach numbers the effects of compression and energy dissipation produce considerable increases in temperature. Hypersonic flight is most likely to occur at high altitudes where the density is very low, which accounts for low Reynolds numbers. Under these conditions, high Mach number and low Reynolds number, the boundary layer becomes very thick. The interactions between boundary layer growth and the external inviscid flow can significantly modify the distribution of surface pressure and heat transfer rate. A good example is the leading edge region of a sharp flat plate, where the pressure distribution is significantly changed by the viscous interaction. Rapid changes of boundary layer growth will also occur in regions of strong pressure gradient. It is necessary to predict such mutual interaction before the correct body shape can be designed to give the required performance and to withstand severe pressure and heating loads.

The aim of this work is to enhance such predictions by comparing theory and experiments for hypersonic laminar flow over two-dimensional curved surfaces with sharp leading edges.

The first part of this thesis contains a survey of literature dealing with boundary layers in incompressible, compressible and finally hypersonic flow, both from a theoretical and experimental viewpoint. It also contains a discussion about the assumption of zero normal pressure gradient in super- and hypersonic boundary layer theories.

Part two deals with the present experimental study of hypersonic flow on concave and convex models. The facilities and models are described and the experimental results are interpreted.

Part three contains the theoretical investigation made in this study. This part is divided into two sections. In the first section two of the compressible boundary layer theories are described briefly. These methods are due to Sells (computer programme) and to Luxton and Young (momentum integral method). The second section deals with viscous interaction theory. Cheng's theory is analysed and solved for curved surfaces including power-law-bodies. The asymptotic behaviour of Cheng equation is examined for small and large arguments. Modifications of Cheng's method due to Sullivan and Stollery are also discussed and applied to a variety of surfaces.

Part four contains the results and discussion of the present experimental and theoretical investigations. Measurements of surface pressure distribution, heat transfer rate, boundary layer thickness, and shock shape are compared with the viscous interaction theories and with the first order boundary layer theories.

1. REVIEW OF BOUNDARY LAYER THEORY

1.1. Incompressible and compressible boundary layers

The concept of the boundary layer, one of the corner-stones of modern fluid dynamics, was introduced by Prandtl (1904) in an attempt to account for the sometimes considerable discrepancies between the predictions of classical inviscid incompressible fluid dynamics and the results of experimental observations.

Boundary layer theory has contributed a great deal to our understanding of incompressible aerodynamics, and will no doubt prove equally important for compressible and hypersonic flow problems. Its application however in the calculation of the flow round any given body is likely to be much less straightforward if the fluid is compressible, partly because then boundary layer theory is itself more complex, and partly because compressibility introduces new types of possible interaction between external and boundary layer flow.

As is well known, when an incompressible fluid flows round a body of suitable (streamlined) shape at a high enough Reynold's number, the important effects of viscosity on the flow are confined to a relatively small region consisting of a narrow wake behind the body and a thin layer, the boundary layer, next to its surface. Two important consequences follow from the thinness of the boundary layer. Firstly there can only be small pressure changes through the boundary layer in a direction normal to the body surface. Therefore the pressure distribution is governed by the external flow, which is unaffected by viscosity. Secondly, the external flow is practically identical with the flow of a theoretical inviscid incompressible fluid round the body. This enables conditions in the boundary layer to be calculated, providing there is no separation, so that the flow round the body can in theory be completely predicted.

In incompressible flow the momentum and energy equations are uncoupled, so that the momentum equation is independent of the temperature field. Blasius (1908) was one of the first persons to solve the boundary layer equations for flow parallel to a semi-infinite flat plate and obtained accurate results. There are now a great number of well established theories dealing with incompressible boundary layers.

With a compressible fluid, different kinds of interactions between boundary layer and external flow can occur. It remains true that in many cases of interest the important viscous effects are confined to a thin layer near the wall. But conditions in the boundary layer cannot necessarily be correctly predicted on the basis of the inviscid flow pressure distribution even when this indicates favourable pressure gradients everywhere so that separation does not occur. For example the pressure rise in a trailing edge shock, may be diffused upstream in the subsonic part of the boundary layer, which may thicken, appreciably or possibly separate as a consequence, so altering the local pressure distribution. The alteration may be large even without separation, for in supersonic flow a very local change in the direction of the external flow can cause an important pressure change at the point in question. Often however the interactions between external flow and boundary layer are minor and the viscous region may then be considered as thin and the displacement effect neglected as is in subsonic flow.

The essential difficulty in dealing with compressible laminar boundary layers is that the momentum and thermal energy equations are coupled, since the temperature field influences the density, which in turn influences the velocity field. Mathematically speaking we are faced with the task of solving two simultaneous non-linear partial differential equations. For this reason the only flow which has been considered in detail over a wide range of conditions is that when there is zero pressure gradient. Even here suitable assumptions are made concerning the value of the Prandtl number and the variation of viscosity with temperature.
E.R. Van Driest (1952) has used Crocco's method for

solving the compressible boundary layer equations on a flat plate and has presented the skin-friction and heat transfer coefficients as functions of Reynolds number, Mach number, and wall-to-free-stream temperature ratio.

The case with both pressure gradient and heat transfer is by far the most difficult to deal with theoretically. The problem becomes even more difficult if the wall temperature is not uniform, a situation which could arise in practice at very high speeds. The mathematical and numerical difficulties encountered in solving these equations are such that, even with the assistance of modern high-speed computing machines, very few precise numerical solutions for special cases have been attempted, and some of these are of doubtful accuracy.

Numerical finite-difference integration offers the only 'exact' method of solution of the general first order boundary layer problem; any other approach utilizes approximations and assumptions of some kind.

Finite-difference schemes have been subject to much development in recent years. Sells (1966) has recently published a very advanced programme, solving the equations in which no simplifications are made beyond two-dimensional steady flow of a perfect gas in equilibrium. The Prandtl number is assumed to be constant but not necessarily unity. We shall apply the programme to our model and will examine how well it can predict experimental results for an adverse pressure gradient with wall cooling. Fitzhugh (1968) has used the programme to compute the boundary layer properties for a variety of problems and the reader is referred to his paper for details.

Similar solutions for compressible laminar boundary layers with pressure gradient and heat transfer were calculated by Cohen and Reshotko (1956a) and these solutions were subsequently used (1956b) as the basis of an approximate method for general use.

In many cases the assumption of unit Prandtl number and linear viscosity-temperature variation are made to simplify the equations. Young (1949) employs a generalized Pohlhausen method to study the effects of changing Pr and ω where Pr is Prandtl number and ω is the index in the temperature-viscosity law $\mu = KT^{\omega}$. This method which for adiabatic wall, was later extended by Luxton and Young (1960) for use when there is heat transfer.

In all these cases the assumption is made that there is no normal pressure gradient. Kepler and O'Brien (1962), McLafferty and Barber (1959), and Michel (1961) have measured static pressure in turbulent boundary layers on concave walls and Myring and Young (1968) have compared the isobars in those three experiments to the external Mach line extrapolated into the boundary layer. Myring and Young have shown that static pressure is constant along Mach lines, and not along normals to the surface. Therefore, strong normal pressure gradients may exist on surface normals.

The above considerations leave no doubt that normal pressure gradients are important. The absence of normal pressure gradients removes the y-momentum equation, and makes it possible to transfer the compressible boundary layer equations to the incompressible plane. No-one has yet transformed the compressible boundary layer equations, with normal pressure gradient terms included, to the corresponding incompressible equations.

1.2. Hypersonic boundary layers

At low speeds the processes of viscous dissipation and heat conduction are restricted to a relatively thin boundary layer near the surface of the body. This layer may be considered as a region distinct from the external inviscid flow.

At hypersonic speeds decelleration of the freestream by shock waves or by viscous processes in the boundary layer can produce very high temperatures. As a result of this the boundary layer thickness is sufficiently big to change the effective body shape. This, in turn, alters the external pressure distribution which governs the growth of the boundary layer. This mutual influence is termed viscous interaction.

Another type of interaction associated with large boundary layer thickness is vorticity interaction. This kind of interaction is significant if the shock wave is highly curved, i.e. flow round blunt bodies. The effect of vorticity interaction can often be neglected for surfaces with sharp leading edges.

The most important practical question involving viscous effects at hypersonic speeds is usually the magnitude of the heat transfer to the body.

Lees (1956) observed that the thermal boundary layer at hypersonic speeds is rather insensitive to pressure gradient, particularly if the boundary layer is cooled. He then reduced the equations of motion to those for an equivalent flat plate flow, for which a self similar solution exists if the wall-to-stagnation temperature ratio is constant along the plate. Making use of this solution, boundary layer thickness and heat transfer coefficient can be expressed in terms of the external pressure distribution. Lees' method is usually called "local flat plate similarity".

For more details the reader is also referred to Hayes and Probstein (1959a) and Cheng (1960).

Cheng (1960) used Lees' local flat plate similarity solution in combination with the Newtonian-Busemann pressure law based on the effective body shape, and developed a theory which considered interaction between different parts of the flow. In his viscous interaction theory he considered the effects of incidence, bluntness and displacement, both separately and in combination.

Cheng applied the method to flat plates and compared the results with experimental data. The comparison between the viscous interaction theory and experimental data appear to be very good in the strong viscous interaction regions.

The simplicity of Cheng's viscous interaction theory and its good prediction of heat transfer and surface pressure distribution near the leading edge of a flat plate - strong viscous interaction region -, encouraged us to modify and apply this method to concave and convex surfaces.

2. EXPERIMENTAL WORK

2.1. The hypersonic Gun Tunnel

The measurements were made using the hypersonic No. 1 gun tunnel in the Aeronautics Department of Imperial College. Stollery et al (1960) and Needham (1963) describe this facility and its capabilities. Essentially, it is a blow-down tunnel with a piston drive shock compression heater. Cold compressed air is used to accelerate an aluminium piston down the length of the barrel. The piston acceleration generates a shock which compressed and heats the working gas. Multiple shock reflections off the barrel end, further compress and heat the working gas. The heated high pressure gas then passes through a convergent divergent nozzle which accelerates the gas to the required Mach number. By varying the ratio of the barrel pressure to the driver pressure the unit Reynolds number of the mainstream flow could be changed.

The Gun Tunnel can be fitted with a conical nozzle with variable throat size for Mach numbers 7, 9 and 15.1. The nozzles for M = 8.2 and 12.25 were contoured. The Mach 8.2 nozzle was calibrated by Opatowski (1967) and the Mach 12.25 by the present author. Details of the calibration of the Mach 12.25 nozzle are included below.

The useful running time of the tunnel was about 20 milli-seconds, during which time the model surface temperature rose a few degrees.

2.2. Calibration of the Mach 12 contoured nozzle

2.2.1. Introduction

The nozzle was manufactured by the electro-forming process using a two-piece aluminium alloy mandrel split at the throat. The electroform comprised a deposit of nickel .030" thick on the inner surface followed by a copper layer nominally .25" thick, built up locally in the throat region to .75" thick. The overall dimension of the nozzle are approximately 36" long by 9" exit diameter.

The nozzle profile was designed using the method of Hall (1961), (ARC 23,347), to determine the transonic flow characteristics of the throat of given radius to a Mach number of between 1.05 and 1.1, thus giving a starting line for the characteristics solution. For this, the Mach number distribution down the centre line was specified in the form of a cubic fitted to the Mach number and first and second derivatives at the starting line and Mach number and zero gradient at the exit.

The resulting inviscid contour was corrected for viscous effects by the addition of an estimated displacement thickness. The boundary layer calculation was based on Stratford and Beavers (1961) assuming a fully developed turbulent boundary layer with zero heat transfer, originating at a point one throat diameter upstream of the throat.

A contraction profile was then fitted mathematically ensuring that the first, second and third derivatives of the profile ordinates were smooth through the region of the throat.

2.2.2. Tests made

A pitot-pressure survey was made with a rake placed on the vertical diameter in the jet. Readings were taken at $x = 0, 2.5, 4.0, 5.5$ and 8, where x is the distance downstream of nozzle exit in inches. Readings on the horizontal diameter were made at $x = 0$ and 4 inches.

The above survey was for the normal running condition of $p_4 = 2000$ psig and $p_1 = 14.7$ psia. Readings were also taken for $p_4 = 2000$ psig; $p_1 = 25$ psia and $p_4 = 1000$ psig; $p_1 = 14.7$ psia .

The accuracy of the Mach number derived from the measured pitot pressure is about $\pm 0.5\%$.

2.2.3. Results and discussion

Results of pitot pressure measurements and the derived Mach number have been plotted for different driver to barrel pressure ratios. Figure (1) represents the pitot pressure distribution across the vertical diameter of the nozzle at different distances from the nozzle exit plane. Figure (2) shows the corresponding Mach number distributions. The pressure distribution across the horizontal diameter at nozzle exit is plotted in figure (3). Figure (4) shows the axial Mach number distribution. The Mach numbers plotted are average values taken from the uniform core regions indicated by the vertical distributions, e.g. figure (2).

From the pressure distribution in figure (1) and (3) it can be seen that the usable test region is not quite symmetric about the centre line of the nozzle. The useful test core is about 4.5 to 5.0" in diameter. It may be noted here that the flow was quite steady in the central core but there was some unsteadiness at the edge of the nozzle boundary layer, particularly at the high Reynolds numbers.

Within the accuracy of the test, the flow was steady at a Mach number of about 12.25. This was taken from the Mach number distribution in figure (2). The Mach number gradient along the central line in test section is 0.015 per inch. In contrast to the Mach 8.2 nozzle, there was no focusing effect on the centre line. The results obtained at the off design stagnation conditions, indicated a slight reduction in Mach number.

A typical trace of pitot pressure distribution is shown in figure (5). The traces of all running conditions are of the same form. The running time for constant stagnation condition is about 20 msec.

Schlieren photographs taken of the flow past the rake were perfectly normal. The nozzle was found to function perfectly satisfactorily with a relatively large flat plate-wedge model in the test section. The fact that the test Mach number did not change was checked by measuring the pitot pressure with the model in position, as in figure (6).

2.3. Pressure measurements

Surface pressure measurements were made using strain gauge transducers. The calibration of the transducers was carried out by putting them in the working section of the tunnel and sucking down to a vacuum (about .1 mm Hg) and monitoring the output of the transducers with a digital voltmeter as the vacuum was relieved. The pressure was measured on a McCleod gauge with a cold trap between it and the working section. In this manner, the individual calibration of each transducer was established.

2.4. Heat transfer measurement

The heat transfer gauges are used essentially as thin film platinum resistance thermometers to measure the surface temperature during the run. The gauges are coupled into a Wheatstone bridge circuit and the out-of-balance voltage due to the change in resistance of the gauges with temperature is amplified and fed into an electronic analogue circuit which, in fact, solves the thermal diffusion equation to give the heat transfer rates as a function of time. Full details of the theory and development of the electronic apparatus have been reported by Hunter (1969) and Holden (1964).

2.5. Flow visualization

Flow visualization was obtained using a conventional single pass schlieren system. The concave spherical mirrors were arranged to give an amplification factor of 0.8. Either Ilford fast blue sensitive plates or a normal polaroid camera could be used to record the resulting image.

The knife edge was set parallel to the flow for all cases studied.

The spark source utilized a 1 μf electrolytic capacitor charged up to 12 kv which discharged over a gap of 1.2 inches in an argon atmosphere of approximately 10 psi gauge pressure. By suitable settings on the time delay unit, the spark was initiated once steady flow conditions were achieved over the model.

2.6. Model construction

2.6.1. Concave model

The model contour chosen for the experiments obeys the following equation in axes originating at the leading edge:

$$y = x^3/150 \quad \text{for} \quad x < 5.1''$$

$$dy/dx = 28^0 \quad \text{for} \quad x \geq 5.1'' .$$

The overall dimensions are shown in figure (7), which also contains a layout of heat transfer gauges and pressure tappings.

The pressure model was originally built for Sullivan (1963) and is described by him. The model was subsequently used by Fitzhugh for a series of experiments at Mach 15.1 using the conical nozzle. It was then decided to use this model as compression surface for our experiments. The pressure and heat transfer models are shown in figure (8).

2.6.2. Convex model

The convex model was an 18° wedge followed by a convex fairing to flat plate. The equation of the fairing was

$$g = 0.00269s^4 - 0.0211s^3$$

g and s are shown in figure (9).
The first and second derivatives are therefore matched at the joins with the straight sections. The model had a span of 4" and a leading thickness of $t = .001$ inches. The overall dimensions of the model and a layout of the pressure tappings and heat transfer gauges are shown in figure (9).

The pressure model consisted of 56 tappings with a tapping spacing of .3". By fitting the transducers into cylindrical mountings made in the support of the model, it was possible to keep the communicating volume as small as possible. The transducers were linked to the model pressure tappings by means of $^1/_{16}$" bore plastic tubing, the typical pipe length being 3 to 4 inches. When not in use, the stub-pipes of the pressure tappings underneath the model were sealed with small caps made from heat-sealed plastic tubing. The sting mounting of the pressure transducers is shown in figure (10).

The heat transfer model is shown in figure (12). Pyrex glass $^1/_{16}$" thick served as the backing material in preparation of thin film gauges. Pyrex glass was cut to the required size and dipped into the melted wax, so that the plate was covered with a somewhat uniform layer of wax. A metal template was made with gauge locations marked on it and then holes with a size of $^1/_{16}$" were drilled at the end of locations. Subsequently the template was put on top of the pyrex and removed the wax by pushing a hypodermic tube through the holes. The resulting plate was then immersed into a 40% solution of hydrofluoride acid for $2\frac{1}{2}$ hours. After the etching process the pyrex was thoroughly washed and the wax was carefully removed from the surfaces. With the Mullard Ultrasonic Drill .020" holes were drilled in the etched holes. The reason for the etching was to achieve a smooth transition from the surface of the pyrex to the holes.

Prior to the painting of the gauges on the pyrex between the holes, the pyrex glass was heated to its plastic temperature (680°C) and annealed for three hours. In doing this any stresses present in the pyrex plate were relieved. The gauges were painted between the holes using acetone diluted Hanovia X-05 platinum paint. The subsequent dried pyrex was heated to 680°C and annealed at 550°C for a few hours. At this temperature pyrex becomes soft, so that platinum can partially sink into the glass. In order to make the gauges more abrasion-resistant the painting and baking cycles were repeated 4 or 5 times until a resistance of around 50 ohms was obtained.

A total of 71 film gauges were put on the pyrex plate using the technique outlined above. For further information see also Holden (1964) and Hunter (1968).

Silver connecting leads were baked into the holes at the end of each gauge, thus enabling the connecting leads to be installed on the under-side of the pyrex plate.

Prior to the connection of the leads the plate was bent, by heating and letting it sag into a mold*. The original pressure model served as a template to make the mold for the bending process. Several "Pyrex" plates were prepared and bent, from which the best one was chosen which conformed very accurately to the desired contour, with no bumps or discontinuities in slope.

---

* The Bending was carried out by the firm of John Bowton Ltd., Glass benders, 79-81 Highgate Hill, London, N.19. Tel. ARCway 5586.

Finally a support for the pyrex plate was made which had a steel leading edge back to $x = 3''$. The support had deep slots cut into it to take wires out the rear, and after the plate was mounted onto this support, melted wax was poured into the slots to hold the plate firmly and give it uniform support. The two convex models, pressure and heat transfer, are identical in shape, contour, etc. Thus one can be substituted for the other without changing flow patterns in the tunnel working section.

The resistance-temperature coefficient of each gauge α was calibrated by measuring resistances at different temperatures in a bath. The factor ρck was taken constant for pyrex, assuming that there is no diffusion of silver or platinum into the substrate. In fact any insulator with known properties can be taken as substrate.

2.7. The test conditions

The flow over the cubic concave model separated at Mach 8.2, even at the lowest Reynolds number attainable. Therefore measurements on the cubic model were restricted to $M = 12.25$ with the following test conditions:

$$p_o = 1600 \ ^{lb}/in^2$$

$$T_o = 1300 \ ^oK$$

$$Re/'' = 0.86 \times 10^5$$

The convex model was tested at both Mach numbers 8.2 and 12.25. The test conditions are summarized below.

At $M = 12.25$

$$p_o = 1600 \ ^{lb}/in^2$$

$$T_o = 1300 \ ^oK$$

$$Re/'' = .86 \times 10^5$$

$$p_o = 800 \ ^{lb}/in^2$$

$$T_o = 1037 \ ^oK$$

$$Re/'' = .644 \times 10^5$$

At $M = 8.2$

$$p_o = 1600 \ ^{lb}/in^2$$

$$T_o = 1300 \ ^oK$$

$$Re/'' = 2.4 \times 10^5$$

$$p_o = 1200 \ ^{lb}/in^2$$

$$T_o = 1185 \ ^oK$$

$$Re/'' = 2.07 \times 10^5$$

Mach numbers behind the leading edge oblique shock were theoretically 4.8 and 4.25 at Mach 12.25 and Mach 8.2 respectively.

The heat transfer and pressure transducer output voltages were displayed on Tektromix type 502 oscilloscopes and recorded using Land Polaroid cameras.

2.8. Experimental Results

The flow over the models at both Mach numbers was attached and laminar as judged from the schlieren photographs and heat transfer traces. Schlieren pictures of the flow over both models at different

Mach numbers are shown in figures 13-16.

The pressure and heat transfer results for the cubic concave model at $M = 12.2$ are shown in figures 17, 18 and 19 and in tables 1-3. The pressure tappings in the model were extended to within .5" of the leading edge.

Side plates were used to test the two-dimensionality of the flow. It was found that side plates caused the boundary layer to separate, which was observed in schlieren photographs, when using small side plates. However, spanwise heat transfer measurement shown in figure (19) indicates that the flow two-dimensionality over the cubic surface was reasonably good. Further discussion and comparison of pressure and heat transfer results for the cubic model is given in chapter 4.

We shall also make use of the measurements taken by Fitzhugh (1968) at Mach 15.1. Since these measurements were obtained in a conical nozzle which had a Mach number gradient, ($M(x) = 15.1 + 0.215x$, x in inches) the static pressure was taken as that in the undisturbed local conical flow, and thus the static pressure p is a function of x .

The pressure and heat transfer results to the convex surface are shown in figures 40, 41, 43, 44 and 45. Typical pressure and heat transfer traces are shown in figure 11. The surveys were made at Mach 8.2 and 12.25 with different stagnation conditions. Surface pressure measurements were made to within .3" of the leading edge. As mentioned before the Mach 8.2 nozzle focussed the discontinuities on the centre line, therefore the scatter in the experimental data near the leading edge at this Mach number is due to the focussing effect of the 8.2 nozzle. The model was set in the test section above the centre line in order to avoid the focussing region, but that caused blockage in the test section, because of the relatively large size of the model.

Spanwise heat transfer measurements at stations 2, 5 and 8 inch from the leading edge, presented in figure (20), indicate that the heat transfer is almost constant across the convex model indicating that the flow is reasonably two-dimensional.

For further discussion of the experimental data obtained for the convex model, the reader is referred to part 4 of this study.

3. THEORY

3.1. Introduction

Following there are the equations governing the steady two-dimensional motion of a compressible fluid in a thin boundary layer on a curved surface.

(i) Continuity equation

$$\frac{\partial(\rho u)}{\partial x} + \frac{\partial(\rho v)}{\partial y} = 0 \tag{3.1.1}$$

(ii) x-momentum equation

$$\rho\left(u\frac{\partial u}{\partial x} + v\frac{\partial u}{\partial y}\right) = -\frac{\partial p}{\partial x} + \frac{\partial}{\partial y}\left(\mu\frac{\partial u}{\partial y}\right) \tag{3.1.2}$$

(iii) y-momentum equation

$$0 = \frac{\partial p}{\partial y} \tag{3.1.3}$$

(iv) Equation of state

$$p = \rho R T \tag{3.1.4}$$

(v) Energy equation

$$\rho Cp\left(u\frac{\partial T}{\partial x} + v\frac{\partial T}{\partial y}\right) = u\frac{dp}{dx} + \frac{\partial}{\partial y}\left(k\frac{\partial T}{\partial y}\right) + \mu\left(\frac{\partial u}{\partial y}\right)^2 \tag{3.1.5}$$

In arriving at these equations it is assumed that the viscous region of the flow is confined to a thin layer, i.e. the Reynolds number is large.

3.2. Sell's computer programme

Sell's (1966) computer programme solves the first order boundary layer equations, mentioned above, assuming only a perfect diatomic gas of constant Prandtl number, not necessarily unity. The inviscid solution over the body in question is specified before calculation begins. Sells employs an implicit finite-difference scheme and an estimation of the non-linear terms for the solution of the two coupled non-linear partial differential equations. The resulting non-homogeneous linear equations are solved by matrix inversion, the non-linear terms are re-evaluated and the process is repeated until the solution converges to within some pre-set limit. The programme then marches downstream utilising the parabolic nature of the equations. Typically two hundred points are taken across the boundary layer. The programme is capable of integrating close to separation and usually fails to converge at some point less than one step length from the extrapolated separation point. Occasionally the programme integrates one step length beyond separation, but errors in calculation using a reversed flow velocity profile are thought to be so great that convergence cannot be obtained any further downstream. Other methods are needed to march past this point.

3.3. Luxton and Young's Method (1962)

This method is essentially a generalization of the Pohlhausen procedure. It was originally developed by Young (1949) for the case of zero heat transfer, but was later generalized and developed by Luxton and Young (1962) for use when there is heat transfer. The method is applicable for arbitrary values of Pr and ω, where Pr is Prandtl number and ω is power index of the viscosity temperature relationship $\mu \sim T^{\omega}$. The method assumes that the velocity profile is of the form

$$u = aY + bY^2 + cY^3 + dY^4$$

where $$Y = \int_0^y \frac{\mu_1}{\mu} \, dy$$

and a, b, c and d are chosen to satisfy the boundary condition and are all functions of the pressure gradient form-factor Λ. The form parameter $H(= \delta_1/\delta_2)$ and the ratio of total boundary-layer thickness to momentum thickness $f(= \delta/\delta_2)$ are not chosen from the assumed velocity profile but are taken to be functions of Λ, wall temperature T_w and of the flow properties at the edge of the boundary layer. They then integrate the momentum equation for the skin friction coefficient from which heat transfer rate can be calculated using Luxton (1967).

3.4. Viscous Interaction

So far we have considered the classical first order theories which are valid for thin boundary layers. Laminar boundary layer growth at hypersonic speeds can severely distort the external flow field, which in turn reacts to modify the boundary layer growth. A good example of such viscous interaction is the flow near the leading edge of a flat plate where the boundary layer growth gives rise to a strong, curved oblique shock-wave followed by an expansion fan. The surface pressure distribution is then entirely different to the inviscid prediction. Rapid changes of boundary layer growth will also occur in regions of strong pressure gradient and thus the effective body shape is no longer the surface of the body, but surface of the body plus displacement thickness. Therefore the viscous interaction effects must be considered as important as the first order effects in any boundary layer calculation involving a thick layer.

Three sets of equations are required to represent this type of flow: Boundary layer equations, inviscid flow equations and a coupling equation. These equations can be summarized in the following 3 functions

$$\delta^* = f_1(p_e) \qquad (3.4.1)$$

$$p_e = f_2(y_e) \qquad (3.4.2)$$

$$y_e = f_3(\delta^*) \qquad (3.4.3)$$

Hence a complete solution for the flow over a given shape $(y_w \sim f(x))$ is possible once methods of estimating boundary layer growth, external pressure distribution and effective body stream line have been found.

(i) <u>Boundary layer equations</u>

A method is needed to predict the boundary layer growth over a body. There are many methods predicting the boundary layer growth δ^*, but one very simple and useful method is Lees (1956) local flat plate similarity which is given by Cheng (1960) as

$$M \frac{\delta^*}{x} = \overline{\chi}_\varepsilon \left[\int_0^x \frac{p}{p_\infty} \frac{d\xi}{x} \right]_x^{\frac{1}{2}} \left[\frac{p}{p_\infty} \right]^{-1} \qquad (3.4.4)$$

where

$$\bar{\chi}_\varepsilon = .664\left(\frac{\gamma-1}{\gamma+1}\right)\left(1+2.6\frac{T_w}{T_o}\right)\bar{\chi} \qquad (3.4.5)$$

and $$\bar{\chi} = M^3\sqrt{C/Re_x} \qquad (3.4.6)$$

$\bar{\chi}$ is the viscous interaction parameter, T_w and T_o are wall- and total temperature respectively. C is the constant of proportionality in the linear viscosity-temperature relation. Cheng (1960) gives the following expression for C .

$$C = [\mu(T_*)/\mu(T_\infty)](T_\infty/T_*) \qquad (3.4.7)$$

where $$T_* = T_o[1+3(T_w/T_o)]/6 \qquad (3.4.8)$$

An alternative method of predicting boundary layer growth, is the method due to Sells (1966), which was described earlier.

(ii) Inviscid equations

There are many approximate methods for hypersonic inviscid calculation which relate the surface pressure to the body slope, i.e. to the slope of the effective body shape (body plus displacement thickness). Three such methods are

a) Newton-Busemann

$$p_e/p_\infty = \gamma M_\infty^2 (y_e'^2 + y_e\, y_e'') \qquad (3.4.9)$$

b) Newtonian approximation

$$p_e/p_\infty = 1 + \gamma M_\infty^2 \left(\frac{dy_e}{dx}\right)^2 \qquad (3.4.10)$$

c) Tangent-wedge approximation

$$p_e/p_\infty = 1 + \gamma k^2 \left[\frac{\gamma-1}{4} + \left\{\left(\frac{\gamma+1}{4}\right)^2 + \frac{1}{k^2}\right\}^{\frac{1}{2}}\right] \qquad (3.4.11)$$

where $k = M_\infty \dfrac{dy_e}{dx}$.

An alternative to these approximations, other methods such as the method of characteristics may be used for the inviscid pressure calculation.

(iii) Coupling equation

The coupling equation accounts for the interaction between the two flow regions. A simple method of coupling these types of flows is

$$y_e = \delta^* + y_w \qquad (3.4.12)$$

which states that the effective body shape is the body's coordinate y_w plus the displacement thickness. Here the assumption is made that y_e is the solid body surface.

A more precise and complex coupling equation is used by Lees and Reeves (1964) in the calculation of the viscous interaction of supersonic separated boundary layers.

Any of the suggested expressions for the boundary layer, inviscid and coupling equations can be combined to yield solutions to viscous interaction problems.

3.4.1. Cheng's method

Combining Lees local flat plate similarity solution for the boundary layer growth with the Newton-Busemann inviscid equation and the simple coupling equation (3.4.12), gives:

$$(y_e - y_w)[\sqrt{y_e\ y_e'}\ ]' = \frac{\bar{\chi}_\varepsilon \sqrt{x}}{2\sqrt{\gamma}\ M^2} \qquad (3.4.13)$$

This equation agrees with Cheng's equation except for $\sqrt{\gamma}$ replacing unity in the denominator.

Equation (3.4.13) can be solved numerically from the origin for any given shape y_w. Since the right hand side of the equation (3.4.13) is a constant, it can be reduced to unity by appropriate scaling. For a family of shapes $y_w \sim x^n$ we may write

$$\frac{y_w}{a\ell} = \left(\frac{x}{\ell}\right)^n \tag{3.4.14}$$

or

$$z_w = \xi^n \tag{3.4.15}$$

Replacing y and x in the equation (3.4.13) by $a\ell z$ and $\xi\ell$ respectively we obtain the following scaled equation

$$(z-\xi^n)(\sqrt{zz'})' = 1 \tag{3.4.16}$$

with

$$\ell = \frac{\chi_\varepsilon^2}{4\gamma a^4 M^4} \tag{3.4.17}$$

From the scaling factor ℓ, it is immediately apparent that the important parameter which controls the relative importance of the effects of incidence and viscous interaction, is

$$M^2\alpha^2/\bar{\chi}_\varepsilon \tag{3.4.18}$$

The joint-effects of incidence and displacement thickness $M^2\alpha^2/\bar{\chi}_\varepsilon$ are of particular interest to our investigation. The physical significance of this parameter can also be seen from a comparison between the pressure distribution due to strong viscous interaction

$$p/p_\infty = \frac{3}{4}\sqrt{\gamma(\gamma+1)}\quad\bar{\chi}_\varepsilon \tag{3.4.19}$$

and that due to incidence

$$p/p_\infty = \frac{\gamma(\gamma+1)}{2}M^2\alpha^2 \tag{3.4.20}$$

On regions of the body where $\bar{\chi}_\varepsilon \gg M^2\alpha^2$ viscous interaction will dominate, but in regions where $M^2\alpha^2 \gg \bar{\chi}_\varepsilon$ the incidence effect will be the more important and the inviscid pressure distribution may be a sufficiently accurate estimate of the real situation.

For a flat plate at zero incidence, equation (3.4.16) reduces to a simpler form of

$$z\left(\sqrt{z z''}\right)' = 1 \qquad (3.4.21)$$

with
$$\ell = \frac{\overline{\chi}_{\varepsilon}^{2}}{4\gamma M^{4}} \qquad (3.4.22)$$

Equation (3.4.21) can be solved analytically to give the strong viscous interaction solution

$$z = \left(2\sqrt{2}/3^{1/4}\right)\,\xi^{3/4} \qquad (3.4.23)$$

Equation (3.4.16) reveals a singular behaviour at the origin and admits the solution $z \sim \xi^{3/4}$ as $\xi \longrightarrow 0$. This is the behaviour to be expected when the displacement effect predominates, Lees (1953), Stewartson (1955). With the asymptotic solution for $\xi \longrightarrow 0$, solution to the equation (3.4.16) can be obtained by a forward integration from the origin using Runge-Kutta or Predictor-Corrector methods.

Asymptotic solution to the equation (3.4.16) for $\xi \longrightarrow 0$ gives

$$z = \frac{2\sqrt{2}}{3^{1/4}}\,\xi^{3/4} + \frac{3}{8n^2+2n}\,\xi^n + \ldots \qquad (3.4.24)$$

the derivation of this equation can be found in appendix A. The first term in the above solution is the flat plate solution at zero incidence and is the predominant term for $\xi \longrightarrow 0$. For $n > 1$ the second term in the solution can be neglected without introducing much error, firstly because as $\xi \longrightarrow 0$, ξ^n becomes much smaller than $\xi^{3/4}$ and secondly the coefficient of ξ^n decreases with increasing n . For $n = 1$ the equation (3.4.24) becomes

$$z = \frac{2\sqrt{2}}{3^{1/4}}\,\xi^{3/4} + \frac{3}{10}\,\xi + \ldots \qquad (3.4.25)$$

this equation is identical to Cheng's equation (2.22) for small argument of the variable. For $\xi = .001$ the second term in (3.4.25) is 10% of the first term and for $\xi = .0001$, it is only 1.5%.

Therefore for a sufficiently small argument the flat plate solution may be taken as the starting values with reasonable accuracy.

With the asymptotic solution as the starting value equation (3.4.16) can be integrated to yield z and its derivatives z', z''. In terms of the new variables z and ξ the required physical quantities are

$$\frac{p/p_{\infty}}{\gamma\alpha^2 M^2} = (zz')' \qquad (3.4.26)$$

$$\frac{\delta^*}{\alpha \ell} = (z - \xi^n) \qquad (3.4.27)$$

$$\frac{A\ St.}{4\gamma\alpha^3 . 0.332} = \frac{1}{z - \xi^n} \qquad (3.4.28)$$

where St. is the Stanton number.

Following we shall examine the asymptotic behaviour of Cheng's equation (3.4.16) for the power-law bodies $z_w = \xi^n$ as ξ approaches infinity.

3.4.1.1. Asymptotic solution of Cheng's equation for large arguments

For a family of shapes $z_w = \xi^n$ we

write the equation (3.4.16) again

$$(z-\xi^n)(\sqrt{zz'})' = 1 \qquad (3.4.16)$$

We now put

$$\Delta^* = z-\xi^n \qquad (3.4.29)$$

where Δ^* is the scaled displacement thickness

$$\Delta^* = \frac{\delta^*}{a\ell} \qquad (3.4.30)$$

By rewriting equation (3.4.16) in terms of Δ^* we obtain

$$\Delta^*[\sqrt{(\Delta^*+\xi^n)(\Delta^{*\prime}+n\xi^{(n-1)})}]' = 1 \qquad (3.4.31)$$

An aymptotic solution for Δ^* as $\xi \to \infty$ can be obtained if we assume that $\Delta^* \to 0$, which means that this analysis applies for concave surfaces only. For $\Delta^* \to 0$, $\xi \to \infty$ equation (3.4.31) can be rewritten as

$$\Delta^*[n\ \xi^{2n-1}]' = 2\sqrt{n\ \xi^{2n-1}} \qquad (3.4.32)$$

By differentiating the bracket and solving for Δ^* we obtain

$$\Delta^* = \frac{2}{\sqrt{n}(2n-1)}\,\xi^{3/2-n} \qquad (3.4.33)$$

From the equation (3.4.33) it is obvious that the assumption for Δ^* going to zero holds only for cases where $n > 3/2$. Therefore our analysis will be restricted to cases where $n > 3/2$. We might be able to find individual solutions for $n = 3/2$ and $n < 3/2$, but this is not attempted in the present work. Nevertheless, even for $n > 3/2$ asymptotic solution for large arguments will give us a broad idea how equation (3.4.16) behaves.

Equation (3.4.33) reveals another interesting phenomena. Decaying solutions of displacement thickness Δ^* exist only for $n > 3/2$ as $\xi \longrightarrow \infty$, i.e. there are some compression surfaces where the displacement thickness increases with increasing distance far from the leading edge. We shall discuss this characteristic in detail in the next chapter.

We now rewrite Δ^* as

$$\Delta^* = z-\xi^n - \frac{2}{\sqrt{n}(2n-1)}\,\xi^{3/2-n} \qquad (3.4.34)$$

and put it into equation (3.4.16) and obtain

$$\frac{1}{2}(\Delta^{*}+D\xi^{3/2-n})[(\Delta^{*}+\xi^{n}+D\xi^{3/2-n})(\Delta^{*\prime}+n\xi^{n-1}+E\xi^{1/2-n})]' =$$
$$[(\Delta^{*}+\xi^{n}+D\xi^{3/2-n})(\Delta^{*\prime}+n\xi^{n-1}+E\xi^{1/2-n})]^{1/2} \qquad (3.4.35)$$

where
$$D = \frac{2}{\sqrt{n}(2n-1)}$$
$$E = \frac{2(3/2-n)}{\sqrt{n}(2n-1)}$$

After differentiation we approximate the resulting equation for $\Delta^{*} \longrightarrow 0$ and $\xi \longrightarrow \infty$ and end up with following equation

$$\xi^{2}\,\frac{\partial^{2}\Delta^{*}}{\partial\xi^{2}} + \frac{2n+1}{2}\,\xi\,\frac{\partial\Delta^{*}}{\partial\xi} + \frac{n^{3/2}(2n-1)^{2}}{2}\,\xi^{2n-3/2}\,\Delta^{*} = 0 \qquad (3.4.36)$$

This is a second order ordinary differential equation with variable coefficients, which is identical with the generalized Bessel equation

$$x^{2}y''+x(a+2bx^{r})y'+[c+dx^{2s}-b(1-a-r)x^{r}+b^{2}x^{2r}]y = 0 \qquad (3.4.37)$$

with the oscillatory solution

$$y = x^{\frac{1-a}{2}} \cdot e^{\frac{-bx^r}{r}} \; y_\rho \left(\frac{\sqrt{d}}{s} \cdot x^s\right) \qquad (3.4.38)$$

and $$y_\rho = A_1 \, J_\rho + A_2 J_{-\rho} \qquad (3.4.39)$$

where $$\rho = \frac{1}{s} \sqrt{\left(\frac{1-a}{2}\right)^2 - c} \qquad (3.4.40)$$

Comparing equation (3.4.36) with (3.4.37) we clearly find that

$$b = 0 \quad ; \quad a = \frac{2n+1}{2}$$

$$c = 0 \quad ; \quad d = \frac{n^{3/2}(2n-1)^2}{2}$$

$$s = n-{}^{3}/_{4} \quad \text{and} \quad \rho = \frac{1-2n}{4n-3}$$

Hence

$$\Delta^* = \xi^{\frac{1-2n}{4}} \left[A_1 J_\rho(X) + A_2 J_{-\rho}(X) \right] \qquad (3.4.41)$$

where $$X = 2\sqrt{2}\, \frac{n^{3/4}(2n-1)}{4n-3}\, \xi^{n-3/4} \qquad (3.4.42)$$

and A_1 and A_2 are constant.

Equation (3.4.41) clearly demonstrates the oscillatory behaviour of Δ^* for large arguments. For $n \leq {}^{3}/_{4}$ equation (3.4.36) reduces to the

Cauchy differential equation which has a non-oscillatory solution. For $n > 3/4$ equation (3.4.41) gives an oscillatory solution for Δ^*. Although equation (3.4.41) gives an oscillatory solution to Δ^* for $n > 3/4$, it is valid only for $n > 3/2$, as discussed earlier.

3.4.2. Modified Cheng's method

Alternative pressure laws can be used instread of the Newton-Busemann law employed by Cheng. If we now combine Lees local flat plate similarity solution for the boundary layer growth, equation (3.4.4), with the tangent-wedge approximation (3.4.11) and the coupling equation (3.4.12) we obtain the following two simultaneous differential equations, as shown by Stollery (1970).

$$\frac{dP}{dX} = \frac{P^2}{2R}\left\{1+2R^{\frac{1}{2}}\left[M\frac{dy_w}{dx} - \frac{(P-1)}{\gamma\left[1+\frac{\gamma-1}{2\gamma}(P-1)\right]^{\frac{1}{2}}}\right]\right\} \qquad (3.4.43)$$

$$\frac{dR}{dX} = P \qquad (3.4.44)$$

where $P = p_e/p_\infty$ (3.4.45)

and $X = \frac{x}{L} = (A\bar{\chi})^{-2}$ (3.4.46)

$A\bar{\chi}$ differs slightly from the $\bar{\chi}_{\varepsilon}$ given by Cheng, by a factor of $A\bar{\chi}/\bar{\chi}_{\varepsilon} = (\gamma+1)/2$.

With known initial conditions X_o, R_o and P_o , a solution to equations (3.4.43) and (3.4.44), for a given body shape, can be found using Runge-Kutta or Predictor-Corrector techniques. In the strong interaction limit $\bar{\chi} \longrightarrow \infty$ or $X \longrightarrow 0$, $P \longrightarrow \infty$. Therefore to start the integration we must solve the equation (3.4.43) for strong interaction as $X \longrightarrow 0$. This can be done by simplifying (3.4.43) with the approximation $P >> 1$ to obtain

$$\frac{dP}{dX} = \frac{P^2}{2R} \left[1 - \frac{4R^{\frac{1}{2}}P^{\frac{1}{2}}}{\sqrt{2\gamma(\gamma+1)}}\right] \qquad (3.4.47)$$

Now by assuming a solution of the forms $P = kX^n$ we find that

$$P = \frac{3}{4}\,\gamma(\gamma+1) \quad X^{-\frac{1}{2}} \qquad (3.4.48)$$

or

$$P = \frac{3}{4}\,\gamma(\gamma+1) \quad A\bar{\chi} \qquad (3.4.49)$$

Solution of equations (3.4.43) and (3.4.44) leads to a pressure distribution $P = P(X)$.

Using Lees expression for boundary layer growth δ^* and Stanton number St., give:

$$\frac{M\,\delta^*}{L} = \frac{\sqrt{R}}{P} \tag{3.4.50}$$

$$\frac{AM^3 St.}{0.332} = \frac{P}{\sqrt{R}} \tag{3.4.51}$$

For a family of shapes $Y_w = X^n$ equation pair (3.4.43) and (3.4.44) can be modified to give

$$\frac{dP}{dX} = \frac{P^2}{2R}\left\{1+2R^{\frac{1}{2}}\left(M\alpha\,\frac{dY_w}{dX} - \frac{(P-1)}{\gamma\left\{1+\frac{\gamma-1}{2\gamma}(P-1)\right\}^{\frac{1}{2}}}\right)\right\} \tag{3.4.52}$$

$$\frac{dR}{dX} = P \tag{3.4.53}$$

For a given shape and given $M\alpha$ the equation pair can be solved for P . For a wedge body $\frac{dY_w}{dX} = 1$ and α is the wedge angle. Many cases have been studied and results are discussed in the next chapter.

Sullivan (1968) used the tangent-wedge approximation in his study of viscous interaction for flows over convex corners and found the same equation pair as above.

4. RESULTS AND DISCUSSION

4.1. General discussion

The governing equations for both Cheng's and modified Cheng's (Sullivan (1969), Stollery (1970)) methods have been solved for a family of concave and convex of the form $y_w \sim x^n$. The numerical computation was carried out using either an IBM 7094 or CDC 6600 machine. The computer programme due to Sells was run on the University of London Atlas computer.

Figure (21) shows the theoretical pressure and heat transfer predictions for a flat plate at zero incidence using the modified Cheng's method. This figure clearly demonstrates that by using the tangent wedge approximation in the viscous interaction analysis the resulting pressure distribution is applicable for both strong and weak interaction regions, whereas Cheng's method is strictly for strong interaction regions. The pressure curve asymptotes to both, strong interaction near the leading edge and weak interaction farther downstream.

Furthermore figure (21) demonstrates that for $(A\bar{\chi})^2 > 10$, the flow field on a flat plate is governed by strong viscous interaction, and for $(A\bar{\chi})^2 < 0.1$, viscous interaction can be considered weak.

The modified Cheng's method was also applied to a flat plate at incidence and the results are plotted in figure (22). This figure gives the pressure prediction as a function $1/(A\bar{\chi})^2$ with varying parameter $M\alpha$, where M is the free stream Mach number and α is the angle of attack. For $M\alpha = 0.0$ we have the case of a flat plate at zero incidence. As $M\alpha$ increases, the strong interaction region is pushed more towards the leading edge and pressure ratio asymptotes more quickly to its wedge value.

In the previous chapter we showed that the Cheng equation oscillates for large arguments for cases where we have adverse pressure gradient. This is confirmed by the results of numerical integration of the Cheng equation for concave surfaces. Figure (23) demonstrates clearly the oscillatory behaviour of the Cheng equation. Here the normalized pressure is plotted against the scaled length ξ for various shapes.

The Cheng equation does not oscillate for a flat plate at zero incidence because its analytical solution is a non-oscillatory one. Figure (23) shows that it does not oscillate for flat plates at incidence (n=1) either. But it is shown that the equation does oscillate for $n > 1$, i.e. compression surfaces. The boundary layer, dominated near the leading edge by displacement effects grows initially as though supported by a flat plate. Faced with the adverse pressure gradient downstream, the boundary layer and with it, pressure and heat transfer develop oscillations. The stronger the concave nature of a surface the higher is the frequency of the oscillations. The oscillations damp quickly in the downstream direction.

It appears that the Busemann centrifugal correction is far too powerful in the assumed pressure law. As the flow moves around the surface the dominant influence changes from displacement to incidence. This is very nicely demonstrated in figure (23). For small ξ or $A^2\overline{\chi}^2 >> a^4M^4$, the boundary layer is governed by displacement effect, therefore the pressure drops despite concave nature of the surface. For large ξ , $(\alpha^4 M^4 >> A^2\chi^2)$ the dominant effect is incidence and thus pressure should approach the inviscid value. Therefore

$$\frac{p_e}{p_\infty \gamma\alpha^2 M^2} = (z_w z_w')' \tag{4.1.1}$$

and with $z_w = \xi^n$ we obtain

$$\frac{p_e}{p_\infty \gamma\alpha^2 M^2} = (2n^2-n)\xi^{2n-2} \tag{4.1.2}$$

Equation (4.1.2) is valid for large ξ . For $n=1$, equation (4.1.2) reduces to

$$\frac{p_e}{p_\infty \gamma\alpha^2 M^2} = 1 \tag{4.1.3}$$

or

$$\frac{p_e}{p_\infty} = \gamma\alpha^2 M^2 \tag{4.1.4}$$

The equation (4.1.4) is the Newtonian approximation for a flat plate at an incidence α . For $n>1$, i.e. compression surfaces, the scaled pressure ratio approaches to the expression found in equation (4.1.2). This is in fact the equation of lines about which the pressure curves oscillate and appear as straight lines in figure (23). Similar analyses can be carried out for the boundary layer growth and heat transfer rate, since these are functions of pressure ratio.

Figure (24) shows the theoretical pressure prediction for convex surfaces $y_w = -ax^n$, when using Cheng's method. Near the leading edge the predictions asymptote to the flat plate value but unlike the case of concave surfaces, do not oscillate far downstream.

If Cheng's method is modified by replacing the Newton-Busemann pressure law by the more realistic tangent wedge rule the calculated p, $\dot{q}$ and δ^* do not exhibit any oscillatory behaviour. This is shown in figures (25) and (26), where the pressure rises steadily as the body slope increases. Regardless of values of n and M_α the boundary layer at the leading edge is governed by the displacement thickness. Further downstream where the body slope $\theta_b > \frac{d\delta^*}{dx}$ the boundary layer calculation is governed by the body slope.

In summary both methods describe broadly the main features of the flow. Near the leading edge the displacement effect is dominant $A\bar{\chi} >> M^2\alpha^2$ and the layer grows much as it would over a flat plate. Then as the surface slope increases so the incidence effect grows in importance, and the slope of the outer edge of the layer approaches that of the wall. It remains to look at the experimental evidence for confirmation or for suggestions of inadequacy. But before doing this we shall discuss the behaviour of hypersonic boundary layers in adverse pressure gradients.

4.2. Behaviour of the hypersonic boundary layers in a rising pressure gradient

In the previous chapter, in considering the asymptotic behaviour of the Cheng equation for large arguments we found that

$$\Delta^* = \frac{\delta^*}{\alpha \ell} \sim \xi^{3/2-n} \qquad (4.2.1)$$

This equation reveals that a decaying solution for the displacement thickness exists only if $n > 3/2$, i.e. Δ^* goes to zero for those concave surfaces of the form $y_w = a x^n$, if $n > 3/2$.

This means that there are some concave surfaces over which the displacement thickness rises with increasing distance.

The above relation for Δ^* can also be found by considering Lees expression for δ^*. In the scaled coordinate δ^* can be written as

$$\Delta^* = \frac{2\left[\int P d\xi\right]^{\frac{1}{2}}}{P} \qquad (4.2.2)$$

where

$$P = \frac{p_e}{p_\infty \gamma \alpha^2 M^2} \qquad (4.2.3)$$

For large ξ, pressure approaches the value of the wall, namely

$$P = (z_w z_w')' \qquad (4.2.4)$$

with $z_w = \xi^n$ we obtain

$$P = (2n^2-n)\xi^{2n-2} \qquad (4.2.5)$$

The equation (4.2.5) reveals that for a flat plate at incidence (n=1), pressure ratio approaches a constant value and for $n > 1$, i.e. compression surfaces, pressure increases with increasing distance. Putting equation (4.2.5) into equation

(4.2.2) we find

$$\Delta^* = k\,\xi^{3/2-n} \qquad (4.2.6)$$

where $k = \dfrac{2}{\sqrt{(2n^2-n)(2n-1)}}$

Equation (4.2.6) can be differentiated to give

$$\frac{d\Delta^*}{d\xi} = (\tfrac{3}{2} - n)k\xi^{\frac{1}{2}-n} \qquad (4.2.7)$$

This equation clearly demonstrates that for a family of concave surfaces $y_w = ax^n$ with $n > 1$, there are three distinctive behaviours of Δ^*. With increasing distance ξ, the displacement thickness increases for $1 < n < 3/2$, remains constant for $n = 3/2$ and decreases for $n > 3/2$. Therefore, for some concave surfaces of the form $y_w \sim x^n$, the displacement thickness rises with increasing pressure. In order to find an expression which relates pressure to the displacement thickness, we proceed as follows

$$\frac{d\Delta^*}{dP} = \frac{d\Delta^*}{d\xi} \cdot \frac{d\xi}{dP} \qquad (4.2.8)$$

With the equations (4.2.5) and (4.2.7) we obtain

$$\frac{d\Delta^*}{dP} = \frac{k(3/2-n)}{(2n^2-n)(2n-2)} \xi^{7/2-3n} \qquad (4.2.9)$$

A very important conclusion can be drawn from equation (4.2.9). This is that for some concave surfaces of the family of curve $y_w = ax^n$, the displacement thickness rises with increasing pressure. This phenomena disagrees with the usual assumption of the supercritical condition of hypersonic boundary layers. The condition of a boundary layer is said to be supercritical when $d\,\delta^*/dp_e < 0$, and subcritical when $d\,\delta^*/dp_e > 0$.

For $n < 3/2$ the boundary layer is subcritical and at $n = 3/2$ changes over to the supercritical condition. This phenomena is confirmed by the figures (27), (28) and (29), in which results of the numerical integration of both Cheng's and modified Cheng's methods for concave power law bodies are plotted.

4.3. A comparison between the theoretical results and experimental data for the cubic surface

The cubic model was tested at Mach numbers 8.2 and 12.25. At Mach 8.2 the boundary layer separated, therefore measurements were carried out only at $M = 12.25$. A comparison was also made with the data obtained by Fitzhugh (1968) at $M = 15.1$ using a conical nozzle. Typical schlieren pictures of the flow over the cubic model are shown in figures (13) and (14). These photographs show the boundary layer growth over the cubic surface. It can also be seen that the leading edge shock wave lies close to the body, so that the inviscid flow field is highly influenced by the presence of thick boundary layer, which occupies a considerable proportion of the space between the body and the shock wave.

4.3.1. Pressure distribution on the cubic surface

Pressure measurements at $M = 12.25$, in figure (17), clearly indicates that the flow field near the leading edge is very much affected by the displacement thickness. Therefore the inviscid theories can not be expected to predict the pressure distribution in these regions correctly. Figures (30) and (31) compare experimental data with theory at $M = 12.25$ and 15.1 respectively. There is a large discrepancy between the inviscid flow prediction, assuming Prandtl Meyer compression, and the measured data. The divergence between the inviscid theory and measurement increases with increasing boundary layer thickness. The Newtonian approximation underestimates the surface pressure at $M = 12.25$ and overestimates it at $M = 15.1$. If we take account for centrifugal force then we obtain the Newtonian and Busemann approximation, which compares favourably with the experimental results downstream at $M = 12.25$. Generally, near the leading edge, where $M^2\alpha^2/\bar{\chi}_\varepsilon \ll 1$, displacement effect dominates. Towards the rear of the surface, where $M^2\alpha^2/\bar{\chi}_\varepsilon \gg 1$, incidence effect will be more important. Therefore hypersonic approximation might be expected to adequately predict the measured surface pressure in regions, where $M^2\alpha^2/\bar{\chi}_\varepsilon \gg 1$. At $M = 12.25$ $M^2\alpha^2 = \bar{\chi}_\varepsilon$ at $x = 1.4''$, so that the dominating effect of viscous interaction is restricted to near the leading edge and the body slope dominates the flow over most of the surface. Hence the good agreement between Newton-Busemann and the experimental data at $M = 12.25$ shown in figure (30). At $M = 15.1$ the displacement effect dominates over most of the plate surface, and incidence effect grows in importance only after $x = 4''$. Hence the large discrepancies between data and theories shown in figure (31). It is noticeable that the measured pressure is still rising in the region where the plate has constant slope ($x > 5.1''$).

The above comparisons made it necessary to consider the viscous interaction as a first order effect, and so Cheng's equation was used for the cubic surface. The modification to Cheng's method suggested by Sullivan and extended by Stollery is also applied to the cubic model. Figure (32) and (33) contain comparisons between experimental data and the viscous interaction theories.

Cheng's theory predicts the pressure fairly well near the leading edge at $M = 12.25$, where the flow field is dominated by the displacement effect. The boundary layer grows in this region as though supported by a flat plate. Faced with adverse body slope it thins to a neck and starts oscillating. The oscillation occurs about

$$\frac{p_e}{p_\infty} = 15\gamma\alpha^2 M^2 \left(\frac{4\gamma\alpha^4 M^4}{A^2 \bar{\chi}^2}\right)^4 \quad .$$

If the more realistic tangent-wedge approximation is used then there is no oscillation, the boundary layer thickness decreasing steadily as the pressure rises.

The very good agreement between pressure measurement and the viscous interaction theory using the tangent-wedge approximation suggests that the choice of pressure law is very important in dealing with the joint effect of viscous interaction and incidence. It appears that the Busemann centrifugal correction is far too powerful in the Newton-Busemann pressure law.

4.3.2. Heat transfer distribution for the cubic surface

Heat transfer measurements were made at M = 12.25 . Figure (34) shows a comparison between measurements and three theories. These theories are

(i) Momentum integral method due to Luxton and Young.

(ii) Sell's method.

(iii) The 'flat plate' method for calculating the heat transfer rate, using the local inviscid values for the 'equivalent free stream'.

The results obtained when using Luxton and Young's method for the cubic surface, as shown in figure (34), are even worse than the local flat plate solution. Fitzhugh (1968) found that this method is fairly accurate under a Mach number of 4, especially for adiabatic wall cases and for cases where the wall heats the flow. But for cold wall cases, it becomes inaccurate with increasing Mach number above a Mach number of four.

Sell's method which is an exact method of solving the compressible boundary layer equations, is not much better than the local flat plate solution. Therefore we may conclude that the classical boundary layer theories do not adequately predict the heat transfer rate at high Mach numbers and strong pressure gradients without considering the viscous interaction effects.

The viscous interaction theories, (Cheng and modified Cheng) are compared with experimental data in figures (35) and (36). These figures show that Cheng's theory compares favourably with our measured heat transfer rate near the leading edge, but later greatly overestimates or under-estimates the heat transfer rates, because of the oscillatory behaviour of the solution.

When the more realistic tangent-wedge approximation is used, heat transfer prediction appears better. The solution does not oscillate and it certainly shows the right trend. But the method does not predict heat transfer rate adequately in the region of strong adverse pressure gradient, where the boundary layer profiles are markedly non similar.

It appears that the viscous interaction theories used in this work, which are the same except for the choice of the pressure law, are not adequate in predicting heat transfer rates for our type of problem, where we have strong adverse pressure gradients as well as strong viscous interaction. It is not too surprising that Lees' assumption of local flat plate similarity fails for cases with strong adverse pressure gradients.

4.3.3. Boundary layer growths on the cubic surface

The schlieren photographs presented in figures (13) and (14) give some indication of the boundary layer thickness at Mach numbers 12.25 and 15.1 for the cubic surface. The light line in the schlieren photograph appears because the schlieren system is sensitive to $\frac{\partial \rho}{\partial y}$ and, in the hypersonic boundary layers, the maximum density gradient occurs towards the outer edge. The outer edge of the dark line in the schlieren picture is very close to the outer edge of the boundary, such that it can be taken as a measure of the boundary layer thickness. Boundary layer pitot pressure profiles measured by Needham (1963) at a Mach number of $M = 9.7$ confirms the above argument. Values of boundary layer thickness were measured as explained above from the schlieren photographs at Mach numbers 12.25 and 15.1 and are presented in figures (37) and (38).

Sell's programme was used to calculate the boundary layer thickness at $M = 12.25$ and the result can be seen in figure (37). Sells over-estimates the displacement thickness δ^* near the leading edge and underestimates it further downstream, but shows the right trend.

The viscous interaction theories for boundary layer growth over the cubic surface are compared with the estimated boundary layer thickness from the schlieren pictures and are presented in figures (37), (38) and (39). The oscillation in displacement thickness predicted by Cheng's method using the Newton-Busemann pressure law, is clearly shown with the outer edge coming very close to the wall at the first "neck". The prediction using the tangent-wedge pressure law is more realistic with the layer lying close to the measurement over most of the surface and then thinning slowly but continuously in the downstream region.

4.4. Comparisons between the theoretical results and experimental data for the convex model

The convex surface downstream of an 18^{0} wedge was tested at Mach numbers of 8.2 and 12.25. The boundary layer remained attached and laminar as judged from the schlieren photographs and heat transfer records. Typical schlieren photographs are presented in figures (15) and (16). Even at the higher Mach number $M^2\alpha^2/\bar{\chi}_\varepsilon >> 1$ on the wedge and over much of the convex surface, so it was expected that conventional hypersonic approximations would adequately predict the pressure distribution. The Mach numbers behind the shock are theoretically 4.8 and 4.28 at freestream Mach numbers of 12.25 and 8.2 respectively. The viscous interaction parameter $\bar{\chi}_\varepsilon$ based on undisturbed flow at one inch is 1.06 and .197 at Mach numbers of 12.25 and 8.2 respectively.

4.4.1. Pressure distribution on the convex surface

Figures (40) and (41) show comparisons between measurements and various theories. Because of $M^2\alpha^2/\bar{\chi}_\varepsilon >> 1$, the pressure on the wedge is sensibly constant to within 0.3" of the leading edge. The incidence effect becomes of the same order as the viscous interaction effect, i.e. $M^2\alpha^2 \simeq \bar{\chi}_\varepsilon$, at a distance of 0.655" at $M = 12.25$. This distance reduces to 0.393" at $M = 8.2$. This suggests that the strong viscous interaction region must be confined to a region very close to the leading edge and elsewhere the flow field is strongly affected by the incidence. This is the reason for the good agreement between the tangent-wedge approximation (no viscous interaction) and the measurements.

Cheng's method does not give an oscillatory solution for convex surfaces in contrast to the concave ones. The boundary layer grows rapidly but smoothly in the helpful pressure gradient. The pressure prediction by Cheng for the convex surface is underestimated over the wedge but it is in a fairly good agreement at the rear part of the model. Although the modified Cheng's method overestimates the pressure on the flat parts of the model, it agrees fairly well on the expansion shoulder.

Stollery (1970) measured surface pressure of a flow past an expansion corner and applied both theories. The results are plotted in figure (42). Both theories give predictions which are in reasonable agreement with the experimental data. The modified Cheng's prediction is particularly good over the wedge surface ahead of the corner.

4.4.2. Heat transfer distribution for the convex surface

The two interaction theories, Cheng and the modified Cheng were used to predict the heat transfer rate on the convex surface. Figure (43) and (44) show comparisons between experimental data and the two theories. Both give predictions which are in reasonable agreement with the experimental data. The prediction of heat transfer by Cheng at $M = 8.2$ is in very good agreement with measurement over the wedge, but there is not a good agreement over the expansion shoulder. The reason for this is the rapid drop in pressure predicted over the first part of the expansion shoulder at $M = 8.2$.

On the whole the predictions made using

Cheng's and modified Cheng's methods seem to be reasonably good. Therefore, it appears that the assumption of local flat plate similarity is in fact reasonable in cases involving helpful pressure gradients.

In contrast to the concave cubic model we might expect to predict heat transfer rate on the convex model reasonably well when using compressible boundary layer approximate methods such as Luxton and Young and the local flat plate formula. Theoretical estimates were made starting from a uniform stream at $M = 4.8$ or 4.25, i.e. from appropriate local free stream conditions behind the oblique shock. Such comparisons are shown in figures (46) and (47). The good agreement between measurement and Luxton and Young's method suggests that heat transfer prediction by this method is quite adequate for cases involving expansion at lower hypersonic Mach numbers. Even the local flat plate solution which is the simplest method of calculating heat transfer rate seems to be in a good agreement with experimental data.

4.4.3. Boundary layer growth over the convex model

Schlieren photographs presented in figures (15) and (16) exhibit the boundary layer growth on the convex model. The boundary layer does not grow rapidly as it would on a flat plate with zero angle of attack, because of the strong incidence effect. Faced with the favourable pressure gradient around the shoulder the boundary layer thickens rapidly.

Figure (48) shows the displacement thickness δ^* calculated by the two viscous interaction theories, compared to the measurements. The method of measuring δ^* was outlined in a previous section. The predictions are fairly good on the front part of the model considering the errors involved in measuring δ^* from photograph. It appears that both methods although over-estimating the boundary layer growth over the expansion region, demonstrate the correct trend.

5. CONCLUSIONS

The strong viscous interaction method due to Cheng et al is extended to cover curved surfaces. It is shown numerically and analytically that the resulting scaled equation has an oscillatory behaviour when applied to concave power law bodies. The oscillation begins in the region where the dominant effect turns from displacement to incidence, i.e. $M^2\alpha^2 > \bar{\chi}_\varepsilon$.

The results obtained, by applying Cheng's method to the cubic concave surface, are compared with the experimental data at $M = 12.25$ and 15.1. It is shown that the surface pressure and the heat transfer rate are predicted very well in the region of strong viscous interaction where the adverse pressure is weak. Further downstream, where Cheng's equation oscillates the comparison does not hold. It appears that the centrifugal correction in the assumed Newton-Busemann pressure law is too powerful. It is demonstrated that the solution does not oscillate if other pressure laws are used (i.e. modified Cheng).

Good agreement is obtained when comparing pressure measurements to the cubic surface with the modified Cheng's method. Agreement between heat transfer measurements and this theory is somewhat less satisfactory in the regions of strong pressure gradients where the boundary layer profiles are markedly non-similar.

Although in the case of convex surfaces Cheng's viscous interaction theory in its original and modified versions may be used to predict surface pressure and heat transfer rate, the modified Cheng is preferable because it covers both strong and weak interaction, whereas the original form is strictly for strong viscous interaction regions. In cases of adverse pressure gradients Cheng's original form oscillates and therefore is not realistic.

It is demonstrated that approximate methods such as Luxton and Young's method can predict heat transfer on convex surfaces where the effect of viscous interaction is negligible and $M^2\alpha^2 >> \bar{\chi}_\epsilon$. These methods prove fruitless at high Mach numbers for concave surfaces where the flow field is dominated by strong viscous interaction and strong adverse pressure gradients.

At high speed, the first order finite-difference computer programme of Sells does not give satisfactory results in the case of concave surfaces. Good predictions may be obtained if the viscous interaction is incorporated in this method. Nevertheless, it can provide useful information such as effect of Mach number, Prandtl number and wall temperature on separation point position.

REFERENCES

Ames staff	1953	Equations, tables and charts for compressible flow. NACA Report 1135.
Blasius, H.	1908	Zeitschrift für angewandte Math. Phys. 56, 1.
Cheng et al	1960	Boundary-Layer Displacement and Leading-Edge Bluntness Effects in High-Temperature Hypersonic Flow. Journal of the Aerospace Sciences.
Cohen, C.B. and Reshotko, E.	1956a	Similar solutions for the compressible laminar boundary layer with heat transfer and pressure gradient. NACA Rep. 1293.
Cohen, C.B. and Reshotko, E.	1956b	The compressible laminar boundary layer with heat transfer and arbitrary pressure gradient. NACA Rep. 1294.
Cox, R.N. and Crabtree, L.F.	1965	Elements of Hypersonic Aerodynamics. The English Universities Press Ltd.

Fitzhugh, H.A. 1968 A Study of Longitudinal Curvature Effects on the Hypersonic Laminar Boundary Layer. Ph.D. Thesis Imperial College.

Hall, I.M. 1961 Transonic flow in 2D and axially-symmetric nozzles. A.R.C. 23,347 (1961)

Hammitt, A.G. and Bogdonoff, S.M. 1955 Leading Edge Effects on the Flow over a Flat Plate at Hypersonic Speeds. Princeton Aeronautical Engineering Report No. 326.

Hayes, W.D. 1947 " On Hypersonic Similitude ". Quat. Appl. Math. 5, 105-106.

Hayes, W.D. and Probstein, R.F. 1959a Hypersonic Flow Theory, Academic Press, New York and London.

Holden, M.S. 1964 Heat Transfer in Separated Flow. Ph.D. Thesis Imperial College.

Hunter, J.A. 1968 Theory and Operation of the Equipment used at Imperial College to measure Heat Transfer rate in Hypersonic Flow.

Kepler, C.E. and O'Brien, R.L.	1962	Supersonic Turbulent Boundary Layer Growth over Cooled Walls in Adverse Pressure Gradients. ASD-TDR-62-87, Oct. 1962.
Lees, L.	1953	On the Boundary Layer Equations in Hypersonic Flow and their Approximate Solutions. J. Aero. Sci 20 PP. 143-145.
Lees, L.	1956	Inviscid Hypersonic Flow over blunt nosed slender bodies. GALCIT Hypersonic Research Project. Memo No. 31.
Luxton, R.E.	1967	The Calculation of Heat Transfer Coefficients from Skin Friction Coefficient in the Compressible Laminar Boundary Layer on an Aerofoil. The Aeronautical Quarterly.
Luxton, R.E. and Young A.D.	1962	Generalized Methods for the Calculation of the Laminar Compressible Boundary Layer Characteristics with Heat Transfer and Nonuniform Pressure Distribution. ARC R M 3233, 1962.

McLafferty, G. and Barber, R.E.	1959	Turbulent Boundary Layer Characteristics in Supersonic Streams having Adverse Pressure Gradient. United Aircraft Co., Rept. R-1285-11, Sept. 1959.
Monaghan, R.J.	1960	Effects of Heat Transfer on Laminar Boundary Layer Development under Pressure Gradients in Compressible Flow. Royal Aircraft Establishment, Report No. Aero 2640.
Myring, D.F. and Young, A.D.	1968	The Isobars in Boundary Layers at Supersonic Speeds, Aero. Quarterly 19, Pt. 2, May 1968, P.105.
Needham, D.A.	1963	Progress Report on the Imperial College Gun Tunnel, ICST Aero. Dept. Rept. 118, August 1963.
Opatowski, T.P.S.	1967	"Calibration of Mach 8 contoured nozzle". Imperial College Aeronautics, Internal Memo.
Prandtl, L.	1904	Über flüssigkeits-bewegung bei sehr kleiner Reihung. Proceedings of the 3rd Mathematical Congress, Heidelbarg 1904.

Schlichting, H.	1968	Boundary Layer Theory. McGraw-Hill Company.
Sells, C.C.L.	1966	Two-Dimensional Laminar Compressible Boundary Layer Programme for a Perfect Gas. A.R.C.R. and M. No. 3533.
Shen, S.F.	1952	On the Boundary-Layer Equations in Hypersonic Flow, Reader's Forum, Journal of the Aeronautical Sciences Vol.19, No.7, P.500, July 1952.
Stewartson, K.	1955	On the Motion of a Flat Plate at High Speed in a Viscous Compressible Fluid - Pt.II, Steady Motion, Journal of the Aeronautical Science, Vol.22, No.5, P.303, May 1955.
Stollery et at	1960	"The Imperial College Gun Tunnel", Journal of the Royal Aeronautical Society Vol.64, P.24.
Stollery, J.L.	1970	Hypersonic Viscous Interaction on Curved Surfaces. (To be published).

Stratford, B.S. and Beavers, G.S.	1961	The Calculation of the Compressible Turbulent Boundary Layer in an Arbitrary Pressure Gradient-A Correlation of certain previous Methods. R. M. No.3207.
Sullivan, P.A.	1963	An Investigation of Hypersonic Flow over Concave Surfaces and Corners. London U. Ph.D. Thesis, 1963.
Sullivan, P.A.	1968	On the Interaction of a Laminar Hypersonic Boundary Layer and A Corner Expansion Wave. UTIAS Technical Note, No.129.
Van Driest, E.R.	1952	Investigation of Laminar Boundary Layer in Compressible Fluids Using the Crocco Method. NACA TN 2597.
Van Dyke, M.D.	1954	A Study of Hypersonic Small-Disturbance theory. NACA Rep. 1194.
Young, A.D.	1949	Skin Friction in the Laminar Boundary Layer in Compressible Flow. Aero. Quarterly, Vol.1 PP.137 to 164, Aug. 1949.

APPENDIX

Asymptotic solution of the Cheng equation for a family of shape $z_w = \xi^n$ for $z \longrightarrow 0$.

The Cheng's equation may be written as

$$(z-\xi^n)(\sqrt{zz'})' = 1 \qquad (1)$$

The above equation reveals a singular behaviour at the origin. With $\xi = 0$, equation (1) admits the solution $z \sim \xi^{3/4}$ which is the flat plate solution. With the asymptotic solution for $\xi \longrightarrow 0$, solution to the equation (1) may be obtained by a forward integration from the origin.

We first introduce new variables of order one, F and η .

$$\xi = \quad \eta \qquad (2)$$

$$z = \quad F \qquad (3)$$

ε and δ are control parameters and we expect δ to be a function of ε . Now equation (1) may be rewritten in terms of new variables F and η .

$$\left(F - \frac{\varepsilon^n}{\delta}\eta^n\right)\frac{\delta^2}{\varepsilon^{3/2}}\left(\sqrt{FF'}\right)' = 1 \qquad (4)$$

In order to have just one parameter in the equation (4) we put

$$\frac{\varepsilon^n}{\delta} = \frac{\delta^2}{\varepsilon^{3/2}} \qquad (5)$$

Solving equation (5) for we obtain

$$\delta = \varepsilon^{\frac{n}{3}+1/2} \qquad (6)$$

Thus

$$\left(F - \delta^{2/3n-1/2}\eta^n\right)\left(\sqrt{FF'}\right)' = \lambda \qquad (7)$$

where

$$\lambda = \frac{1}{\delta^{2/3n-1/2}} \qquad (8)$$

where ( )' denotes differentiation with respect to η .

The expansion can now be written in the following form

$$F = F_0(\eta) + \varepsilon^{2/3n-1/2}F_1(\eta) + O[\varepsilon^{4/3n-1}] \qquad (9)$$

We keep only the first two terms for F and neglect terms of the order of $\varepsilon^{4/3^{n-1}}$. The result has to be examined for this negligence.

We now replace F of equation by the series found in (9), make use of binomial theorem and neglect terms of the order of $\varepsilon^{4/3^{n-1}}$. The resulting expression would then be

$$F_o(\sqrt{F_oF_o'})' + \varepsilon^{2/3^{n-1}/2}\left[F_o\left(\frac{F_oF_1'+F_o'F_1}{2\sqrt{F_oF_o'}}\right)' + (F_1-\eta^n)(\sqrt{F_oF_o'})'\right] = \lambda \tag{10}$$

Equation (10) may now be split into order-one and order-zero equations

$$F_o(\sqrt{F_oF_o'})' = \lambda \tag{11}$$

$$F_o\left(\frac{F_oF_1'+F_o'F_1}{2\sqrt{F_oF_o'}}\right)' + (F_1-\eta^n)(\sqrt{F_oF_o'})' = 0 \tag{12}$$

Equations (11) and (12) may now be solved as follows.

The solution for equation (11) is

$$F_o = \sqrt{\frac{8}{3^{\frac{1}{2}}}\lambda} \quad \eta^{3/4} \tag{13}$$

This equation is the leading term in the expansion which we expected. Making now use of the solution found for F_0 in (13), equation (12) may be rewritten as

$$F_1'' + \frac{5}{4}\eta^{-1} F_1' - \frac{3}{8}\eta^{n-2} = 0 \qquad (14)$$

This equation permits the solution

$$F_1 = \frac{3}{8n^2 + 2n}\,\eta^n \qquad (15)$$

Transforming back into z-ξ coordinates we may write

$$z = \frac{2\sqrt{2}}{3^{1/4}}\,\xi^{3/4} + \frac{3}{8n^2 + 2n}\,\xi^n + \ldots \qquad (16)$$

where n can be any number greater than one. A discussion of equation (16) can be found in Chapter 3 of this thesis.

Table 1

Pressure measurements in psia on cubic model at $M = 12.25$ and $Re/'' = .86 \times 10^5$, $T_o = 1300^\circ k$

$P_o = 1600$ psia, x in inches

x =	.5	.8	1.1	1.4	1.7	2.0	2.3
p =	.0165	.0165	.0155	.0170	.018	.0248	.033
	.0180					.0250	

x =	2.6	3.125	3.25	3.375	3.5	3.625	3.75
p =	.042	.098	.148	.130	.192	.190	.245
		.079	.137	.135	.175		

x =	3.875	4.0	4.125	4.25	4.375	4.5	4.625
p =	.255	.303	.358	.385	.455	.535	.555
		.296				.520	.547

x =	4.75	4.875	5.0	5.125	5.25	5.375	5.5
p =	.636	.638	.641	.633	.650	.590	.566
	.626				.645		

x =	5.625	5.75	5.875
p =	.583	.538	.510
	.557	.490	.504

Table 2

Measured heat transfer rate in BTU/ft²/sec

on centre line of cubic model at $M = 12.25$

$Re/'' = .86 \times 10^5$ and $T_o = 1300^o k$; $P_o = 1600$ psia,

x in inches

x =	1.0	1.25	1.5	1.75	2.0	2.25	2.50	2.75
$\dot{q}$ =	1.51	1.39	1.21	1.200	1.31	1.32	1.64	1.97
	1.50	1.25	1.20	1.110	1.24	1.15	1.49	1.82
	1.42			1.05	1.16			

x =	3.0	3.5	3.75	4.0	4.25	4.5	4.75	5.0
$\dot{q}$ =	2.29	2.85	3.78	5.12	7.85	8.15	11.71	14.86
	2.15	2.60	3.49	5.09	7.47	9.20	12.34	13.06
	2.12			5.0		9.61	13.17	12.5

Table 3

Spanwise heat transfer measurements in BTU/ft^2/sec on cubic model at $M = 12.25$; $T_o = 1300^o k$

1 inch from the leading edge

$y =$	1.5	.75	0.0	.75	1.5
$\dot{q} =$	1.37	1.51	1.51	1.40	1.52
			1.50		
			1.42		

3 inches from the leading edges

$\dot{q} =$	2.20	2.0	2.29	2.08	2.29
			2.15		
			2.12		

5 inches from the leading edges

$\dot{q} =$	12.0	12.0	14.86	15.3	14.1
	12.6	14.0	13.06	14.8	
			12.0		

<u>Table 4</u>

Pressure measurements in psia on the centre line of convex model at $M = 12.25$, $P_o = 1600$ psia, $T_o = 1300^o k$, x in inches

x =	.3	.6	.9	1.2	1.5	1.8	2.1
p =	.250	.255	.253	.250	.262	.251	.250
	.255	.250		.268	.263	.268	.253
	.259	.242					.245

x =	2.4	2.7	3.0	3.3	3.6	3.9	4.2
p =	.249	.251	.255	.263	.224	.200	.165
	.252	.264	.251	.262	.218	.189	
				.242			

x =	4.5	4.8	5.1	5.4	5.7	6.0	6.3
p =	.151	.100	.075	.062	.045	.032	.025
	.120	.105					
	.123	.110					

x =	6.6	6.9	7.2	7.5	7.8	8.1	8.4	8.7	9.0
p =	.023	.017	.014	.016	.013	.015	.015	.016	.015
				.013					

Table 5

Pressure measurements in psia on the centre line of convex model at $M = 8.2$, $P_o = 1600$ psia, $T_o = 1300^{o}k$, x inches

x =	.3	.6	.9	1.2	1.5	1.8	2.1
p =	1.651	1.633	1.600	1.837	1.78	1.837	1.742
	1.522	1.570	1.420	1.540	1.59	1.71	1.731
							1.720

x =	2.4	2.7	3.0	3.3	3.6	3.9	4.2
p =	1.865	1.80	1.76	1.725	1.56	1.40	1.20
	1.803	1.585	1.66	1.70			
	1.687						

x =	4.5	4.8	5.1	5.4	5.7	6.0	6.3
p =	.897	.68	.537	.481	.378	.33	.242

x =	6.6	6.9	7.2	7.5	7.8	8.1	8.4	8.7
p =	.21	.18	.172	.172	.174	.170	.174	.173

Table 6

Measured heat transfer rate in BTU/ft^2/sec on centre line of convex model at $M = 12.2$, $P_o = 1600$ psia, $T_o = 1300^\circ$k, x in inches

$x =$	1.0	1.25	1.5	1.75	2.0	2.25	2.50
$\dot{q} =$	6.41	5.23	4.57	4.40	4.03	3.83	3.49
	6.13	5.19	4.38	4.21	3.92	3.71	3.25
	6.09	5.00	4.31	4.05	3.83	3.60	
	6.03	4.35			3.61	3.40	
	5.59				3.55		

$x =$	2.75	3.0	3.25	3.50	4.25	4.50	4.75
$\dot{q} =$	4.20	3.11	4.02	2.71	2.53	2.10	1.79
	3.70	3.03	3.97	2.69	2.51	2.04	1.70
	3.61	2.92	3.55	2.64	2.47	2.00	1.63
		2.83			2.30		

$x =$	5.0	5.25	5.5	6.0	6.5	7.0	7.5	8.0
$\dot{q} =$	1.60	1.30	1.00	.80	.57	.56	.41	.45
	1.50	1.00	.93	.68	.53	.50		.42
	1.48			.60				.40
	1.43							

$x =$	8.5	9.0
$\dot{q} =$	.40	.39
		.37

<u>Table 7</u>

Measured heat transfer rate in BTU/ft^2/sec on the centre line of the convex model at $M = 8.2$, $P_o = 1600$ psia, $T_o = 1300^o$k, x in inches

$x =$	1.0	1.25	1.50	1.75	2.0	2.25	2.5
$\dot{q} =$	14.98	10.95	9.72	8.60	7.82	7.40	6.69
	13.78	10.47	9.60	8.28	7.61	7.05	6.52
	12.60		9.42		7.40	6.20	6.10
						6.00	

$x =$	2.75	3.0	3.25	3.5	4.25	4.5	4.75
$\dot{q} =$	8.98	6.48	8.40	6.20	5.19	4.03	4.07
	8.20	6.01	8.21	5.78	5.11	3.90	3.75
		5.91			4.98		
	7.30	5.65	7.42	5.52	4.20	3.68	3.51

$x =$	5.0	5.25	5.5	5.75	6.0	6.5	6.75
$\dot{q} =$	3.40	2.38	2.50	2.0	1.88	1.36	1.18
	3.11	2.21	2.27		1.72		
	2.90		2.20				

$x =$	7.0	7.5	8.0	8.5	9.0
$\dot{q} =$	1.15	1.00	1.02	.91	.80
	1.08		.90		.86

Table 8

Measured heat transfer made in BTU/ft²/sec on the centre line of the convex model at $M = 12.2$, $P_o = 800$ psia, $T_o = 1037^{o}k$, x in inches

$x =$	1.0	1.5	2.0	3.0
$\dot{q} =$	4.40	2.57	2.15	1.46
	3.73	2.56	1.90	1.45
	3.69	2.49	1.81	1.39
	3.61			

Table 9

Measured heat transfer rate in BTU/ft²/sec on the centre line of the convex model at $M = 8.2$, $P_o = 1200$ psia, $T_o = 1185^{o}k$, x in inches

$x =$	1.0	1.5	2.0	3.0	3.5	4.5	5.0
$\dot{q} =$	11.0	7.35	6.13	5.02	4.28	3.27	2.54
	10.65	7.01	5.69	4.84		3.00	3.34
	9.81		5.40				

$x =$	5.5	6.0	6.5	7.0	7.5	8.25
$\dot{q} =$	1.90	1.49	1.08	1.00	.89	.80
	1.75	1.30				

Table 10

Spanwise heat transfer measurements in BTU/ft^{2}sec on convex model at M = 12.25, P_o = 1600 psia, T_o = 1300^{o}k, y in inches

2 inches from the leading edge

y =	1.5	.75	0.0	.75	1.5
q =	4.18	4.01	4.03	3.78	3.97
	3.91	3.69	4.92	3.60	3.95
		3.41	3.83		3.80
			3.81		
		3.40	3.55		

5 inches from the leading edge

y =	1.5	.75	0.0	.75	1.5
q =		1.51	1.60	1.53	1.45
		1.43	1.50	1.33	1.34
		1.33	1.48	1.24	
			1.43		

8 inches from the leading edge

y =	1.5	.75	0.0	.75	1.5
q =	.42	.44	.45	.40	.39
	.38	.41	.42	.40	.37
			.40	.38	

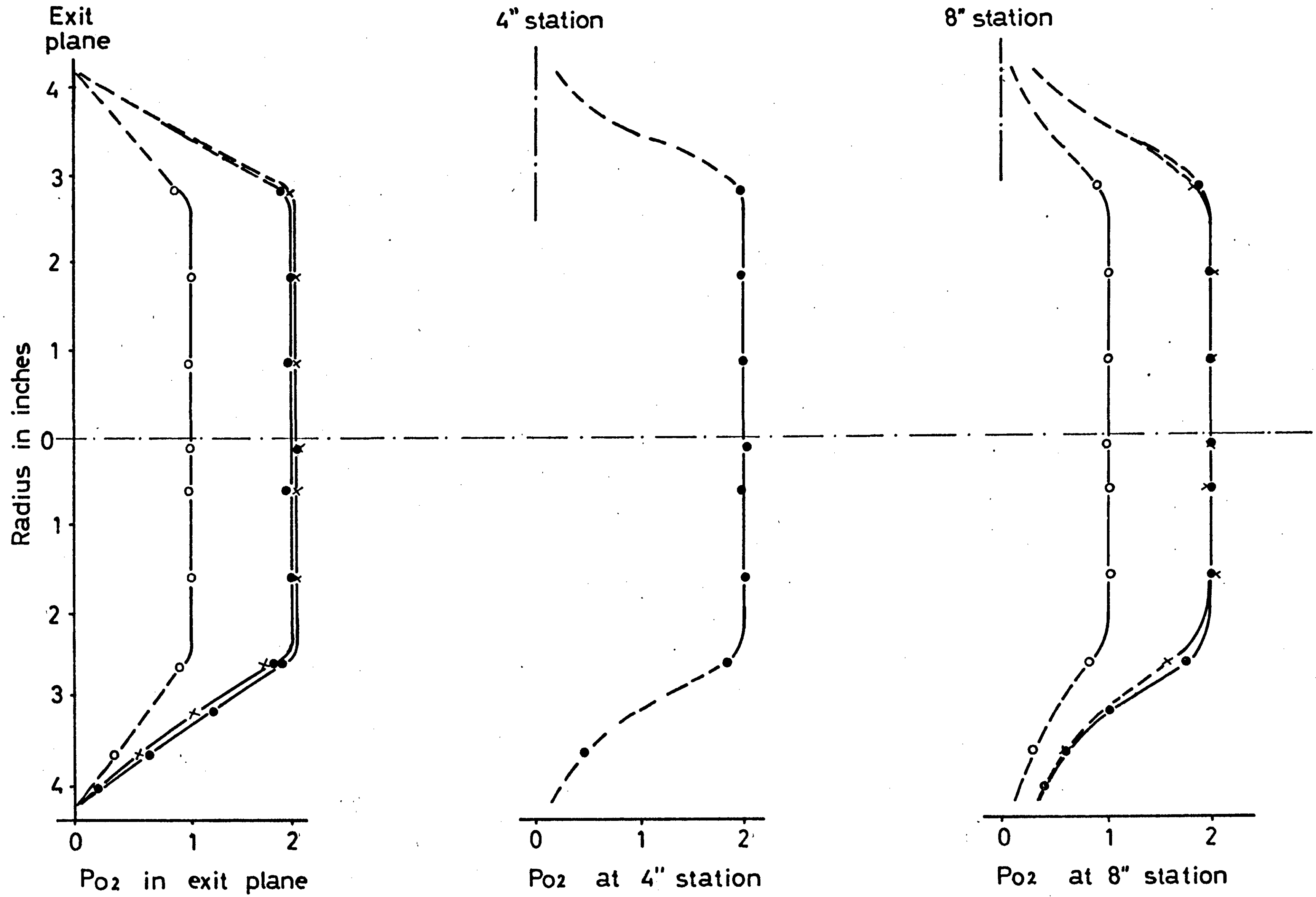

FIG. 1 Pitot Pressure Distribution

P_4 = 2000 psig; P_1 = 14·7 psia ——●——
P_4 = 2000 psig; P_1 = 25·0 psia ——x——
P_4 = 1000 psig; P_1 = 14·7 psia ——o——

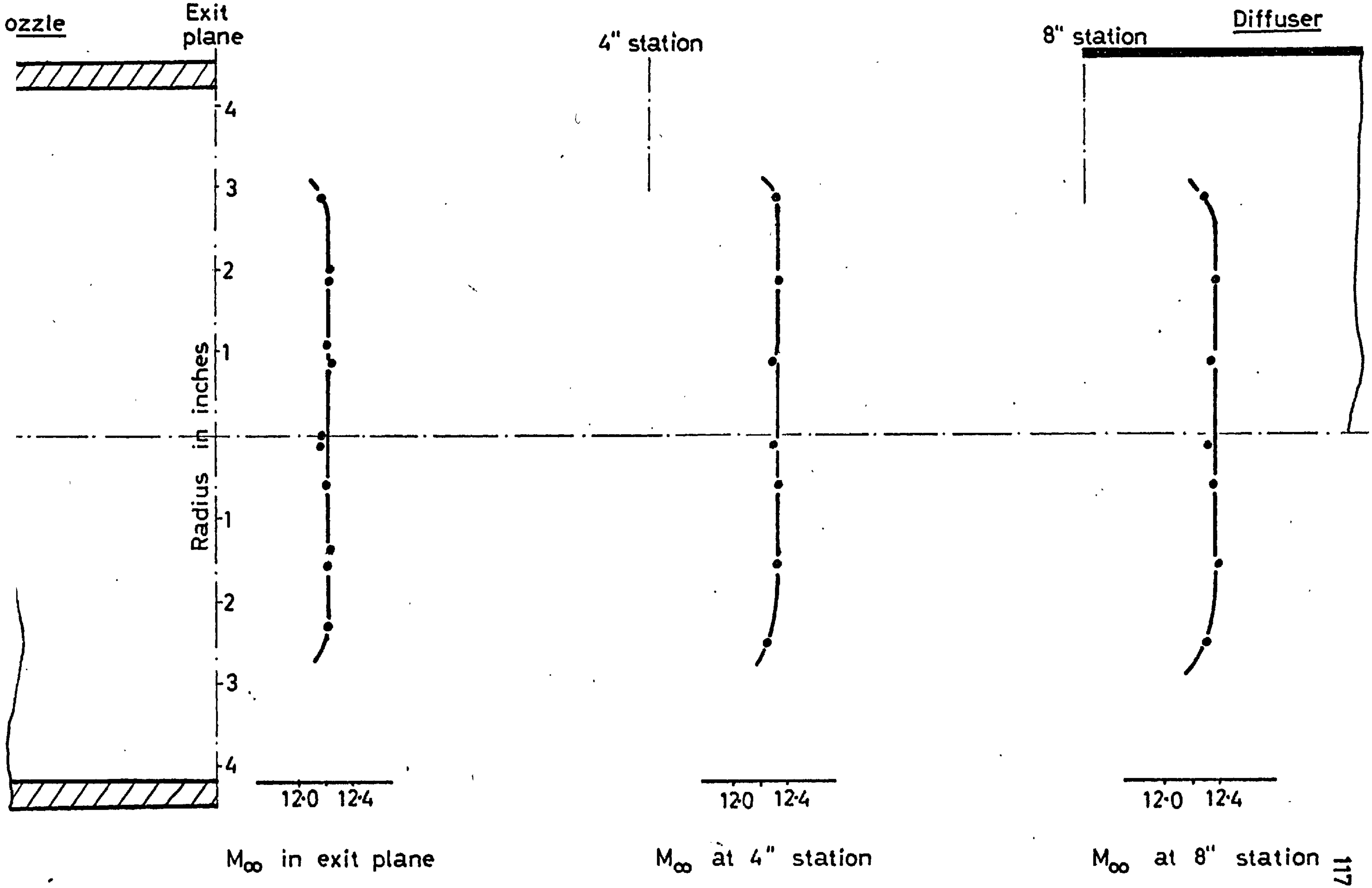

FIG. 2 Mach Number Distribution in test jet

P = 2000 si · P =14·7 sia

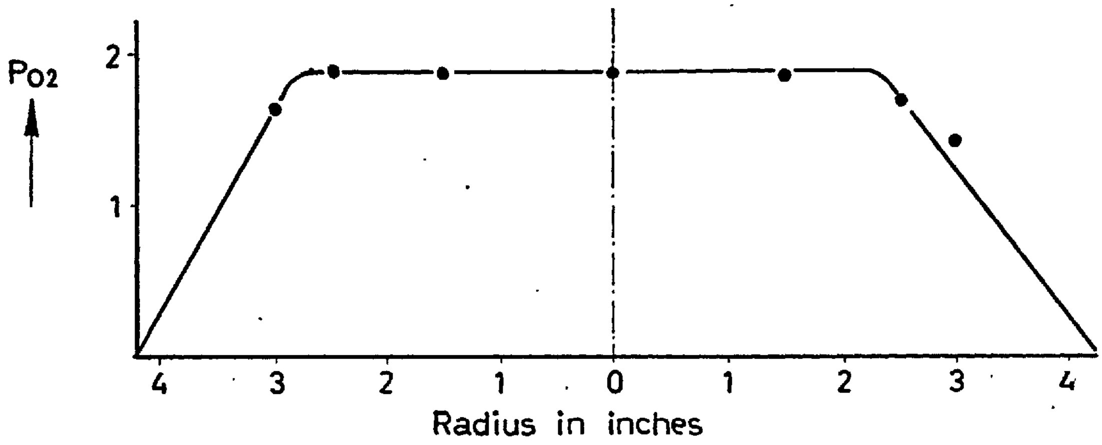

FIG. 3 Pitot Pressure Distribution across the horizontal radius of the nozzle exit plane.

P_4 = 2000 psig; P_1 = 14·7 psia

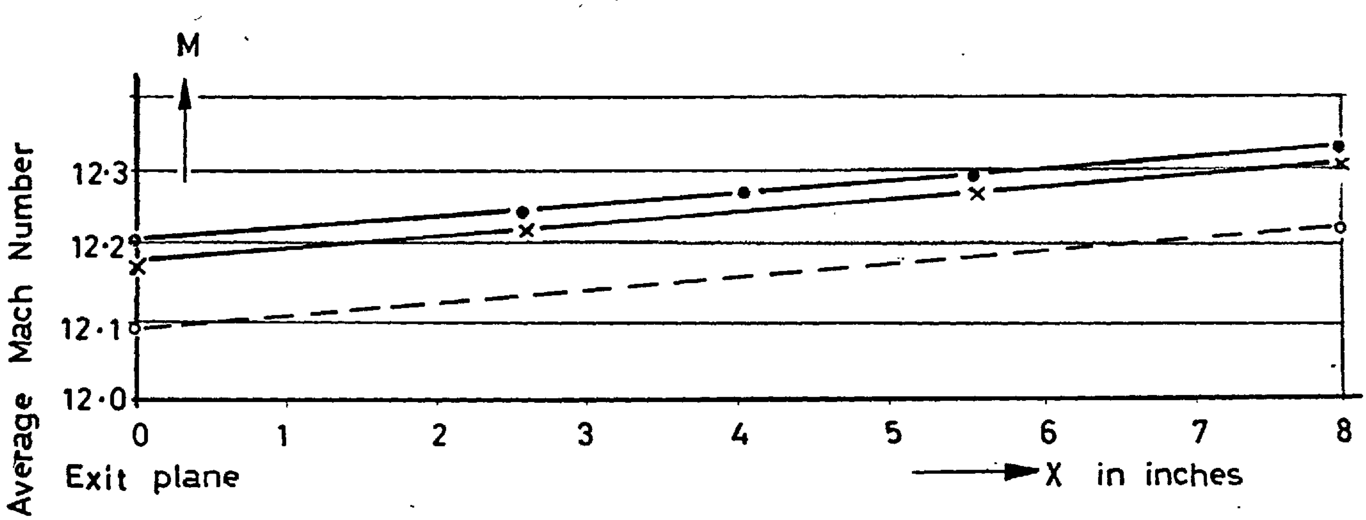

FIG. 4 Mach Number Distribution in the test section.

P_4 = 2000 psig; P_1 = 14·7 psia ——●——

P_4 = 2000 psig; P_1 = 25·0 psia ——x——

P_4 = 1000 psig; P_1 = 14·7 psia ——o——

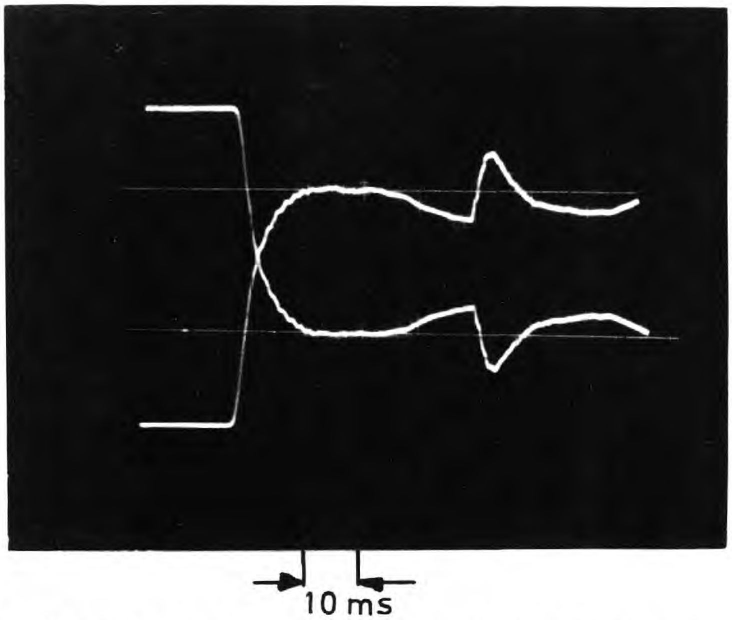

Fig.(5) Oscilloscope trace of pressure transducer output

Fig.(6) Schlieren photograph of flow with a wedge model in the testsection

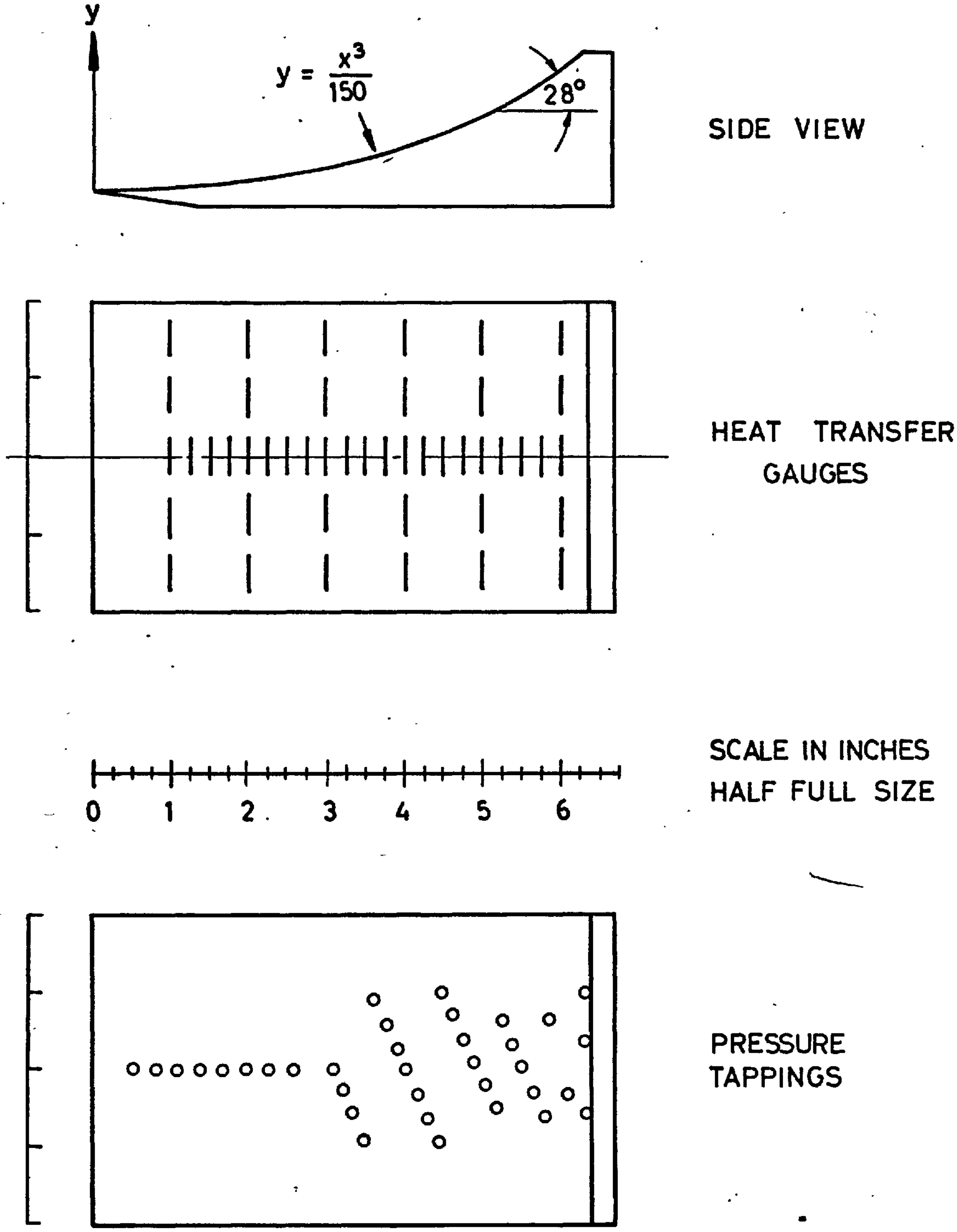

FIG. 7 LAYOUT OF THE CUBIC MODEL

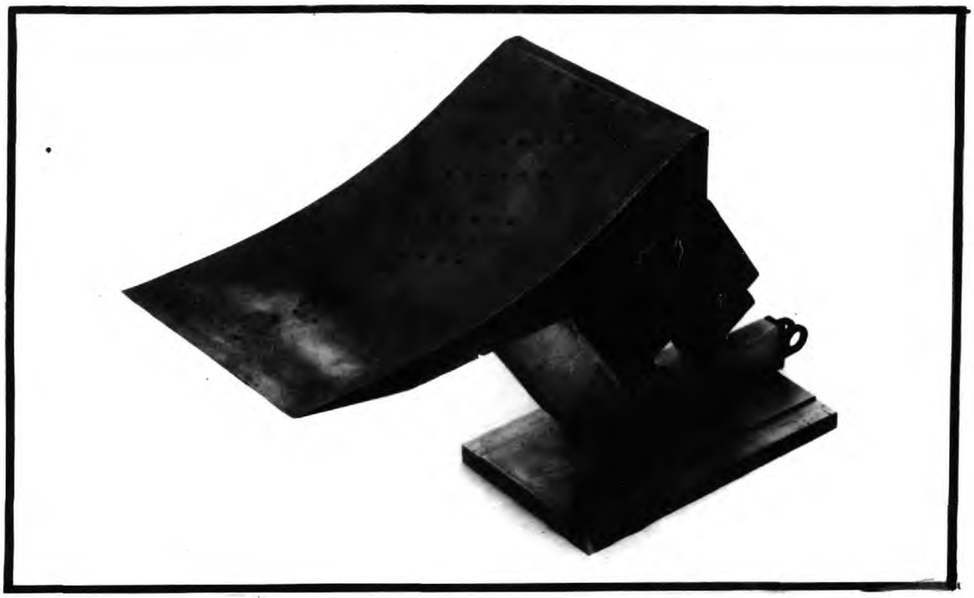

a) pressure model

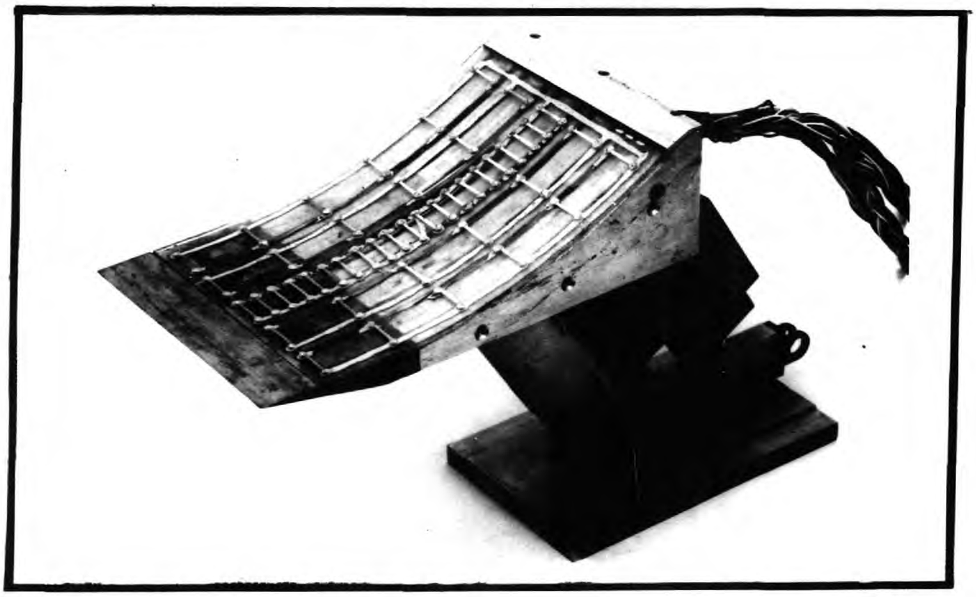

b) heat transfer model

Fig.(8) Concave model

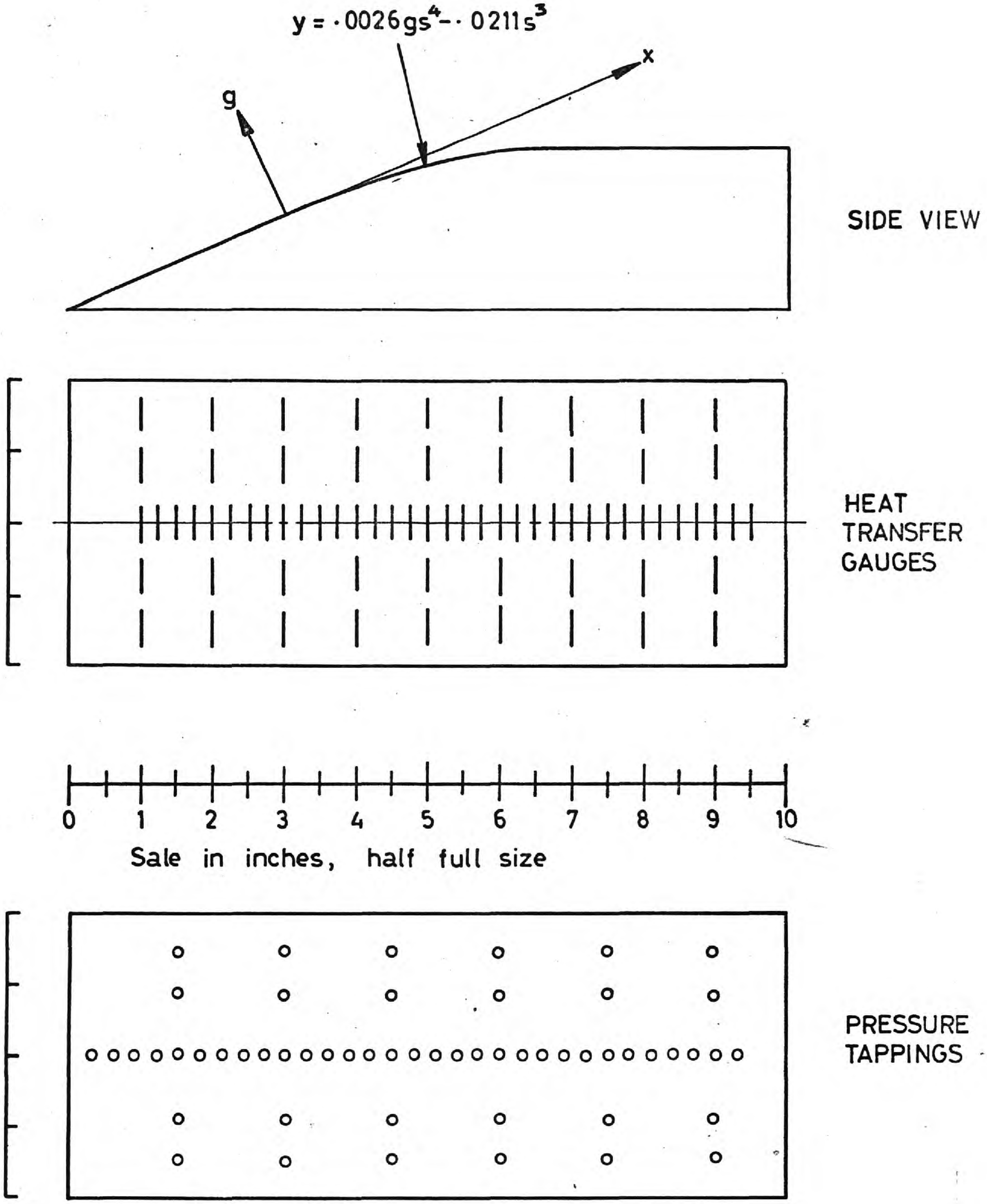

FIG. 9 LAYOUT OF THE CONVEX MODEL

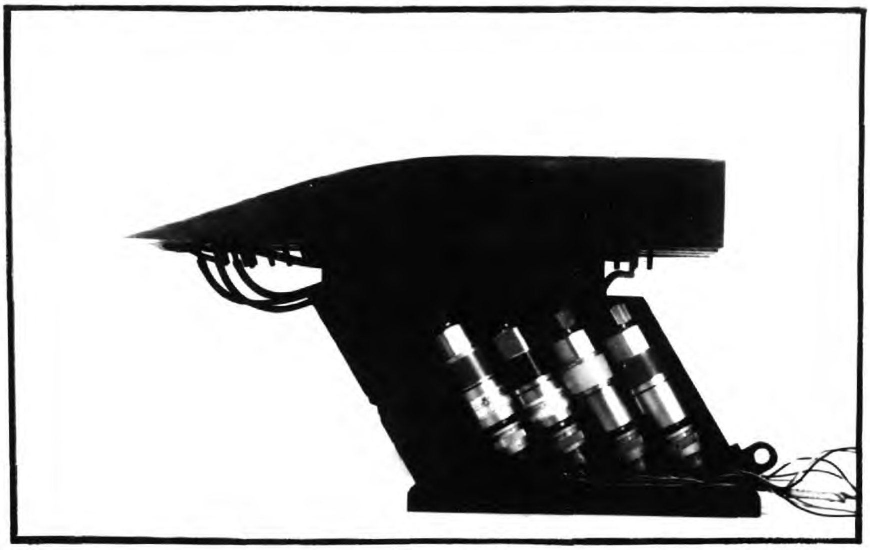

Fig.(10) The sting mounting of the pressure transducers

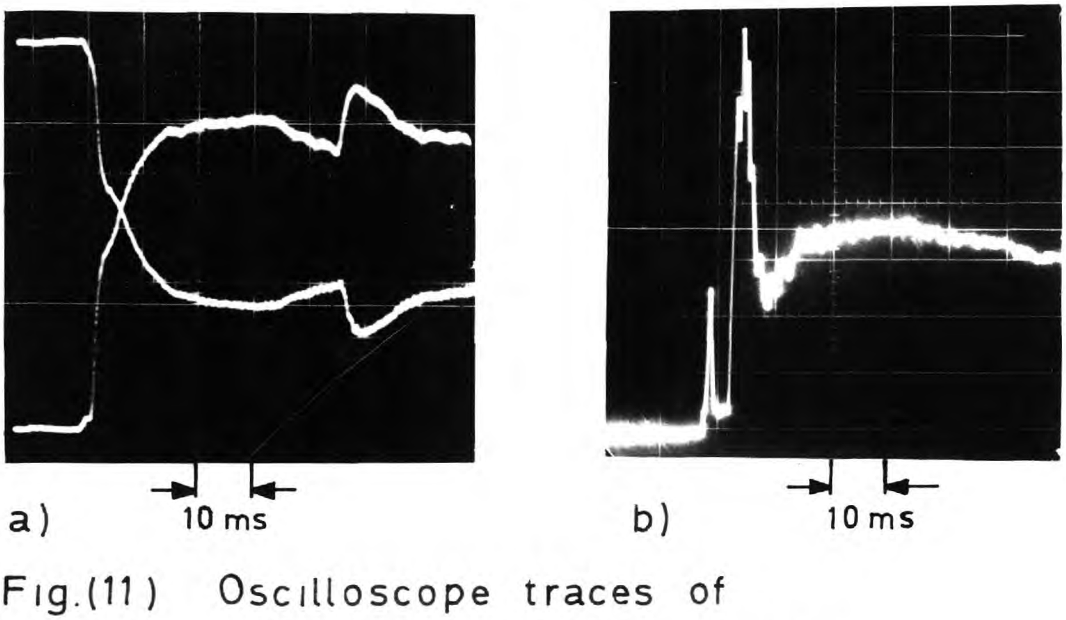

Fig.(11) Oscilloscope traces of

a) pressure transducer output

b) heat transfer output

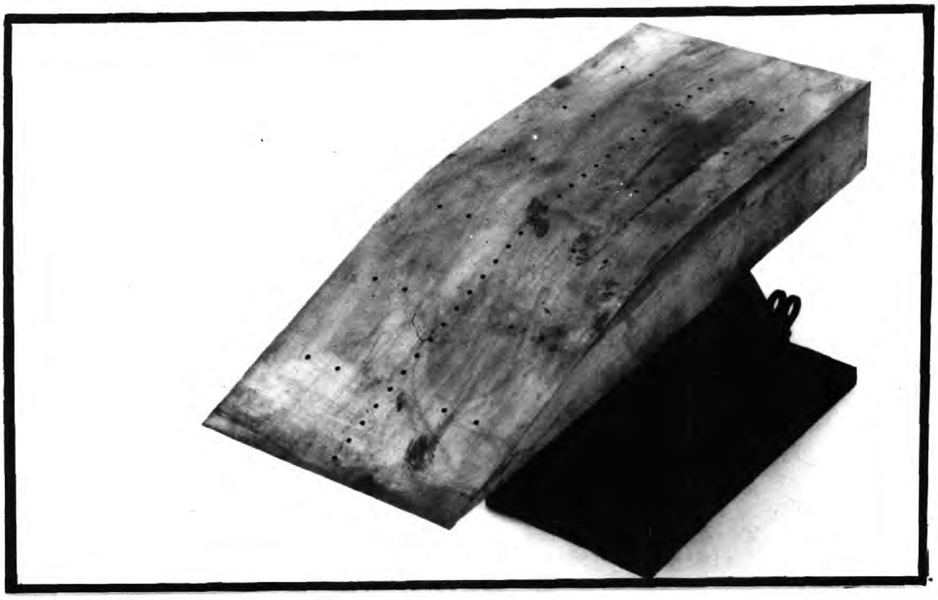

pressure model

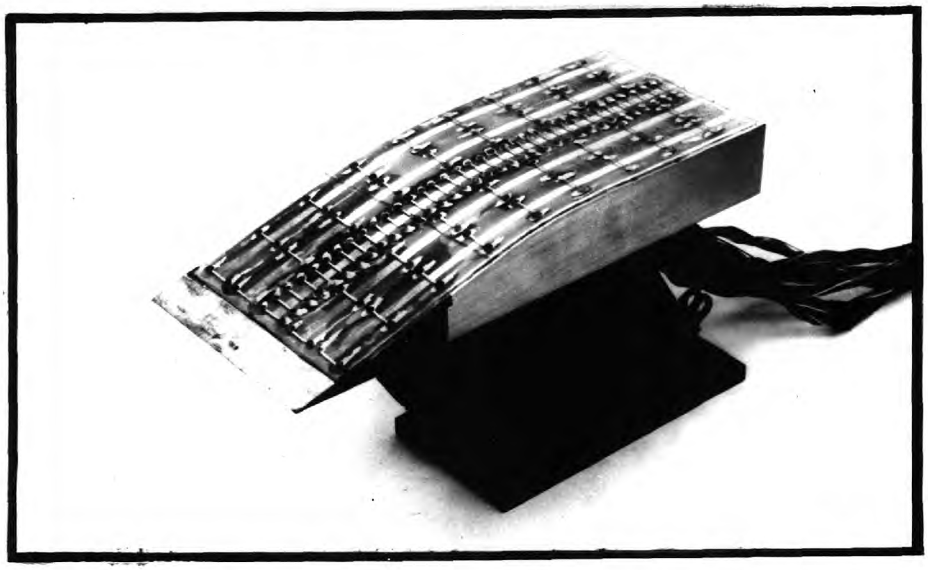

heat transfer model

Fig.(12) Convex model

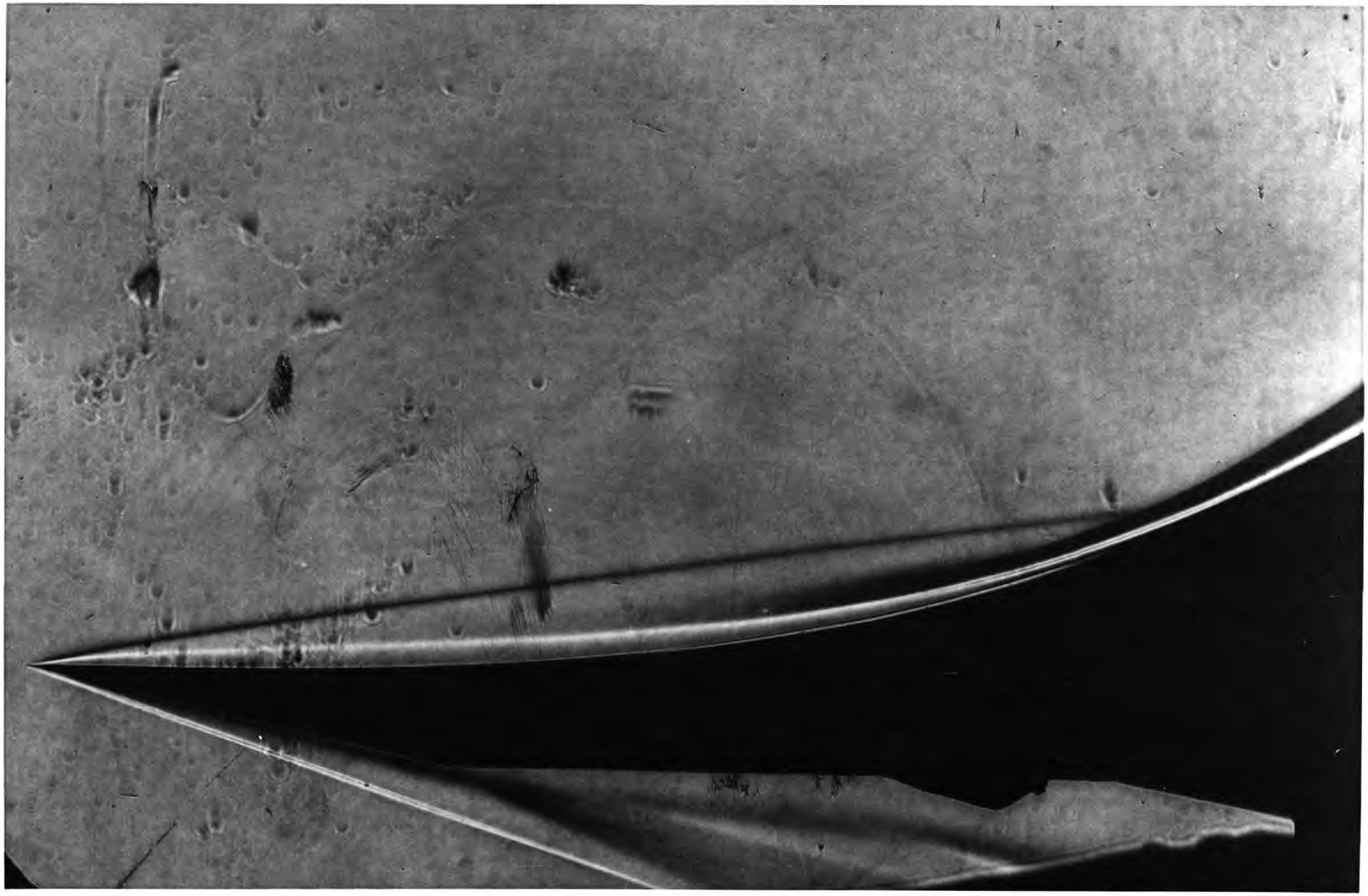

Fig. (13) Schlieren photograph of flow over cubic surface.
$M = 12.25$, $Re/'' = 0.86 \times 10^5$

Fig. (14) Schlieren photograph of flow over cubic surface.

$M = 15.1$, $Re/'' = 0.52 \times 10^5$

Fig. (15) Schlieren photograph of flow over the front part of the convex surface.
$M = 12.25$, $Re/'' = 0.86 \times 10^5$

Fig. (16) Schlieren photograph of flow over the rear part of the convex surface.
$M = 12.25$, $Re/'' = 0.86 \times 10^5$

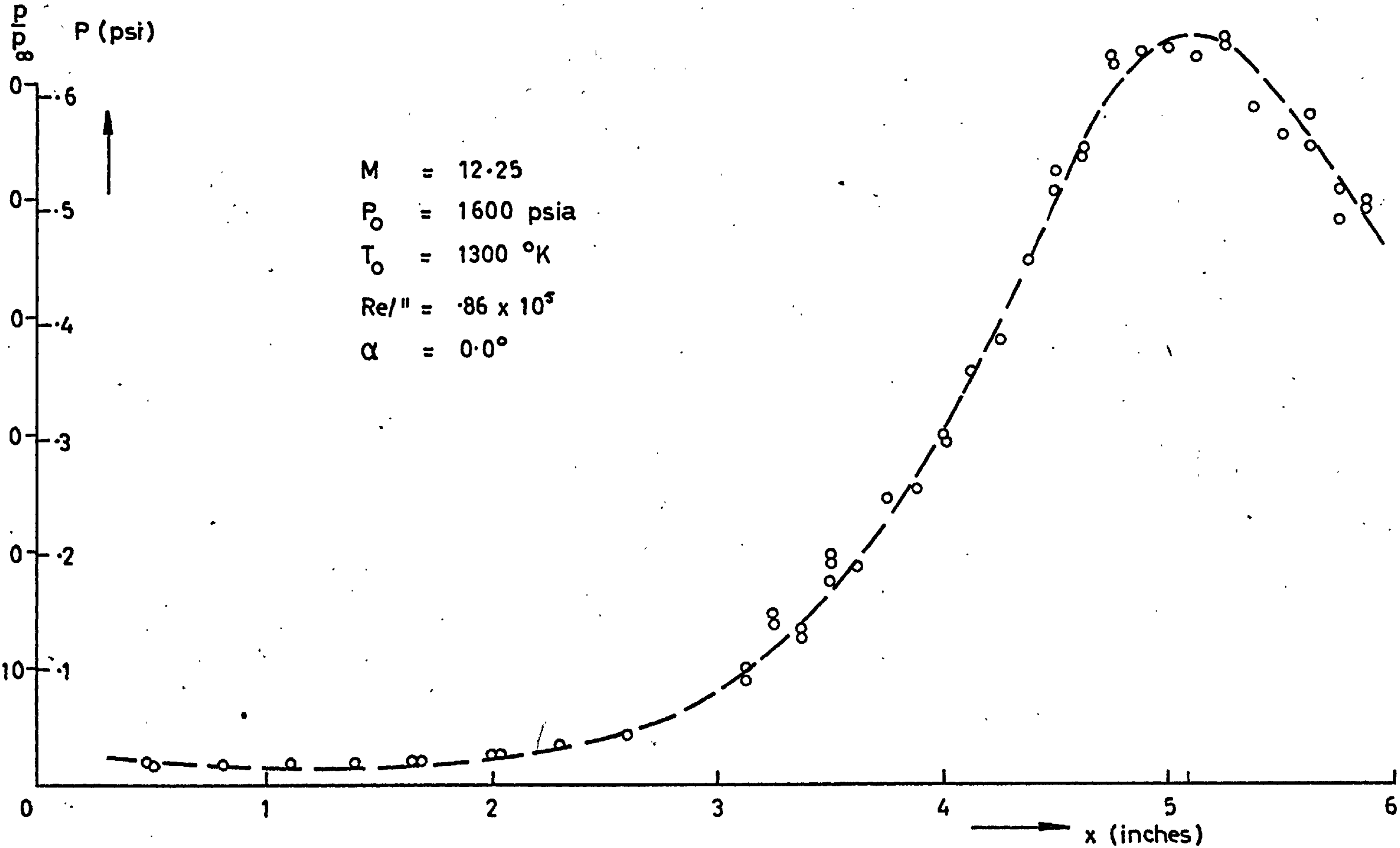

FIG. 17 PRESSURE MEASUREMENTS ON THE CUBIC MODEL

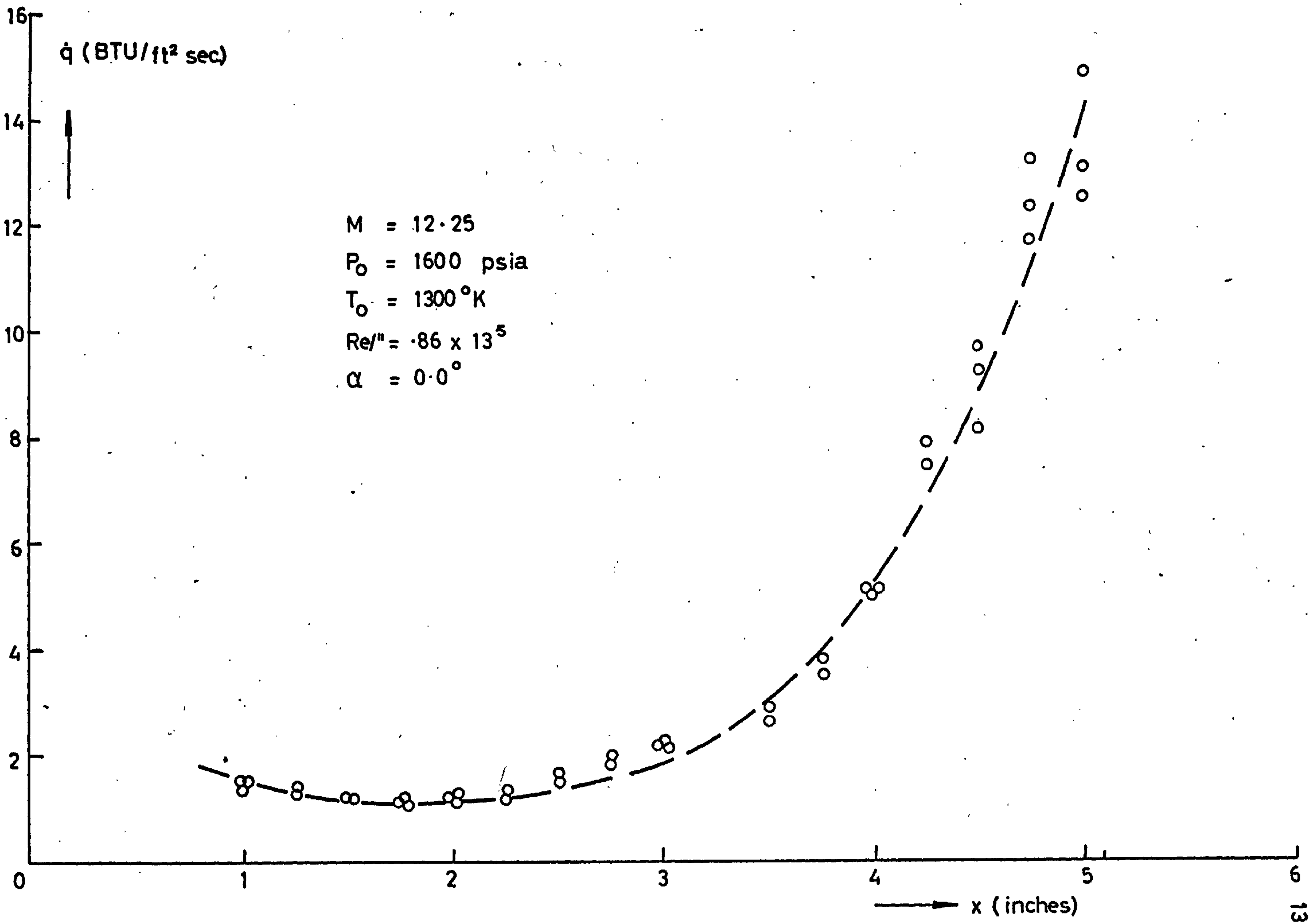

FIG. 18 HEAT TRANSFER ON THE CUBIC MODEL

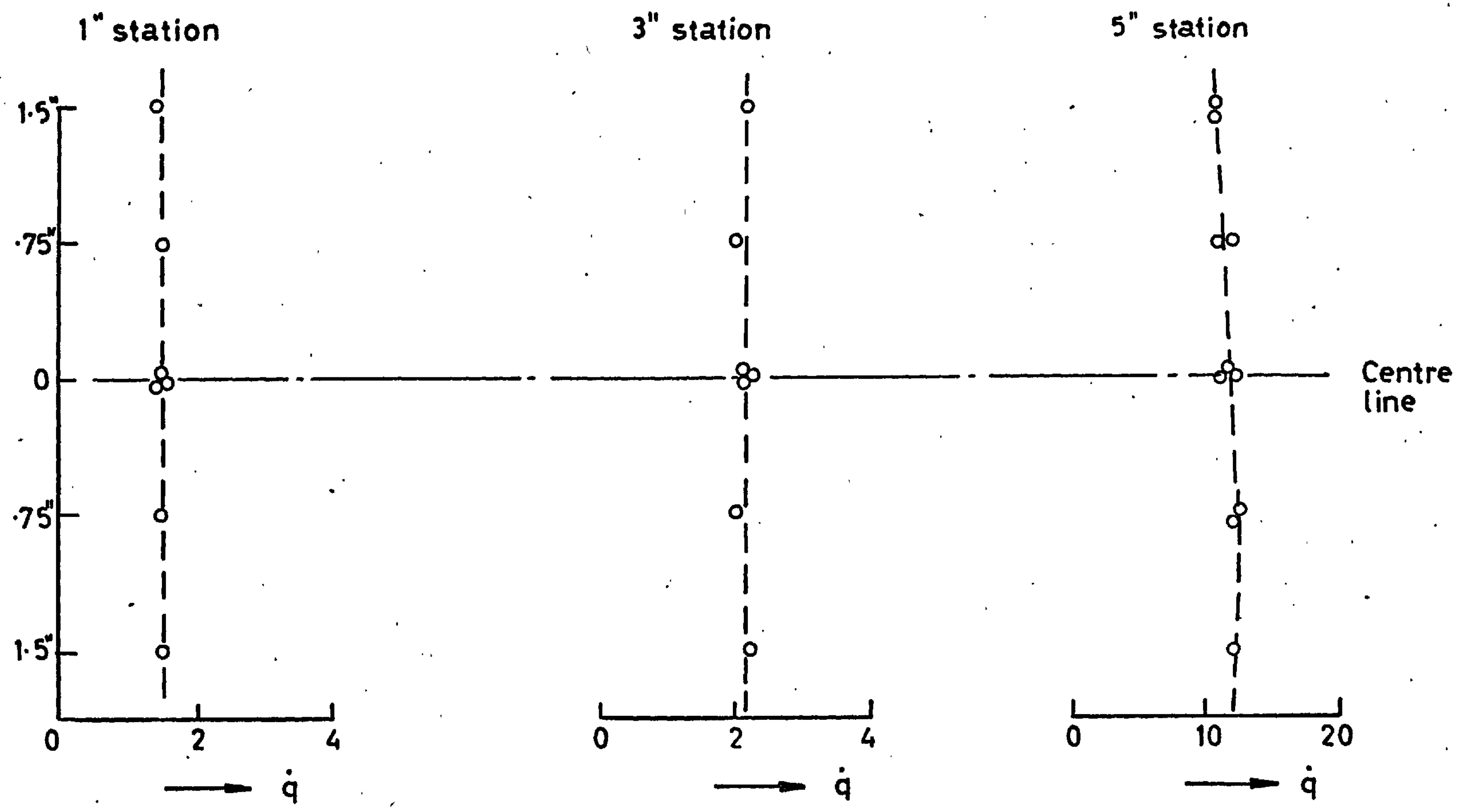

FIG. 19 SPANWISE HEAT TRANSFER DISTRIBUTIONS ON THE CONCAVE MODEL AT 1", 3", AND 5" FROM THE LEADING EDGE

$M = 12\cdot25$, $Re/" = \cdot86 \times 10^{6}$, $T_o = 1300\,^{\circ}K$

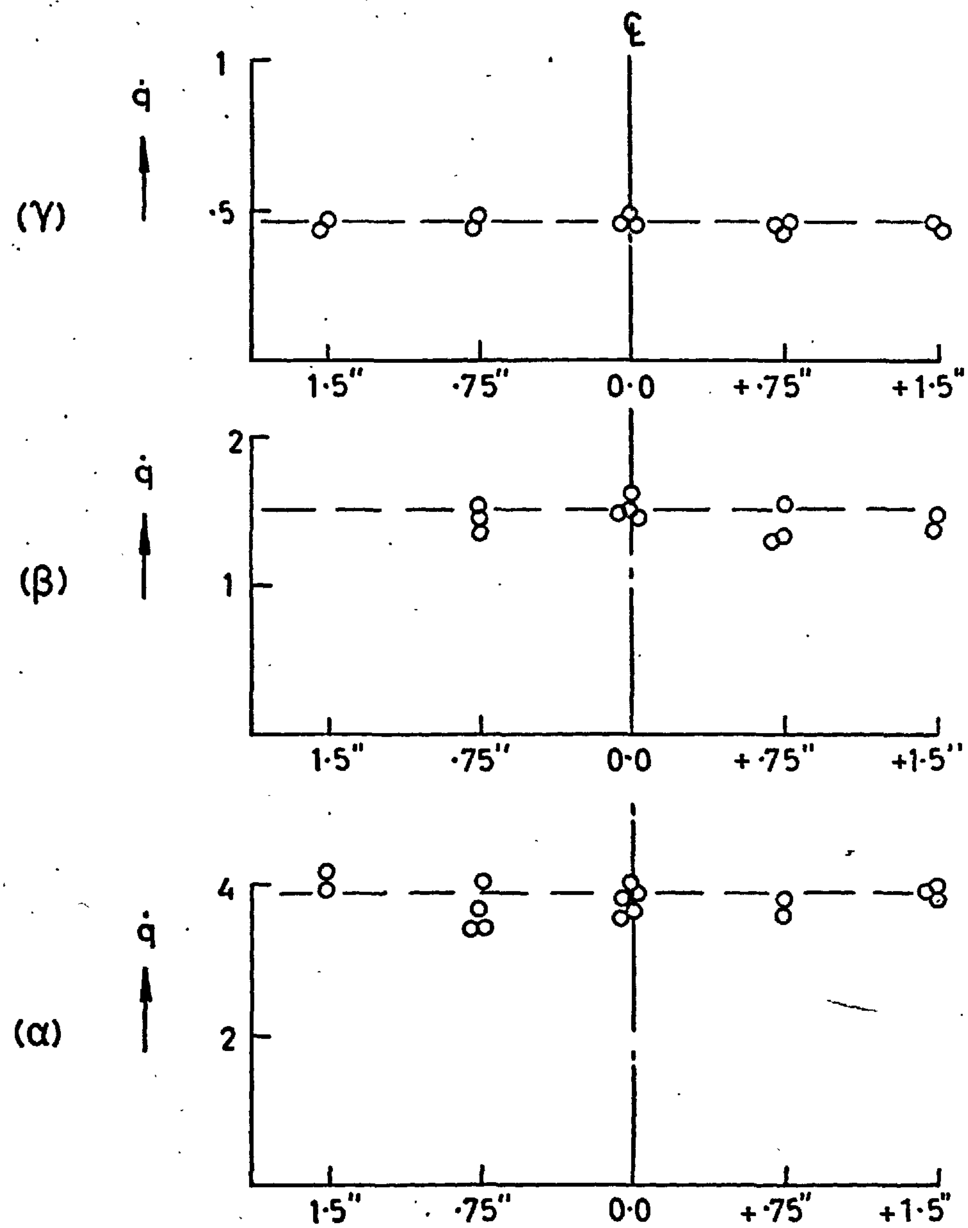

FIG. 20 SPANWISE HEAT TRANSFER MEASUREMENTS ON THE CONVEX SURFACE AT $M = 12 \cdot 25$, $P_o = 1600$ (lb/in^2) AT STATIONS :-

(α) 2" DISTANCE FROM LEADING EDGE

(β) 5" " " " "

(γ) 8" " " " "

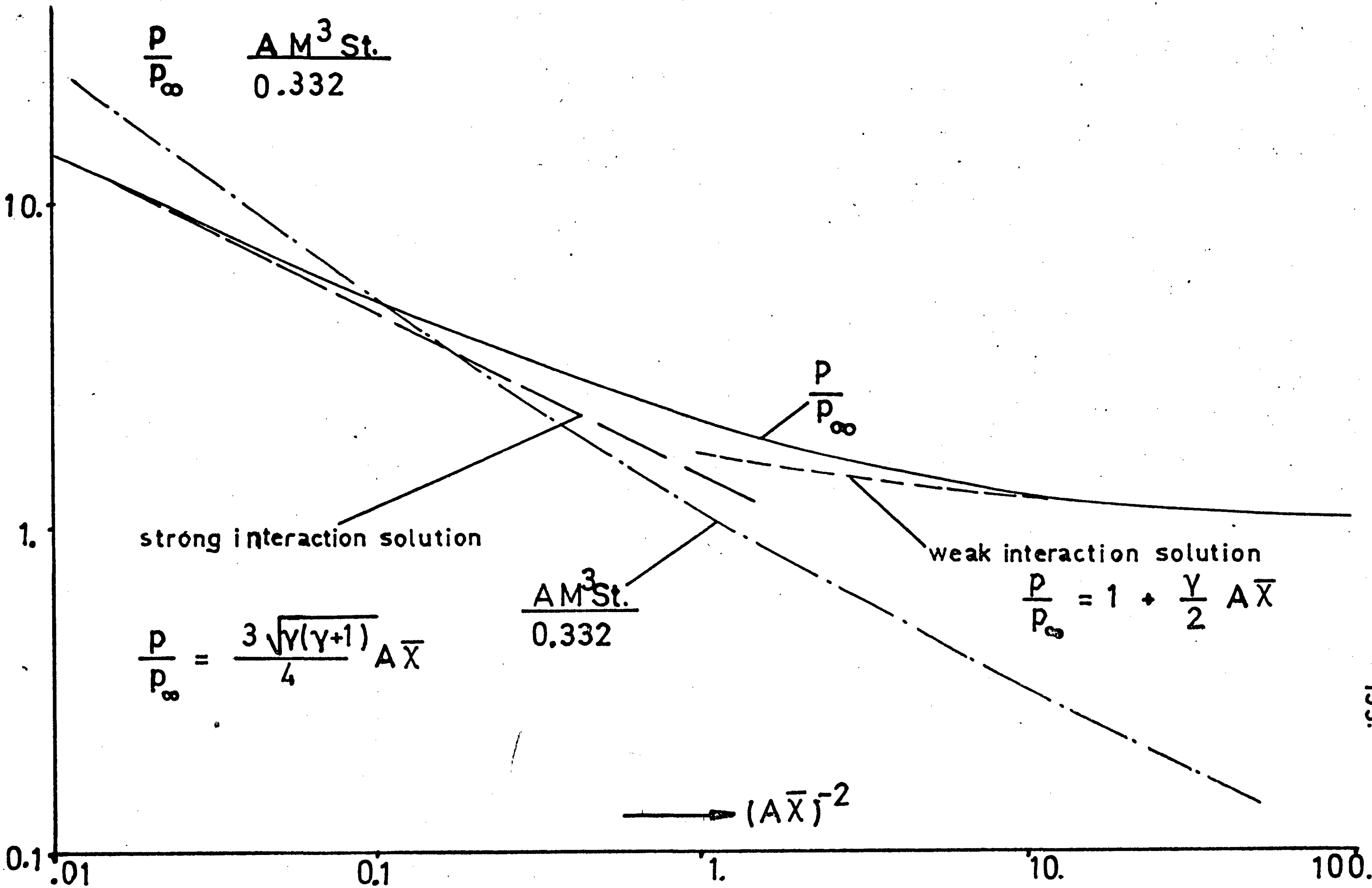

Fig. (21) Theoretical prediction of pressure and heat transfer on a flat plate using modified Cheng's method

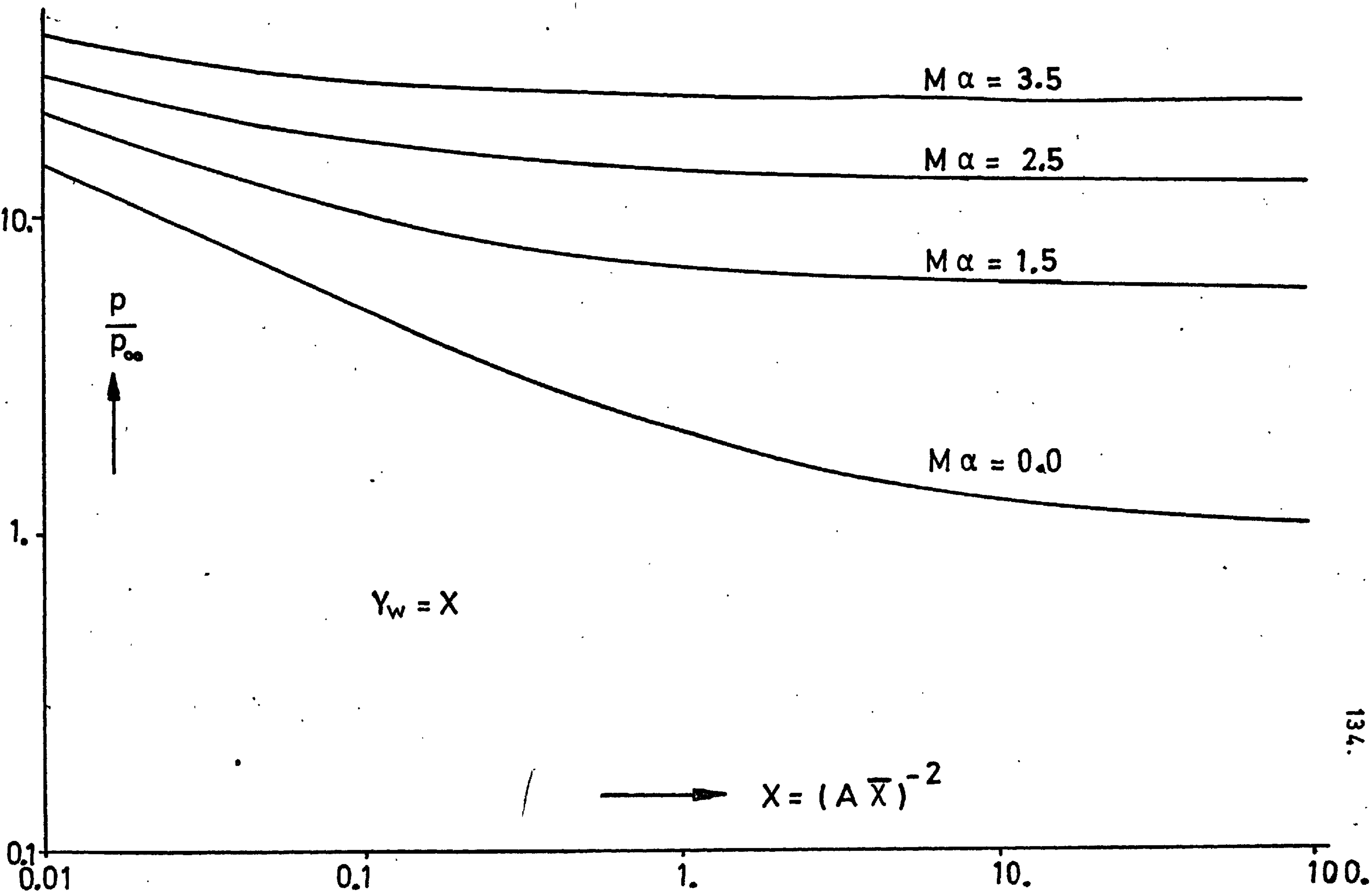

Fig. (22) Theoretical pressure distributions on a wedge using modified Cheng's method

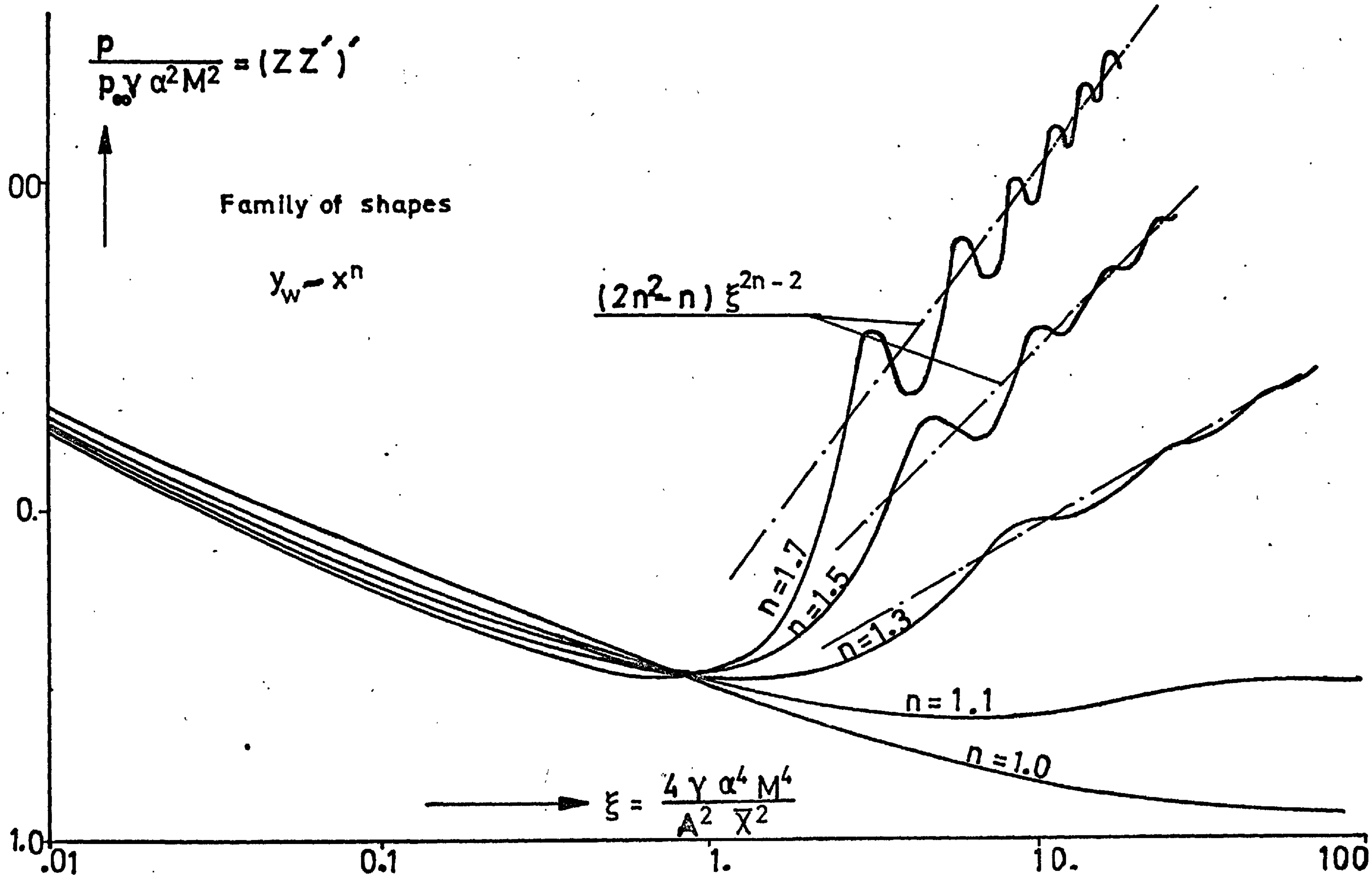

Fig.(23) Theoretical prediction of pressure for power law bodies

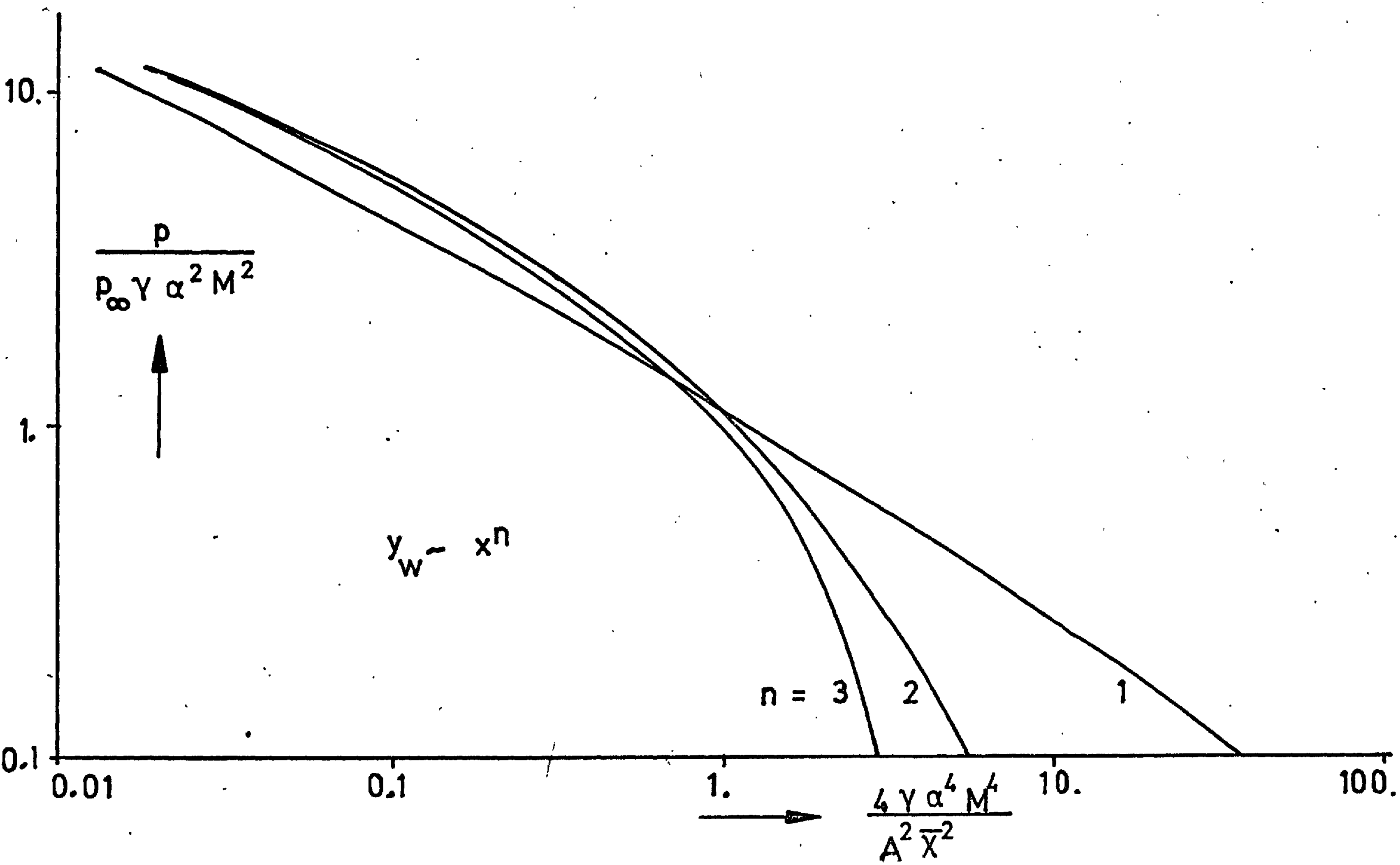

Fig. (24) Theoretical prediction of pressure over convex surfaces

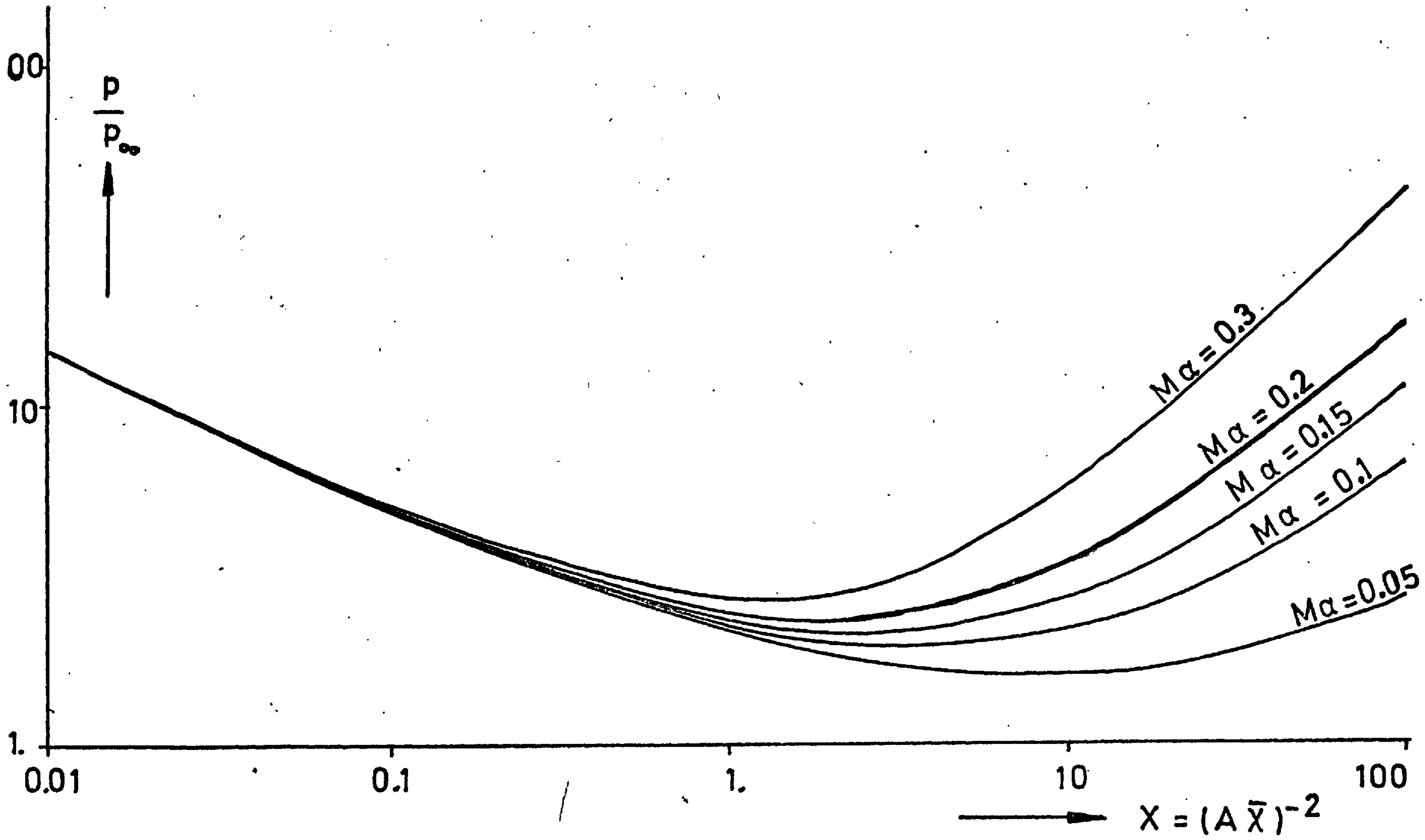

Fig (25) Theoretical prediction of pressure over $Y_w \sim X^{1.2}$

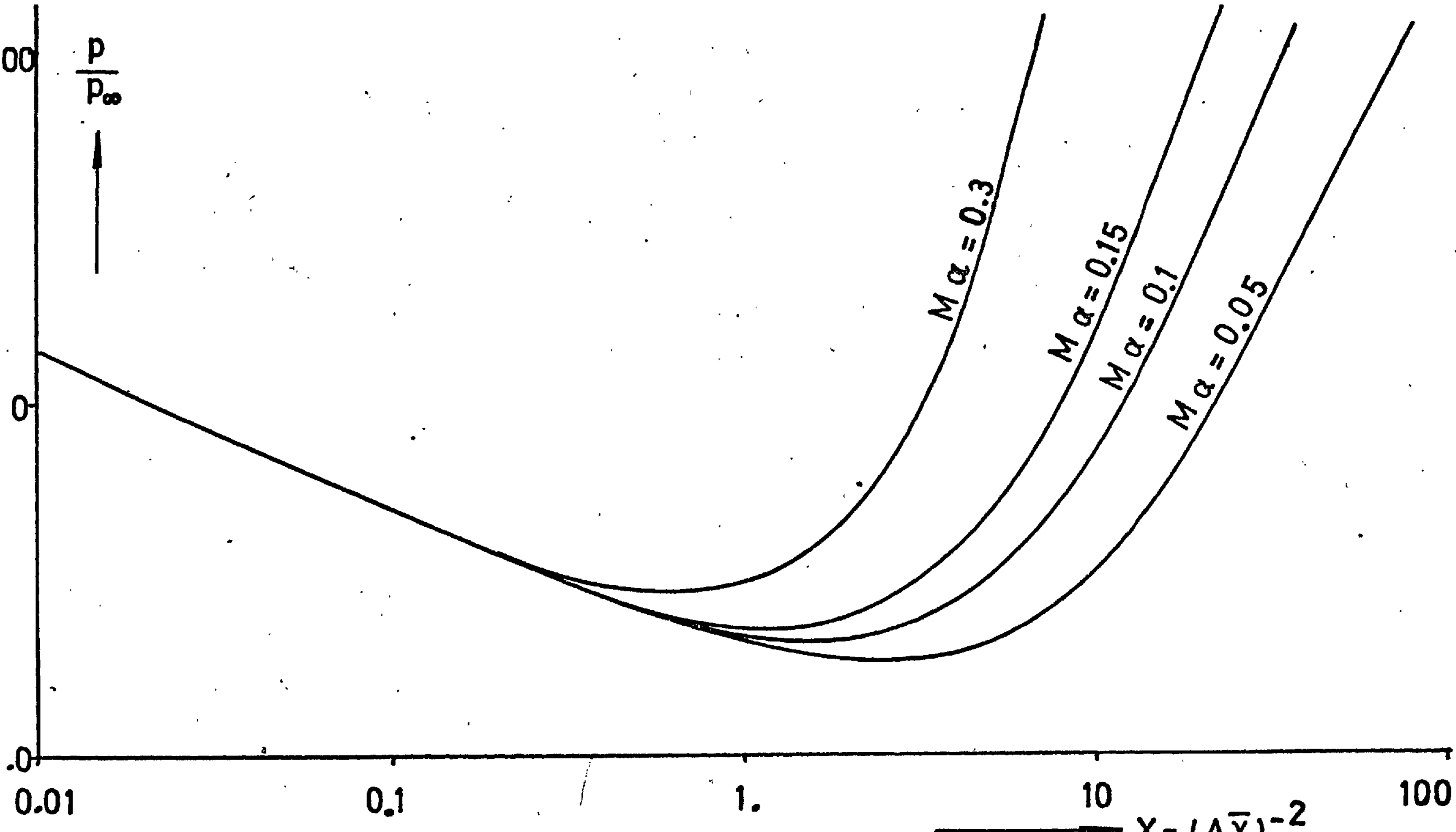

Fig.(26) Theoretical prediction of pressure over $Y_W \sim X^2$

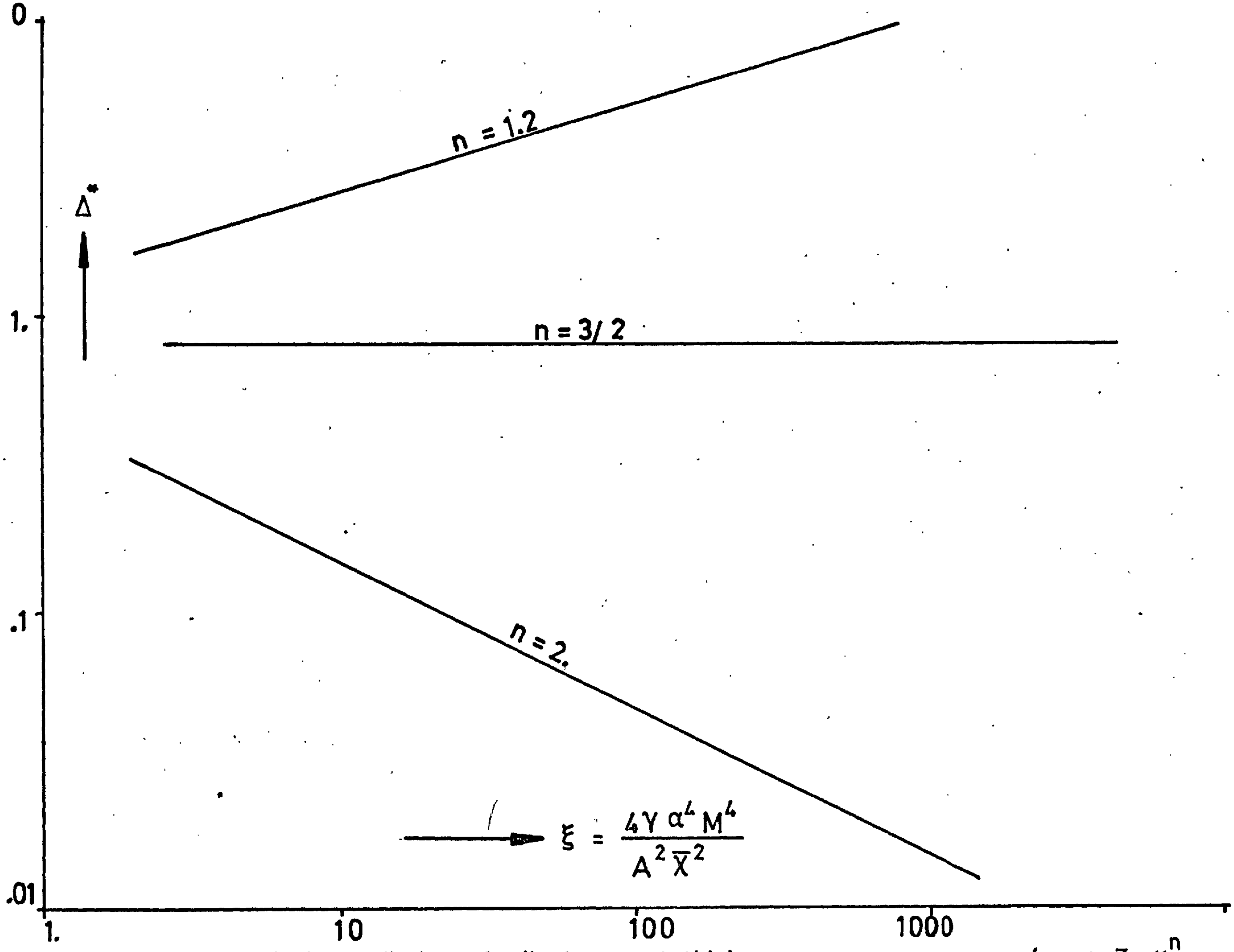

Fig.(27) Theoretical prediction of displacement thickness over concave surfaces $Z_w=\xi^n$

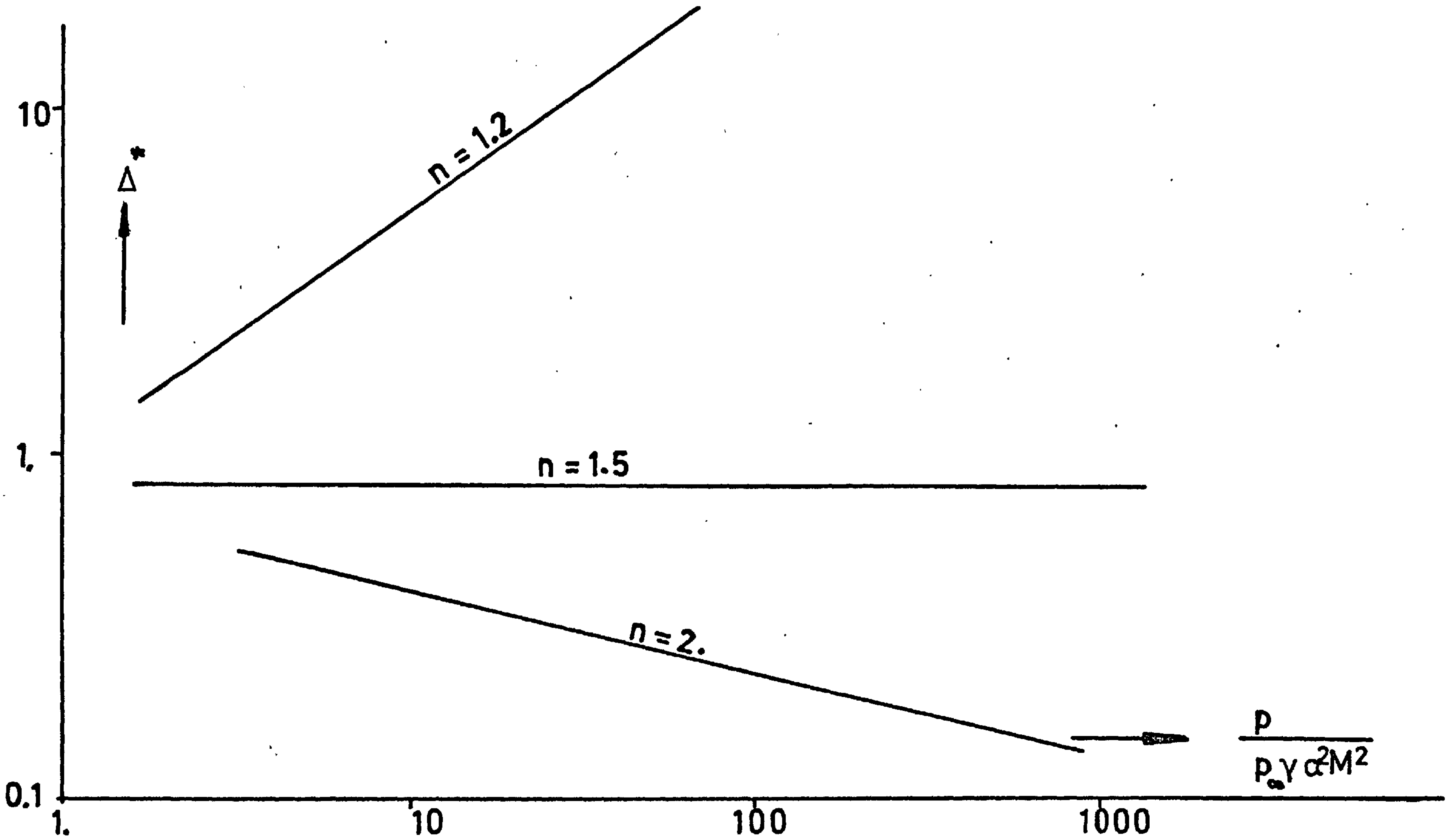

Fig.(28) The distribution of the scaled displacement thickness as a function of pressure ratio for concave surfaces $Z_w = \xi^n$ using Cheng's method

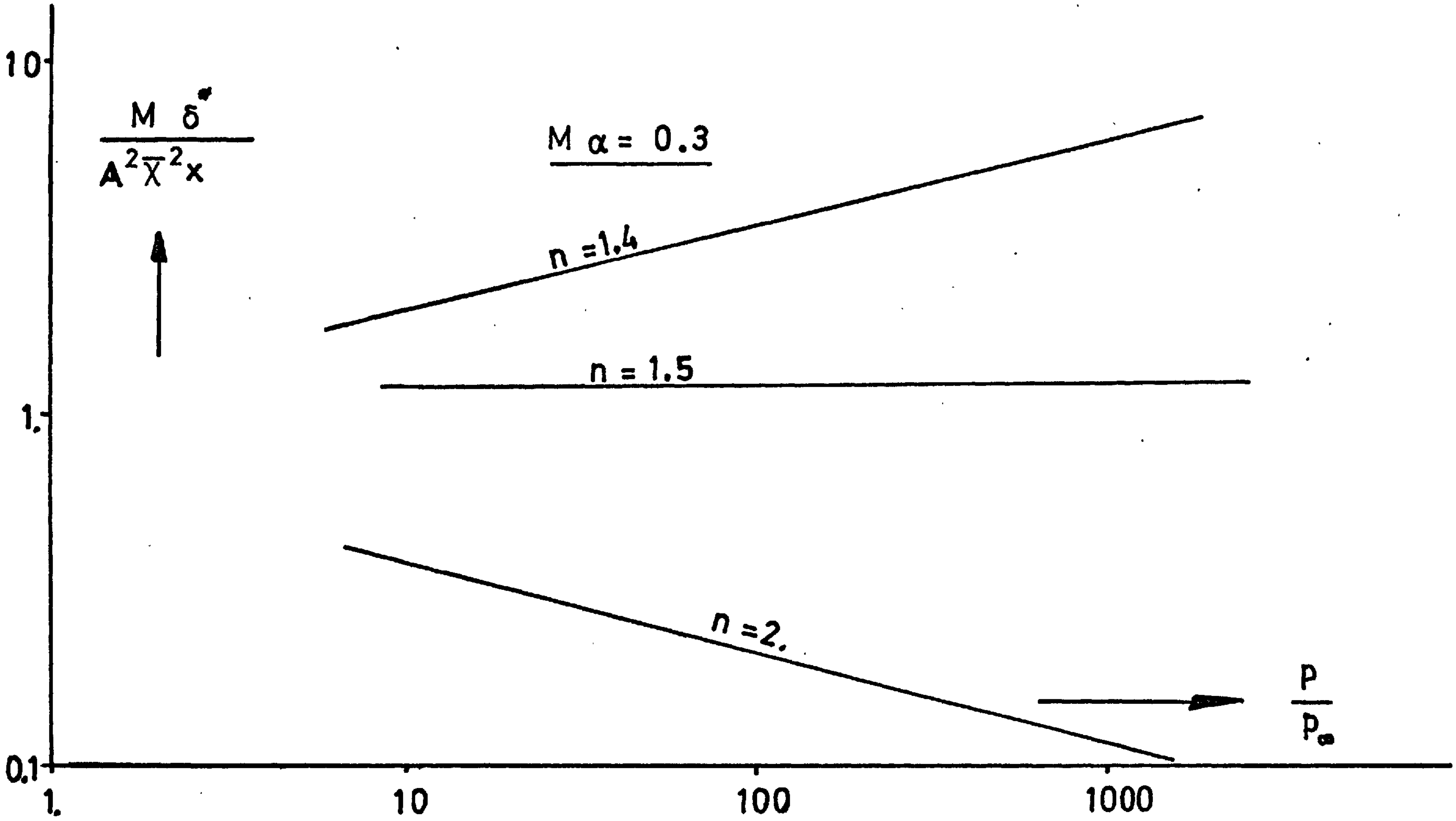

Fig.(29) Variation of displacement thickness with respect to p/p_∞ over concave surfaces $Yw = X^n$ using modified Chengs method

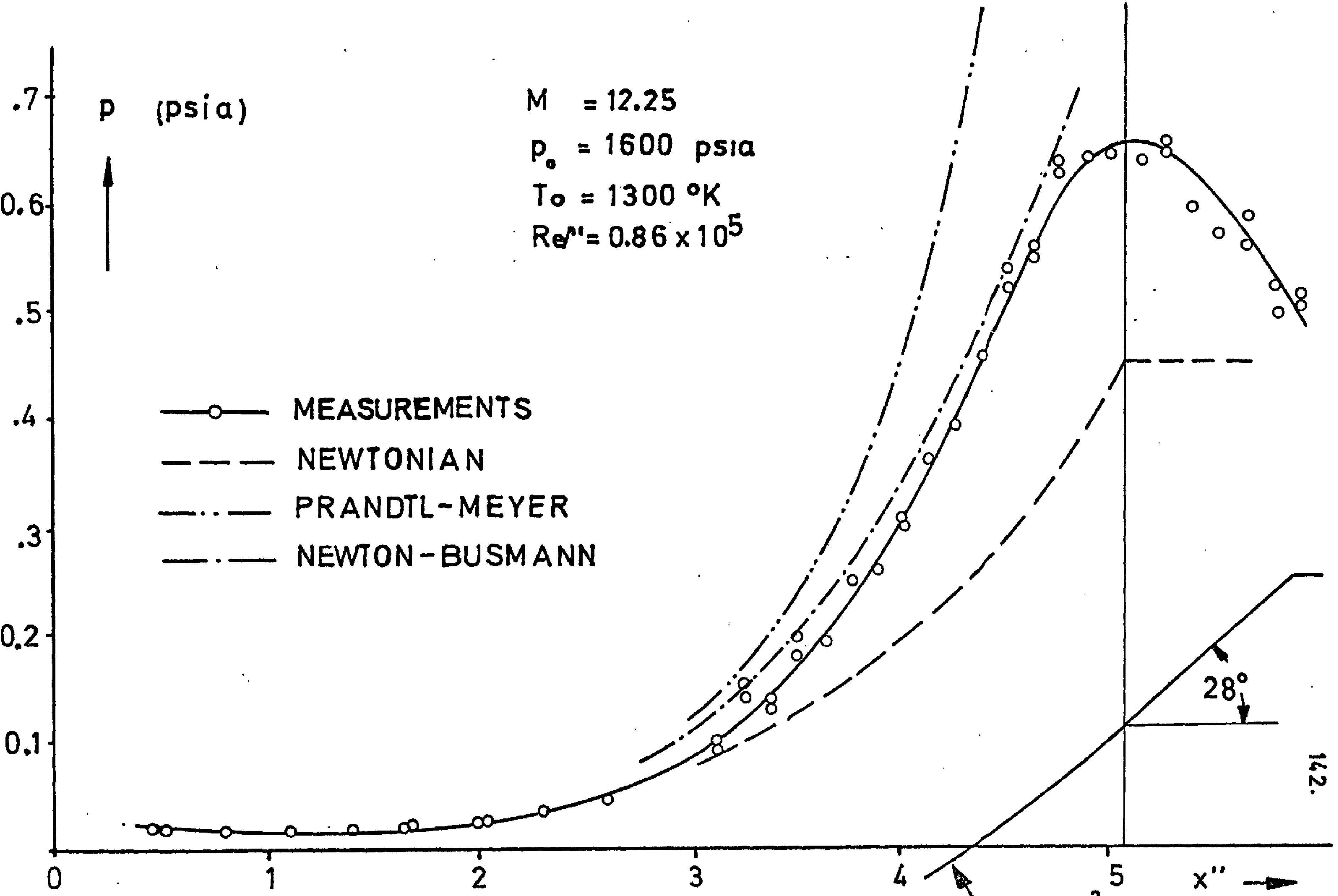

FIG. (30) PRESSURE DISTRIBUTION ON THE CUBIC SURFACE $Y_W = X^3/150$

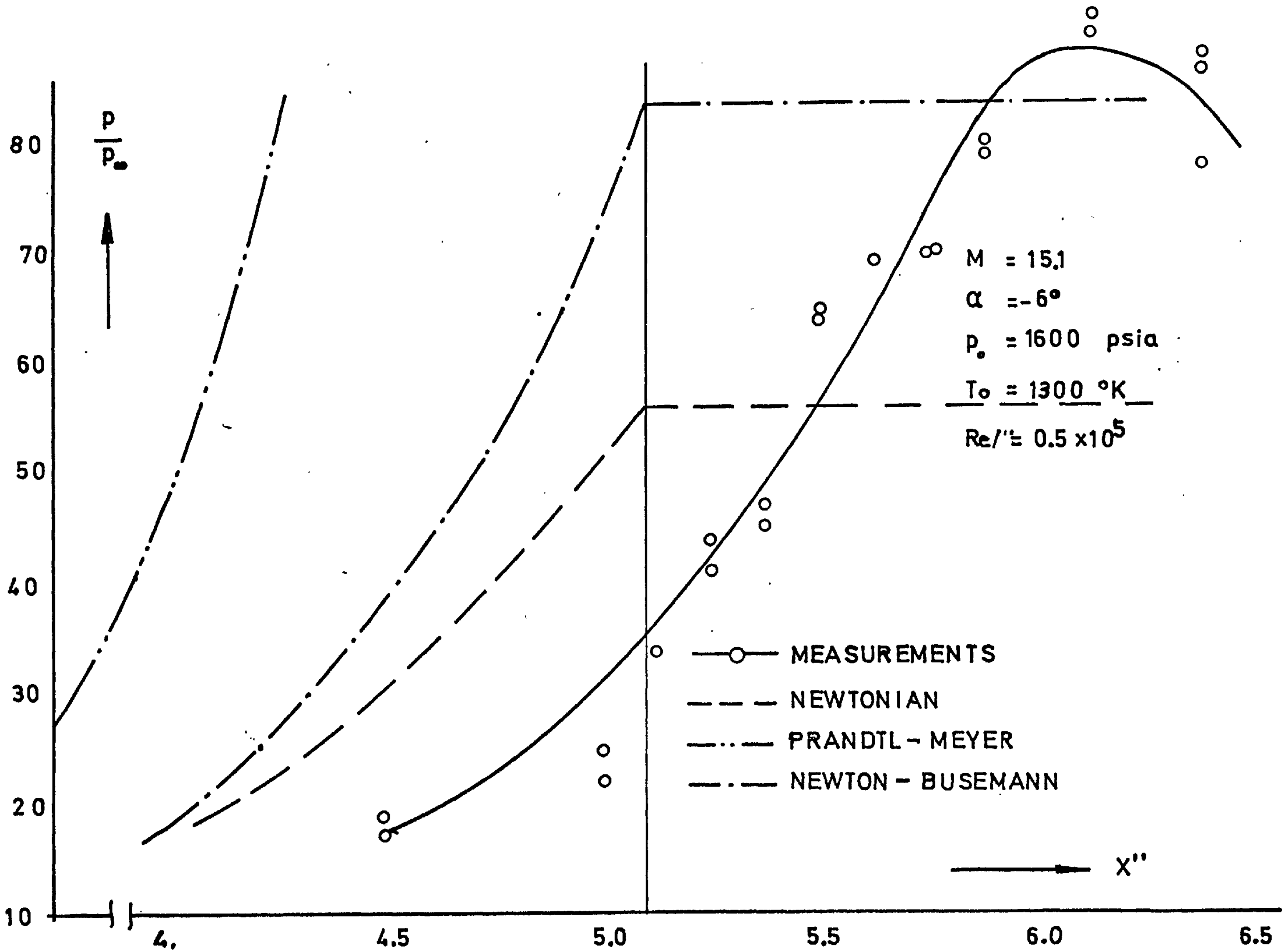

FIG. (31) PRESSURE DISTRIBUTION ON THE CUBIC SURFACE

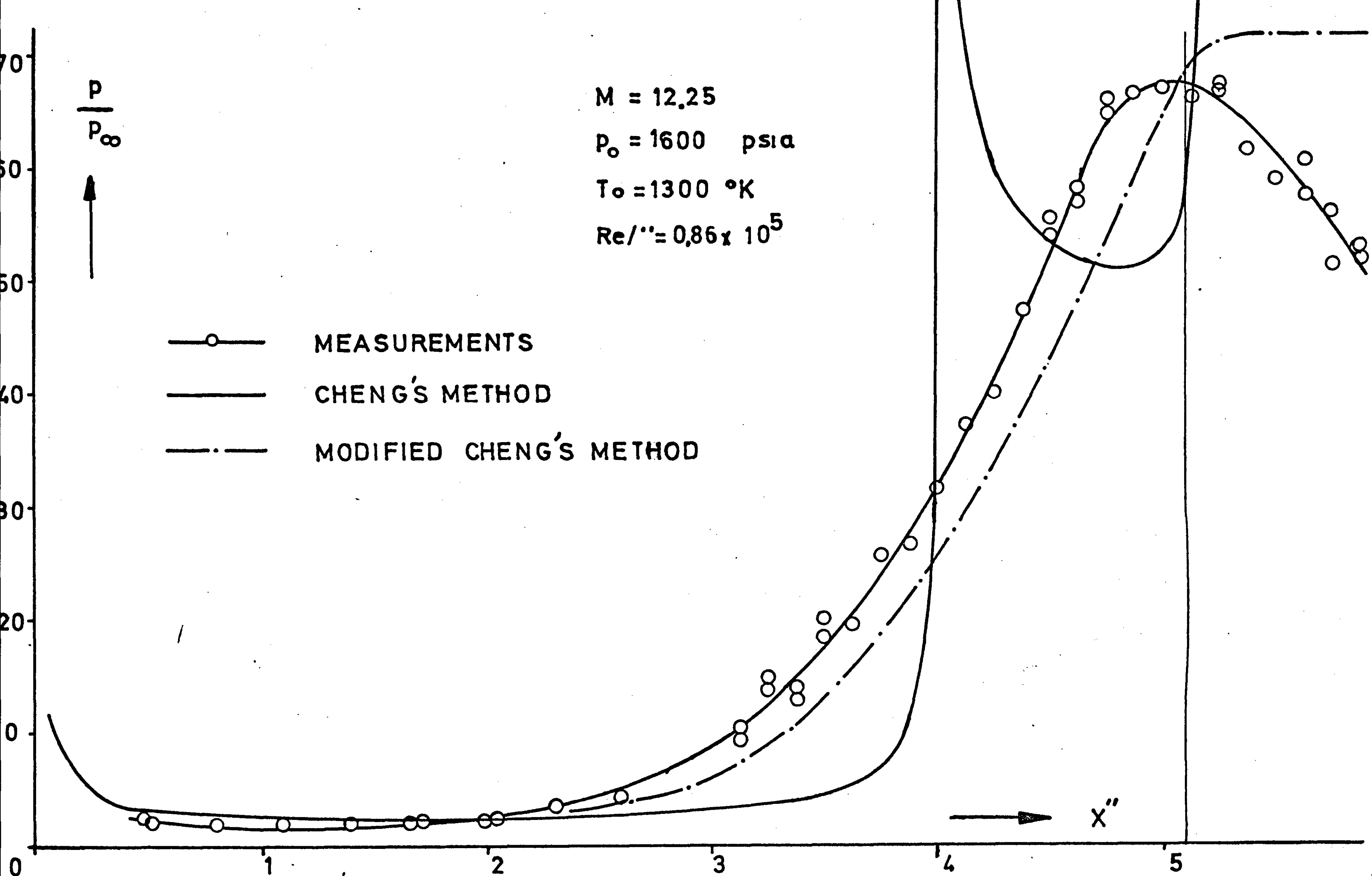

FIG. (32) PRESSURE MEASUREMENT TO THE CUBIC SURFACE COMPARED WITH THE VISCOUS INTERACTION THEORY

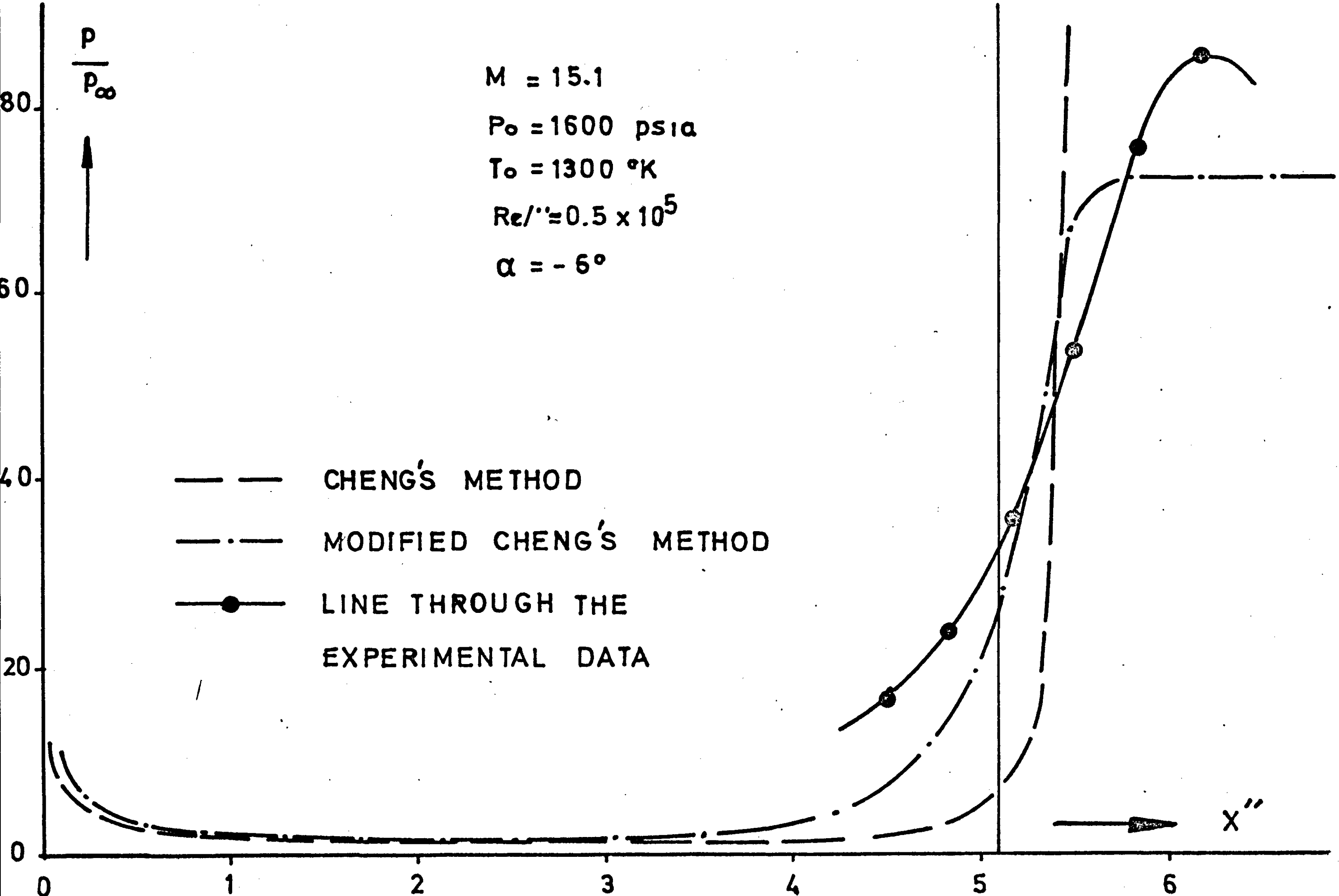

FIG.(33) A COMPARISON BETWEEN EXPRIMENTAL DATA AND VISCOUS INTERACTION THEORY

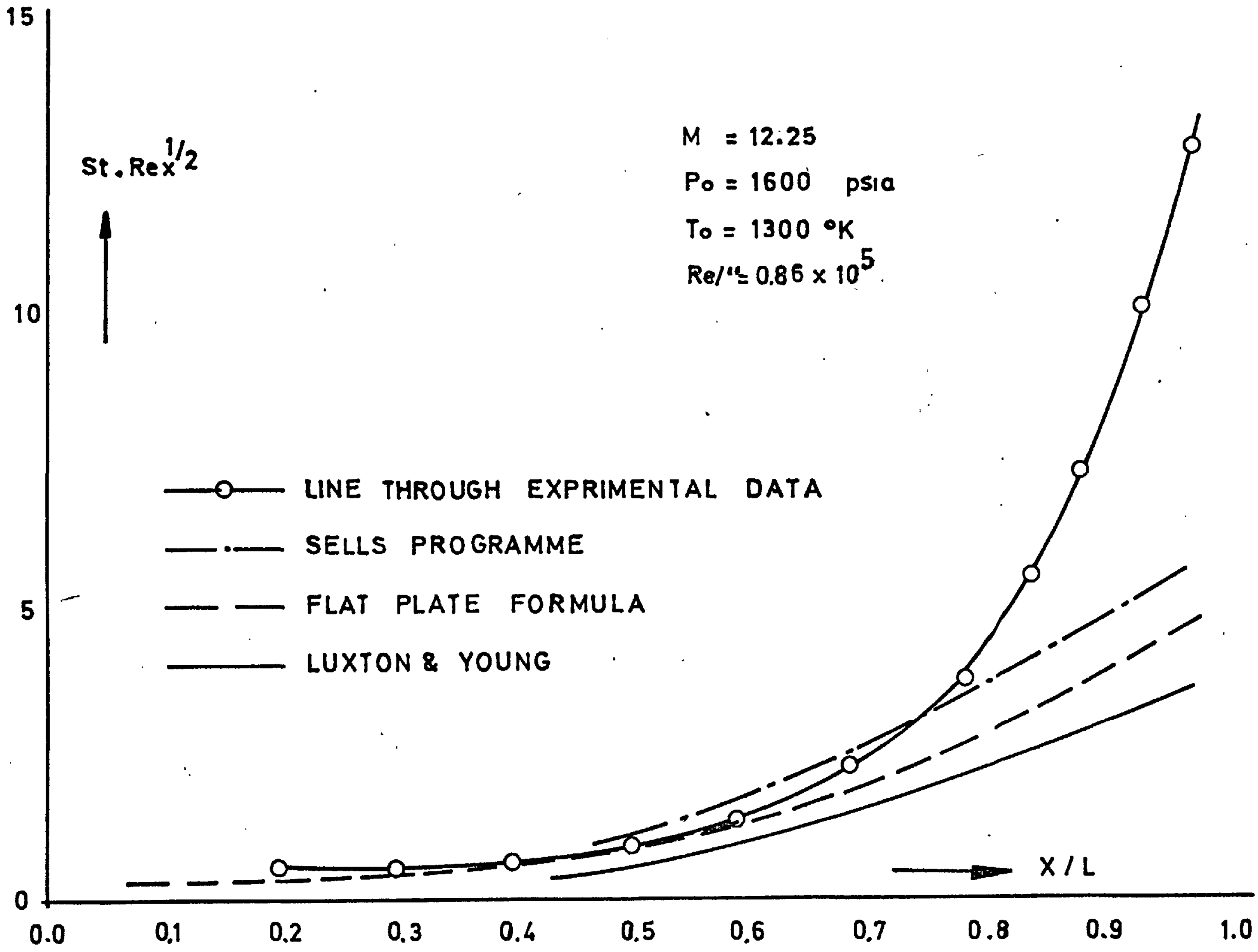

FIG. (34) HEAT TRANSFER MEASUREMENT ON THE CUBIC SURFACE

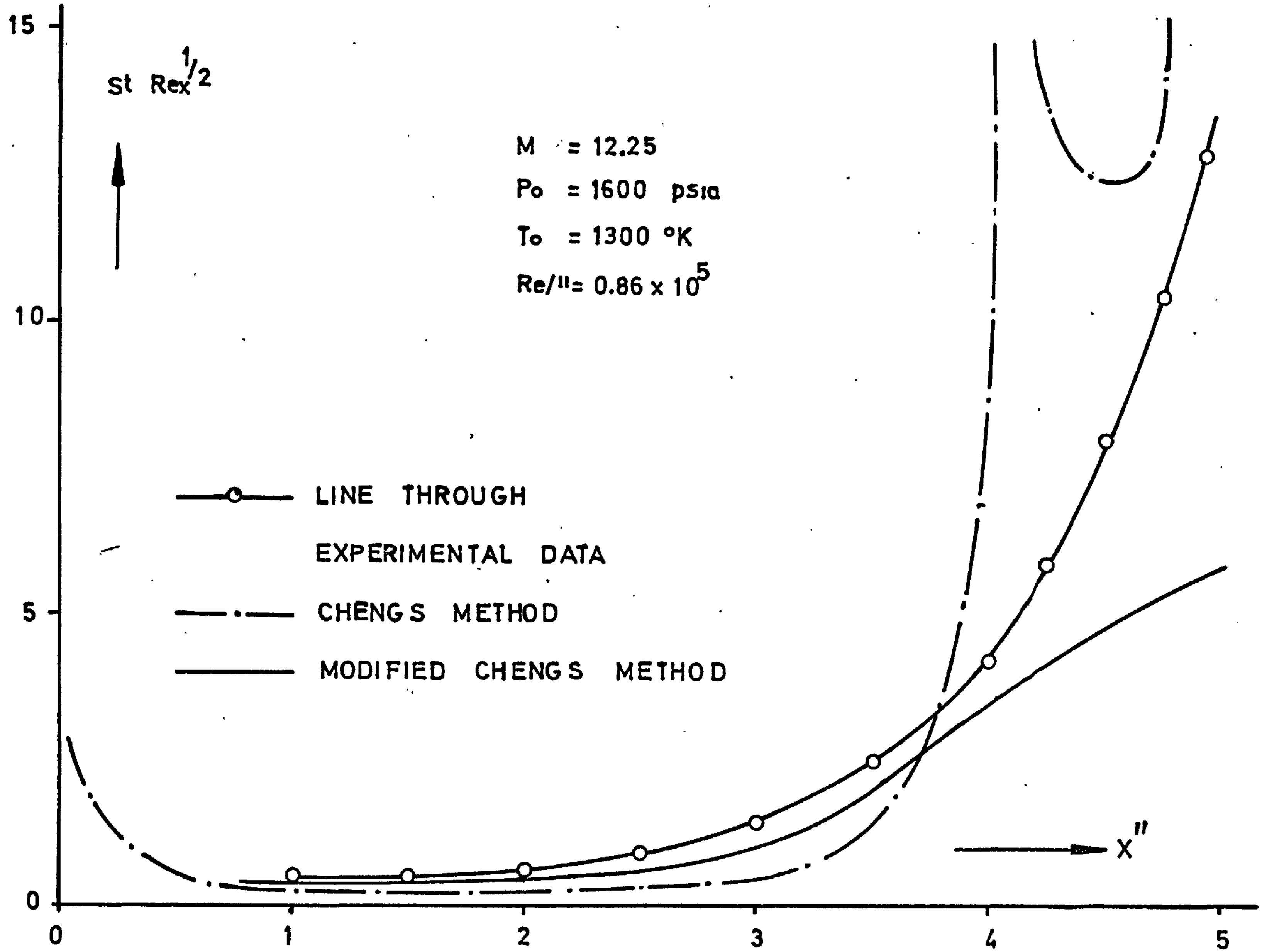

FIG. (35) HEAT TRANSFER ON THE CUBIC MODEL

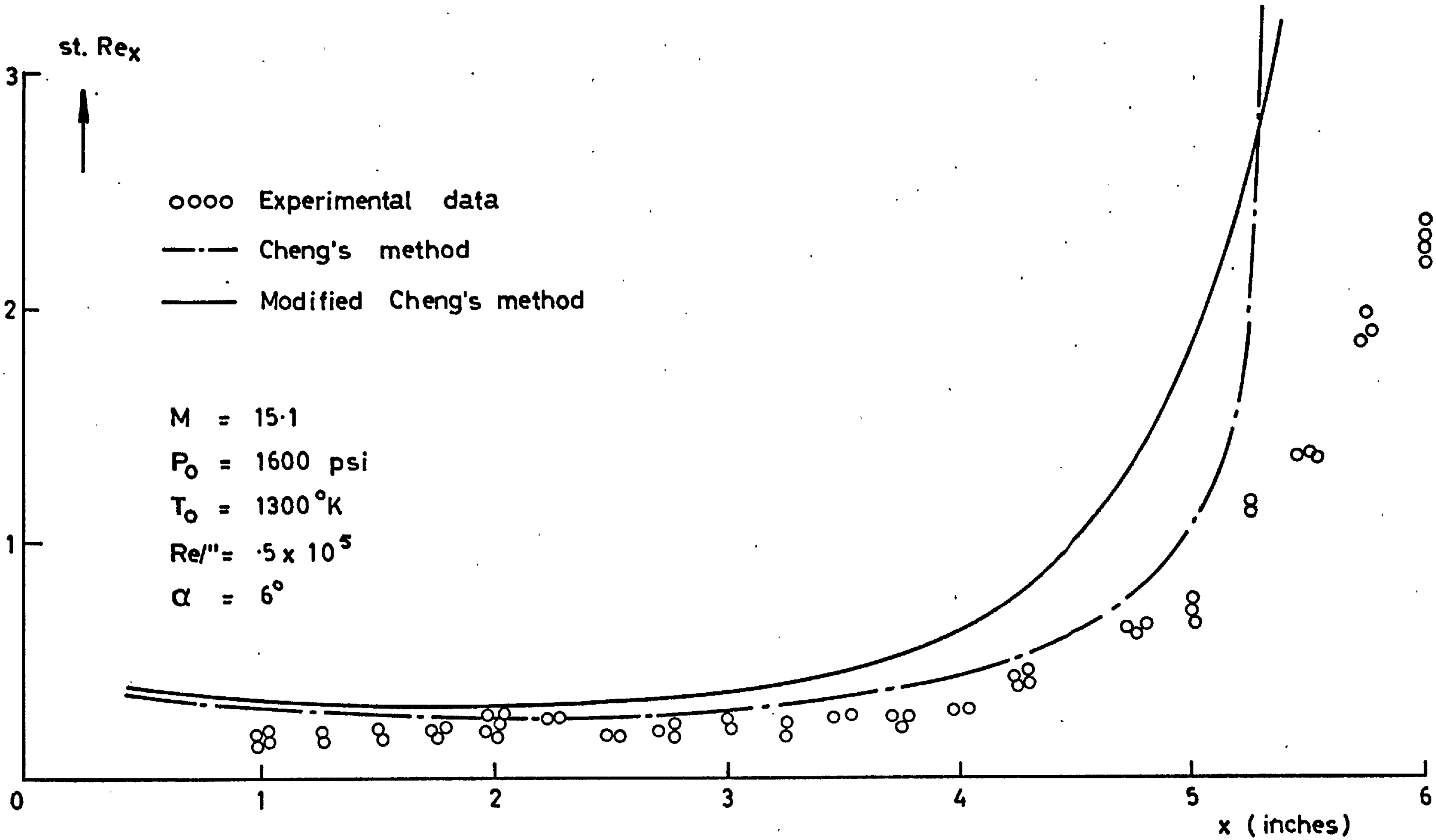

FIG. 36 HEAT TRANSFER RATE ON CUBIC MODEL

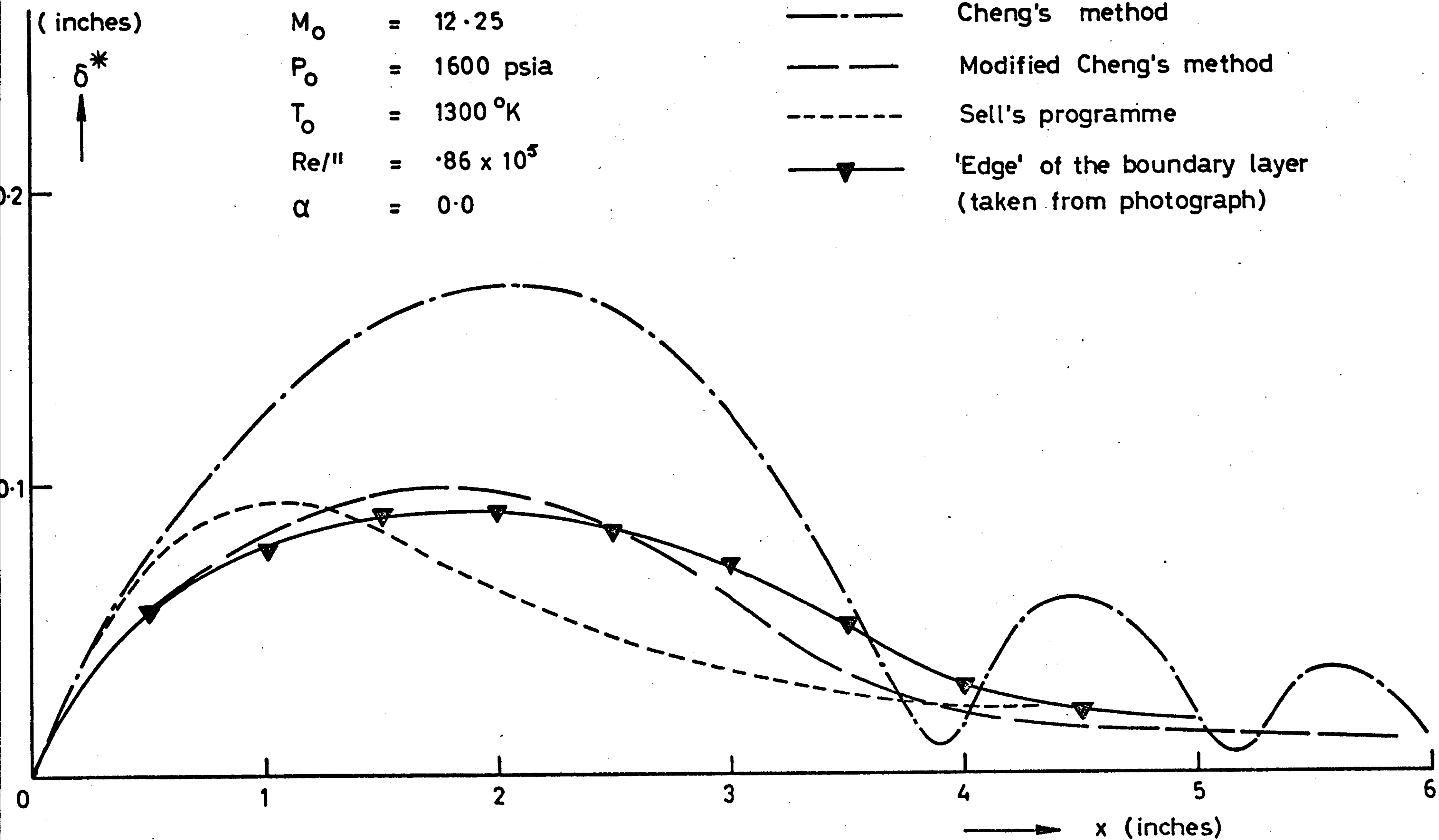

FIG. 37 DISPLACEMENT THICKNESS TO THE CUBIC MODEL

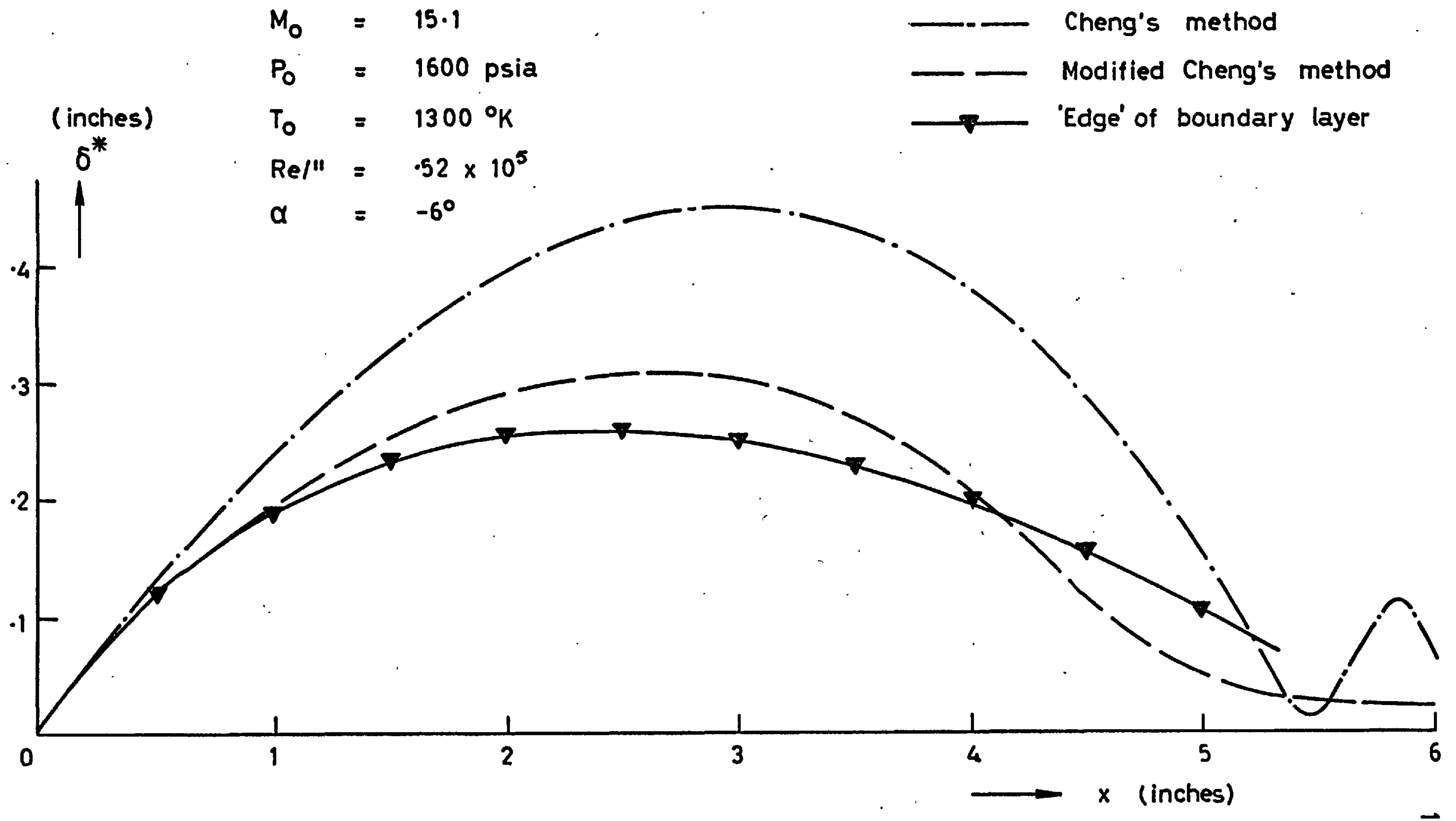

FIG. 38 DISPLACEMENT THICKNESS TO THE CUBIC MODEL

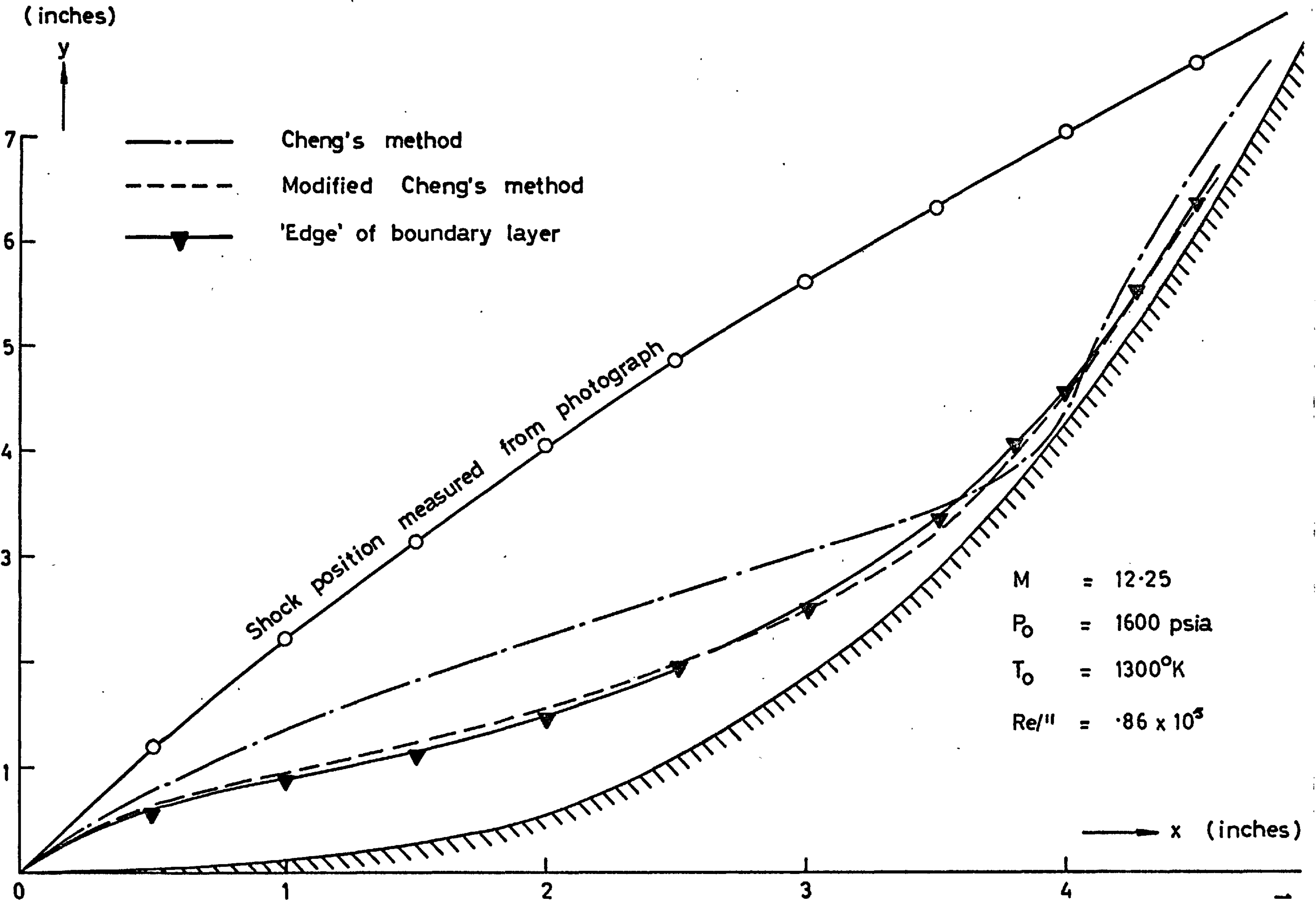

FIG. 39 BOUNDARY LAYER GROWTH OVER THE CUBIC BODY

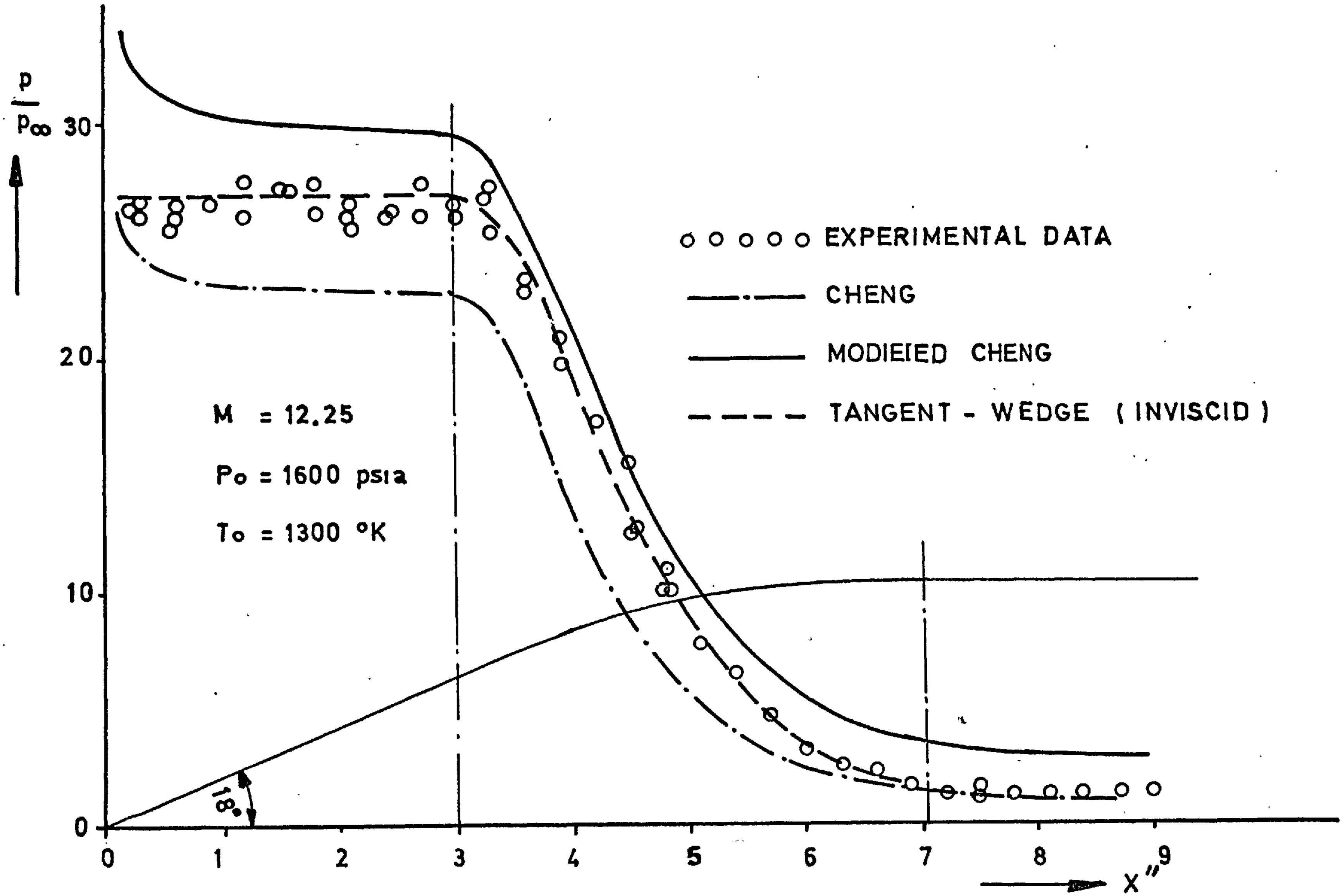

FIG.(40) A COMARISON OF PRESSURE MEASUREMENT ON THE CONVEX MODEL WITH THEORY

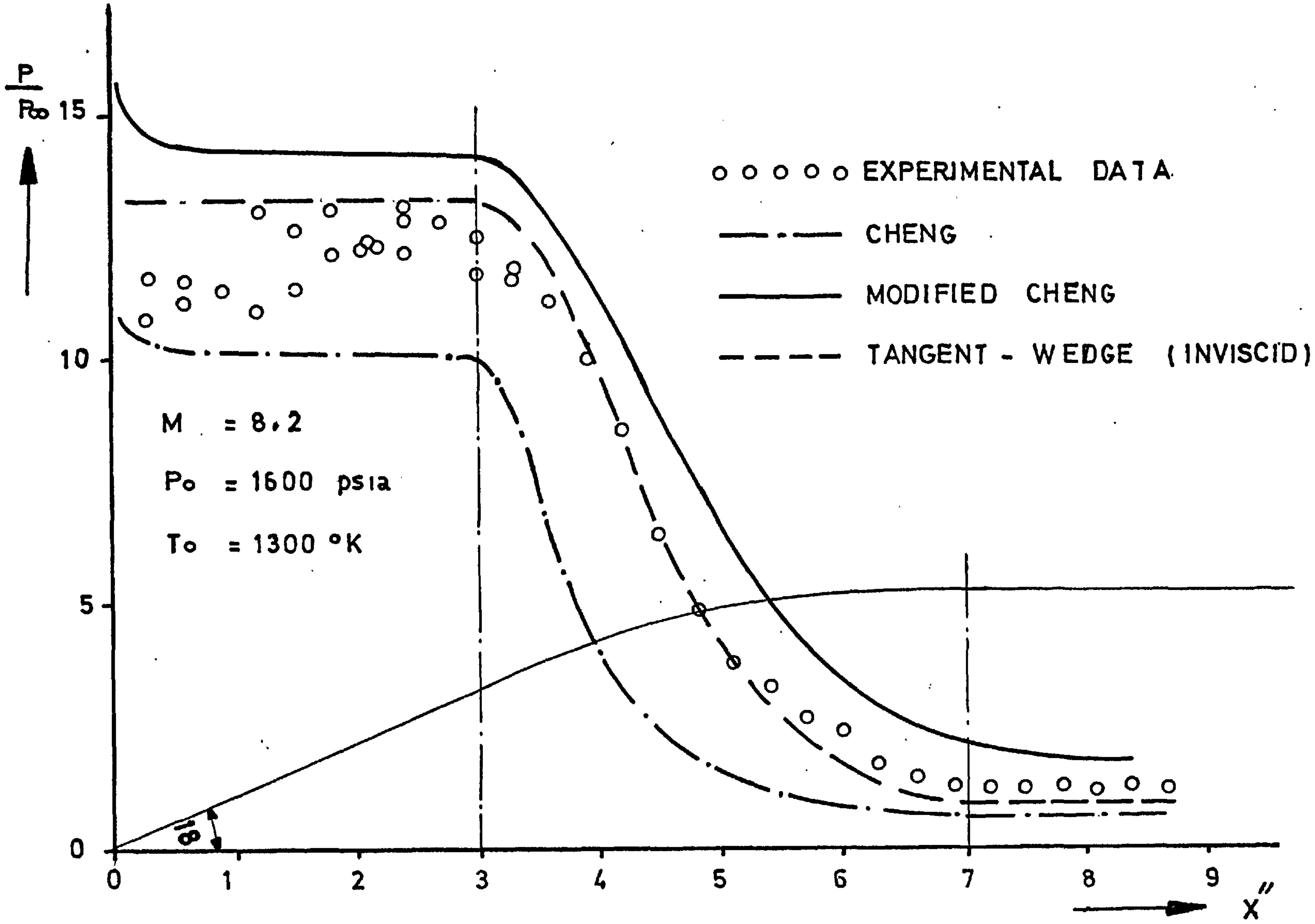

FIG. (41) A COMPARISON OF PRESSURE MEASUREMENT ON THE CONVEX MODEL WITH THEORY

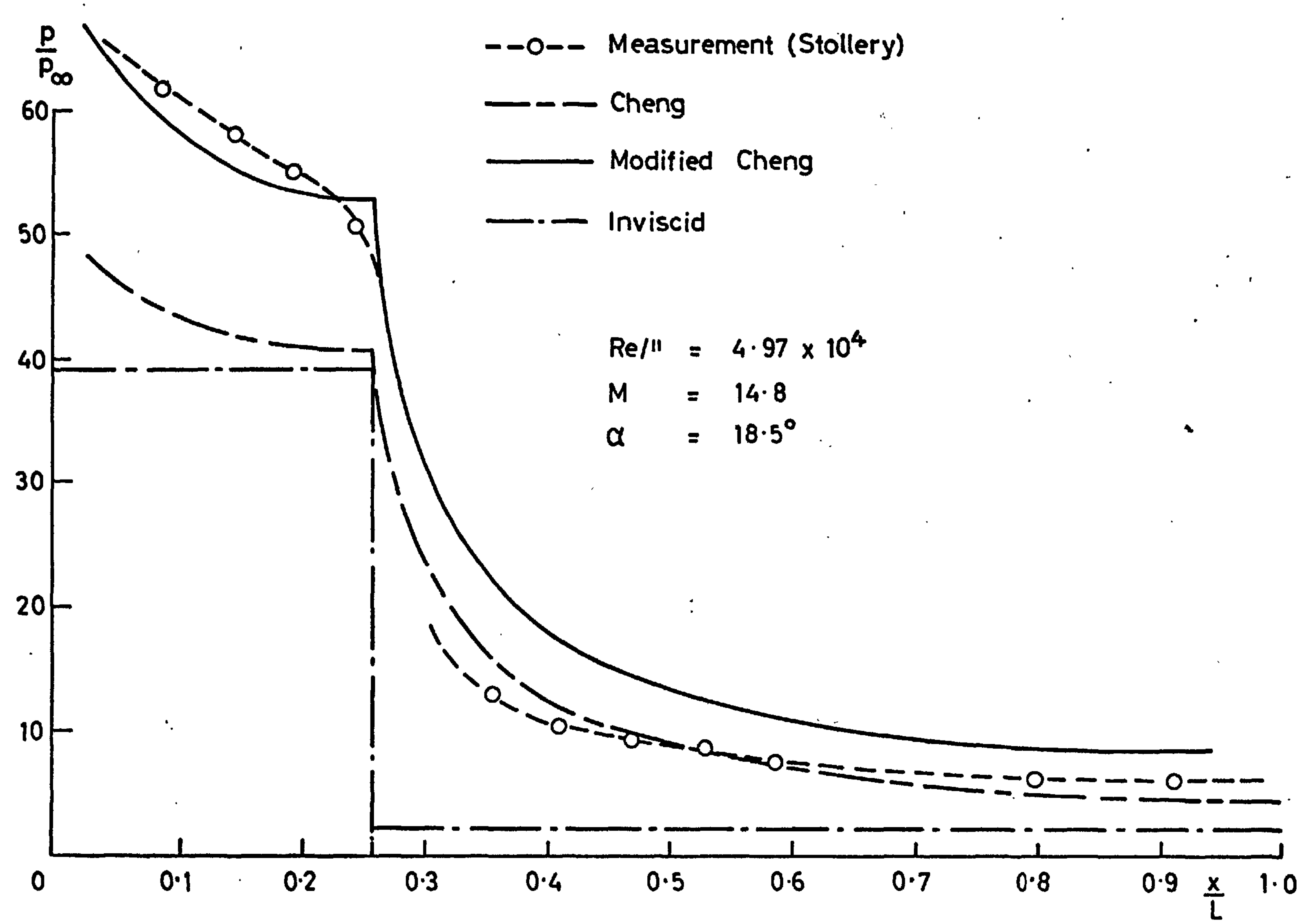

FIG. 42 PRESSURE DISTRIBUTION OVER AN EXPANSION CORNER (L = 2·5")

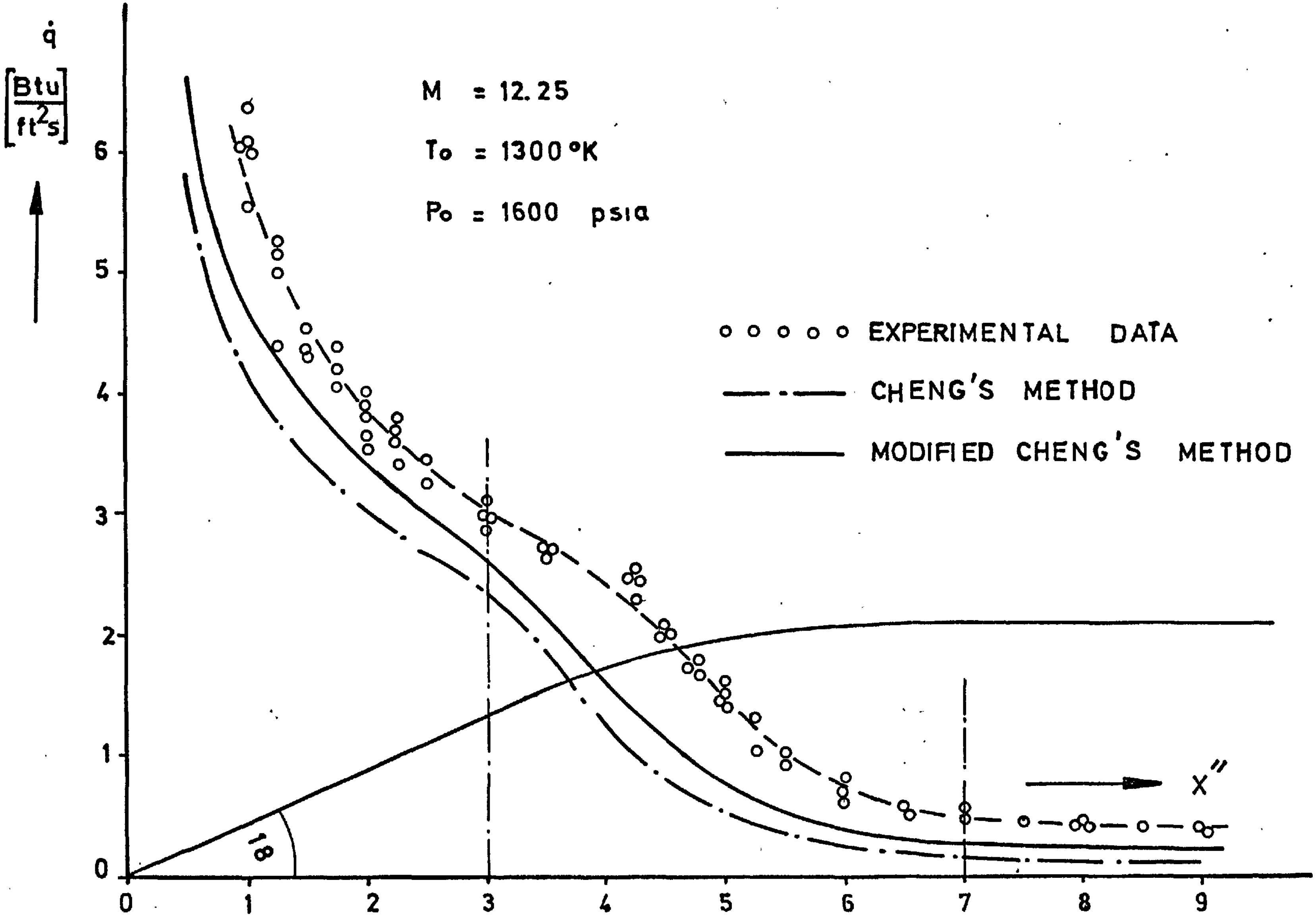

FIG. (43) A COMPARISON OF HEAT TRANSFER MEASUREMENTS WITH VISCOUS INTERACTION THEORY

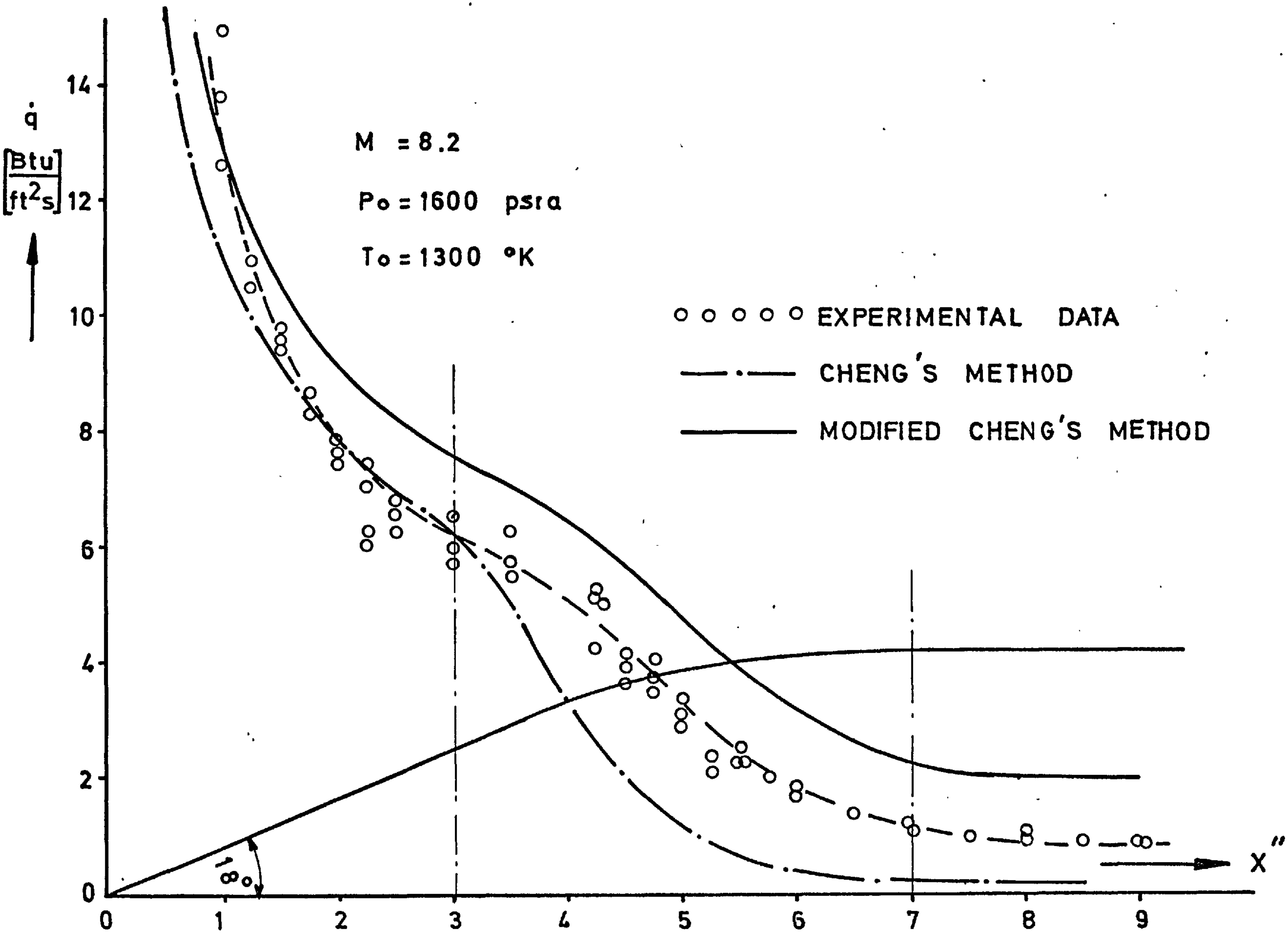

FIG.(44) A COMPARISON OF HEAT TRANSFER MEASUREMENTS WITH VISCOUS INTERACTION THEORY

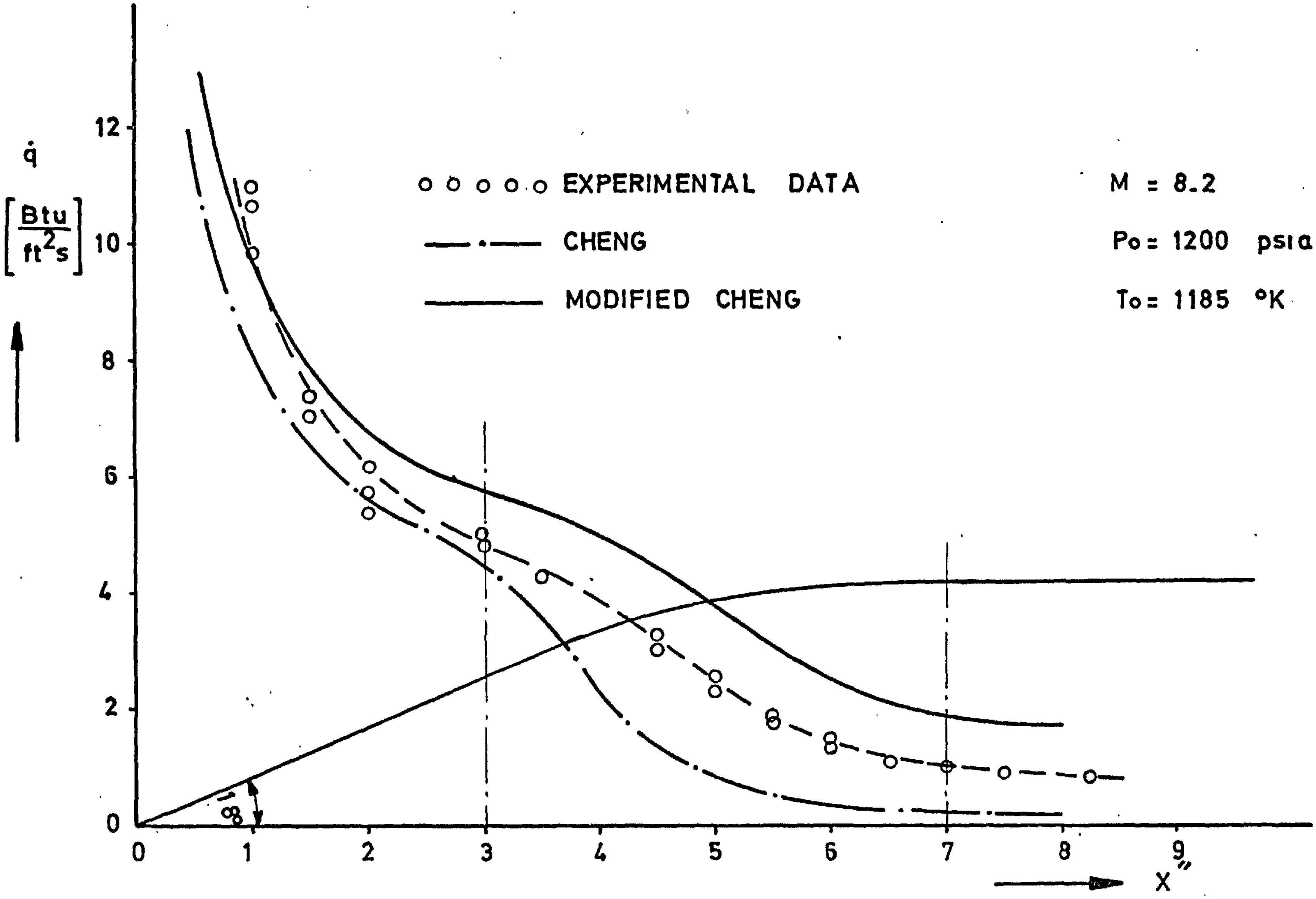

FIG. (45) HEAT TRANSFER MEASUREMENTS ON THE CONVEX MODEL

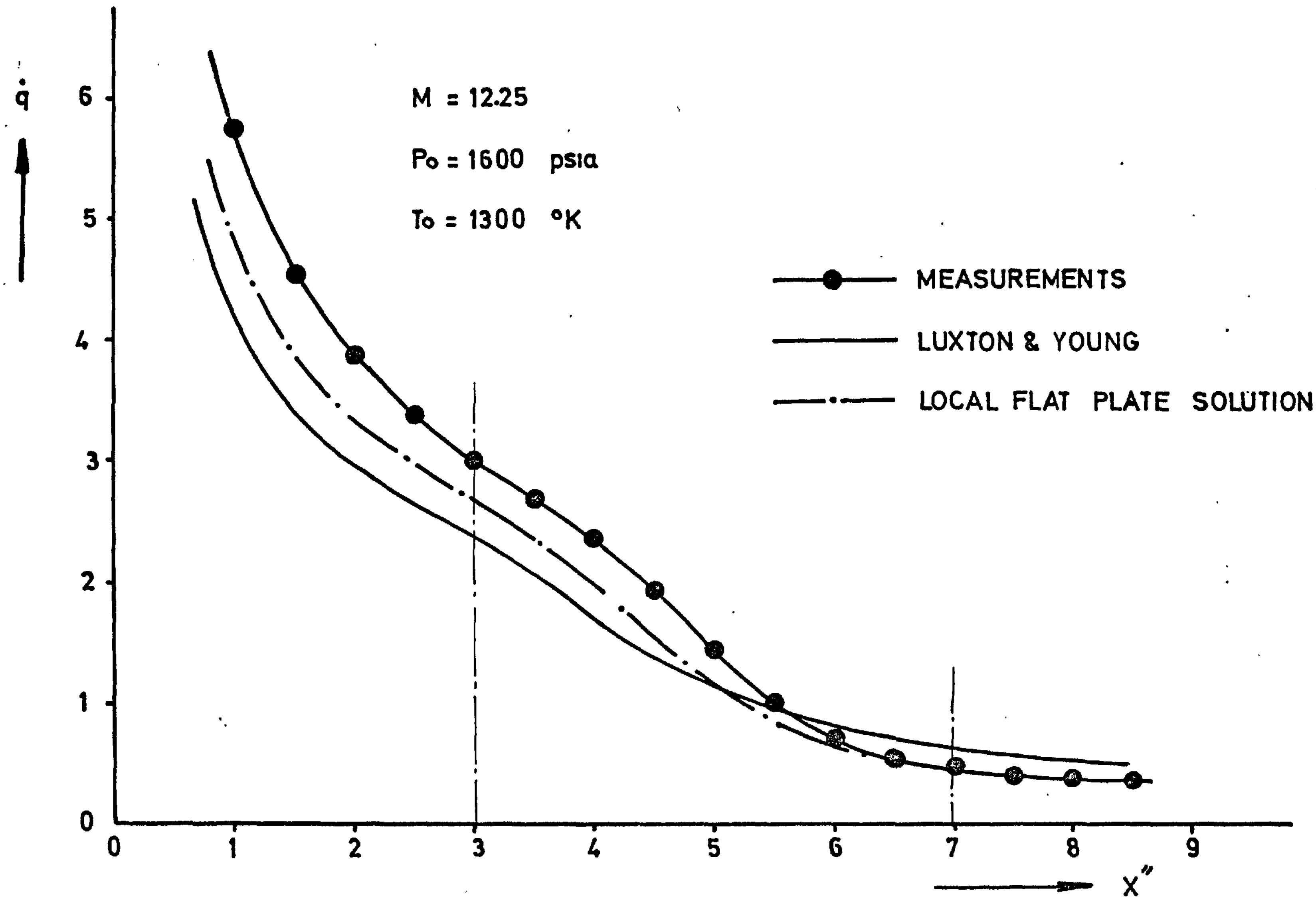

FIG. (46) HEAT TRANSFER RATE IN Btu/ft^2s ON THE CONVEX MODEL

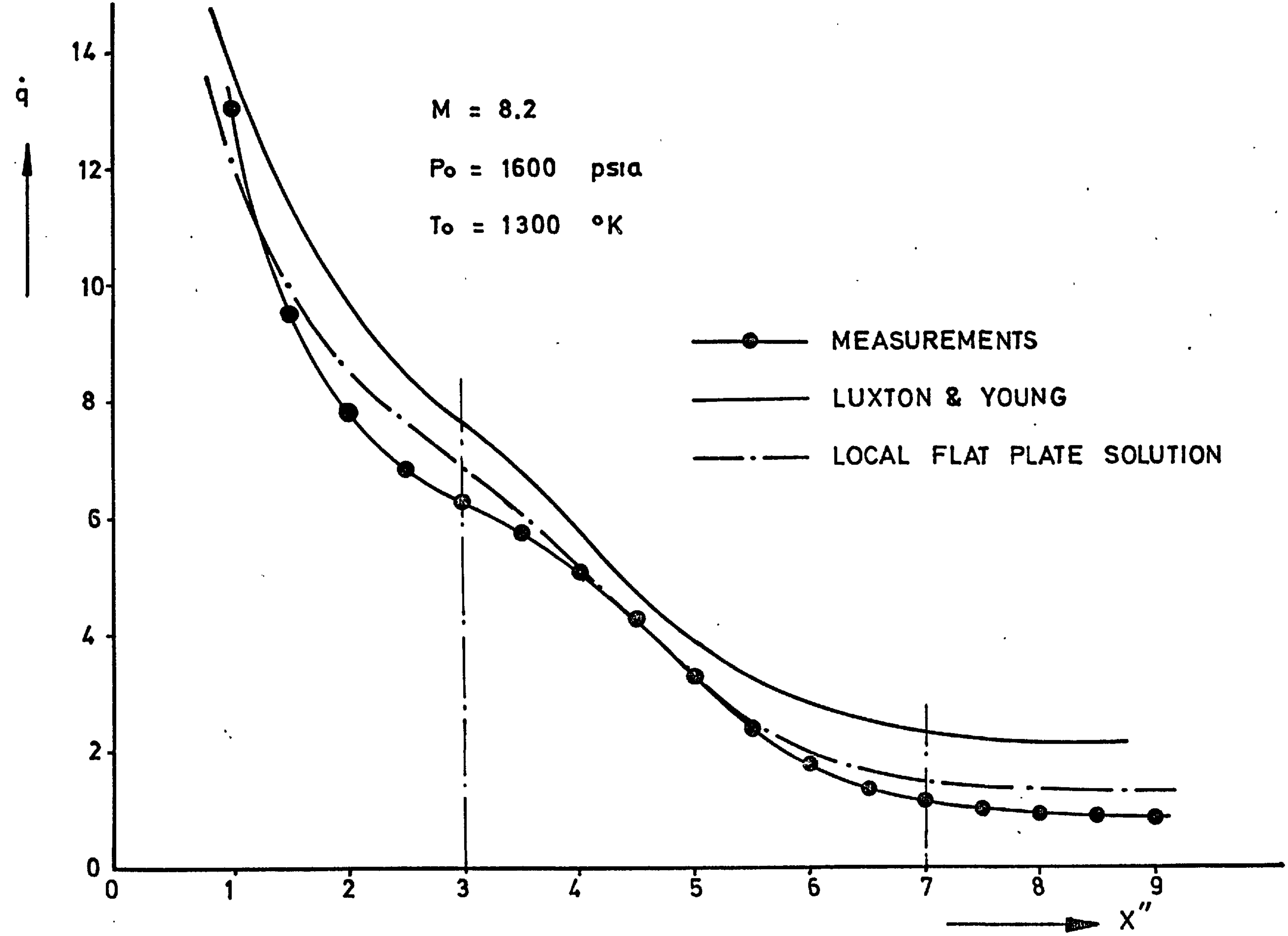

FIG. (47) HEAT TRANSFER RATE IN Btu/ft^2s ON THE CONVEX MODEL

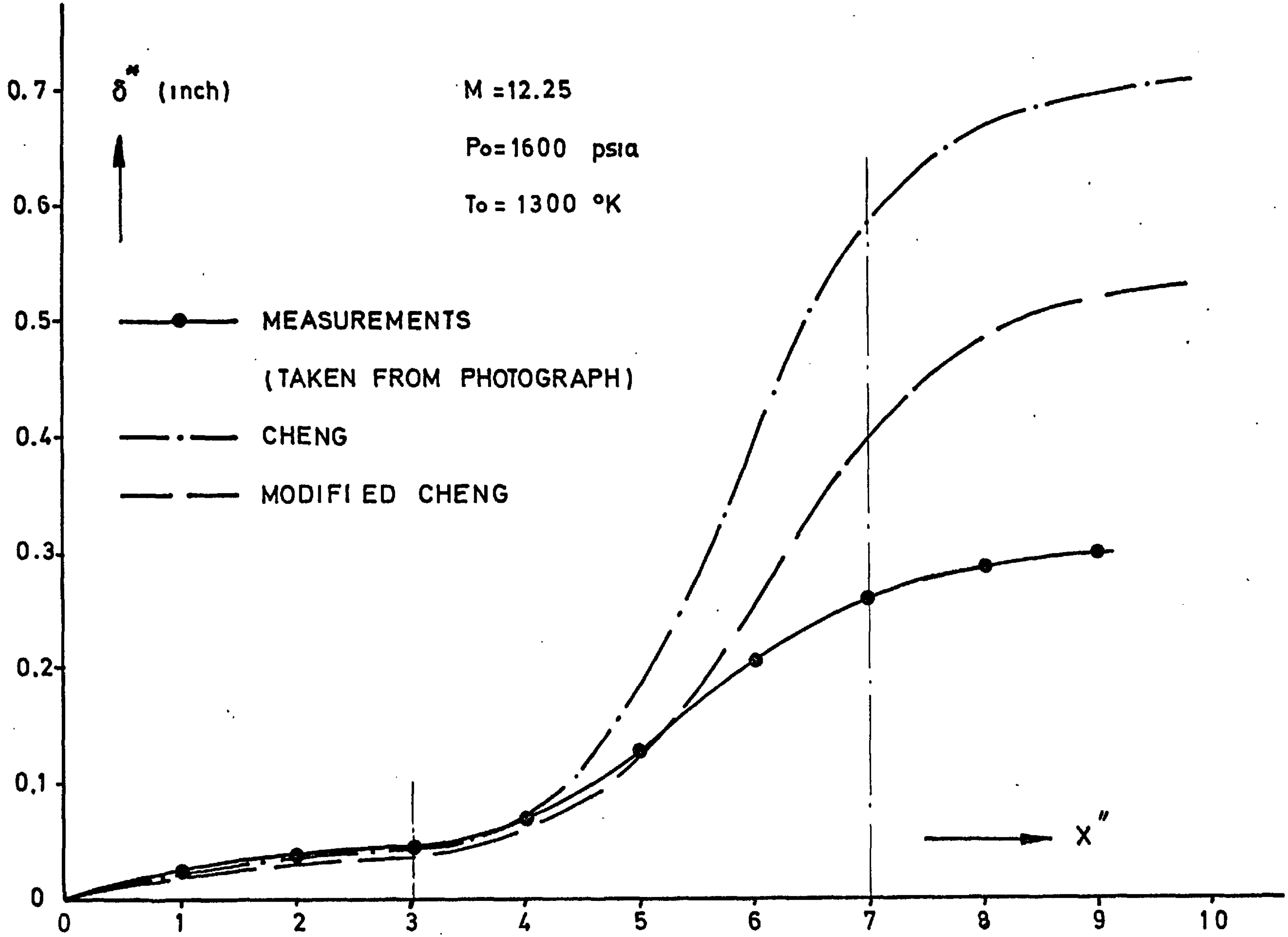

FIG.(48) DISPLACEMENT THICKNESS ON THE CONVEX SURFACE